SANDIA REPORT
SAND2019-13016
Printed October 2019

Sandia National Laboratories

# Mechanistic origins of stochastic rupture in metals

Philip Noell, Jay D. Carroll, Helena Jin, Sharlotte L.B. Kramer, Ryan B. Sills, Douglas L. Medlin, Julian E.C. Sabisch, Brad L. Boyce

Prepared by
Sandia National Laboratories
Albuquerque, New Mexico 87185 and Livermore, California 94550

Issued by Sandia National Laboratories, operated for the United States Department of Energy by National Technology & Engineering Solutions of Sandia, LLC.



Available to DOE and DOE contractors from

U.S. Department of Energy

Office of Scientific and Technical Information

P.O. Box 62

Oak Ridge, TN 37831

Telephone: (865) 576-8401

Facsimile: (865) 576-5728

E-Mail: reports@osti.gov

Online ordering: http://www.osti.gov/scitech

Available to the public from

U.S. Department of Commerce

National Technical Information Service

5301 Shawnee Rd

Alexandria, VA 22312

Telephone: (800) 553-6847

Facsimile: (703) 605-6900

E-Mail: orders@ntis.gov

Online order: https://classic.ntis.gov/help/order-methods/

## ABSTRACT

The classic models for ductile fracture of metals were based on experimental observations dating back to the 1950's. Using advanced microscopy techniques and modeling algorithms that have been developed over the past several decades, it is possible now to examine the micro- and nano-scale mechanisms of ductile rupture in more detail. This new information enables a revised understanding of the ductile rupture process under quasi-static room temperature conditions in ductile pure metals and alloys containing hard particles. While ductile rupture has traditionally been viewed through the lens of nucleation-growth-and-coalescence, a new taxonomy is proposed involving the competition or cooperation of up to seven distinct rupture mechanisms. Generally, void nucleation via vacancy condensation is not rate limiting, but is extensive within localized shear bands of intense deformation. Instead, the controlling process appears to be the development of intense local dislocation activity which enables void growth via dislocation absorption.

## ACKNOWLEDGEMENTS

The authors would like to acknowledge Drs. Joseph Michael, Daniel Bufford, Wei Cai, and Claire Chisholm for beneficial discussions. Also, the authors would like to acknowledge Todd Huber, John Laing, Zachary Casias, Brad Salzbrenner, Richard Grant, Sara Dickens, Alice Kilgo, Chad Taylor, Bonnie McKenzie, Amy Allen, Michael Rye, Celedonio Jaramillo, Christina Profazi, and Curtis Mowry for their exceptional experimental support. Special acknowledgement is given to Xianghui Xiao of the Advanced Photon Source for assistance with designing the *in situ* x-ray computed tomography experiments. This project was funded by a Laboratory Directed Research and Development Program at Sandia National Laboratories. BPC acknowledges funding by National Science Foundation Graduate Research Fellowship Program (Grant number 1315231). This work was performed, in part, at the Center for Integrated Nanotechnologies, an Office of Science User Facility operated for the U.S. Department of Energy (DOE) Office of Science. Sandia National Laboratories is a multimission laboratory managed and operated by National Technology & Engineering Solutions of Sandia, LLC, a wholly owned subsidiary of Honeywell International, Inc., for the U.S. DOE's National Nuclear Security Administration under contract DE-NA-0003525. The views expressed in the article do not necessarily represent the views of the U.S. DOE or the United States Government.

## CONTENTS

## LIST OF FIGURES

## LIST OF TABLES

This page left blank

# ACRONYMS AND DEFINITIONS

| Abbreviation | Definition |
|---|---|
| DRX | Dynamic recrystallization |
| FCC | Face centered cubic |
| BCC | Body centered cubic |
| GOS | Grain orientation spread |
| ECCI | Electron channeling contrast imaging |
| TD | Tensile direction |
| LTD | Long transverse direction |
| STD | Short transvers direction |
| RAD | Radial direction |
| KAM | Kernel average misorientation |
| YS | Yield strength |
| UTS | Ultimate tensile strength |
| SEM | Scanning electron microscope |
| TEM | Transmission electron microscope |
| EBSD | Electron backscatter diffraction |
| GND | Geometrically necessary dislocation |
| OAS | Orowan alternating slip |
| XCT | X-ray computed tomography |

# 1. A PROPOSED TAXONOMY OF DUCTILE RUPTURE MECHANISMS

One of the most confounding controversies in the ductile fracture community is the large discrepancy between predicted and experimentally observed strain-to-failure values during shear-dominant loading. Currently proposed solutions focus on better accounting for how the deviatoric stress state influences void growth or on measuring strain at the microscale rather than the macroscale. While these approaches are useful, they do not address the root of the problem: the only rupture micromechanisms that are generally considered are void nucleation, growth, and coalescence (for tensile-dominated loading), and shear-localization and void coalescence (for shear-dominated loading). Current phenomenological models have thus focused on predicting the competition between these mechanisms based on the stress state and the strain-hardening capacity of the material. However, in the present study, we demonstrate that there are at least five other failure mechanisms. Because these have long been ignored, little is known about how all seven mechanisms interact with one another or the factors that control their competition between. These questions are addressed by characterizing the fracture process in three high-purity face-centered cubic (FCC) metals of medium-to-high stacking fault energy: copper, nickel, and aluminum. These data demonstrate that, for a given stress state and material, several mechanisms frequently work together in a sequential manner to cause fracture. The selection of a failure mechanism is significantly affected by the plasticity-induced microstructural evolution that occurs before tearing begins, which can create or eliminate sites for void nucleation. At the macroscale, failure mechanisms that do not involve cracking or pore growth were observed to facilitate subsequent void growth and coalescence processes. While the focus of this study is on damage accumulation in pure metals, these results are also applicable to understanding failure in engineering alloys.

## 1.1. Introduction

With the advent of fracture mechanics in the 20th century, many problems in fracture became relatively easy to predict. Today, concepts based on linear elastic fracture mechanics [27] and elastoplatic fracture mechanics [28, 29] are widely used to predict failure of ductile metals. Although these methods are often useful, studies such as the Sandia Fracture Challenge [25, 30] have highlighted the difficulty of predicting ductile fracture in many engineering circumstances. Additionally, many fundamental questions, such as the relative difference in ductility between tensile- and shear-dominated loading, remain unanswered. In this context, the goal of this study is to examine the mechanisms of ductile rupture and the factors that control them.

Significant work has been devoted to understanding the relationship between stress state and the amount of deformation a material can tolerate before a ductile crack forms, *i.e.* the failure strain [21, 28, 29, 31, 32, 33, 34, 35, 36]. The stress state can be divided into hydrostatic and deviatoric components, which are referred to as the stress triaxiality ($\eta$) and Lode parameter ($L$), respectively. These are defined analytically as

$$\eta = \frac{\sigma_I+\sigma_{II}+\sigma_{III}}{3(0.5[(\sigma_I-\sigma_{II})^2+(\sigma_{II}-\sigma_{III})^2+(\sigma_{III}-\sigma_I)^2])} \quad (1)$$

and

$$L = \frac{2\sigma_{II}-\sigma_I-\sigma_{III}}{\sigma_I-\sigma_{III}} \quad (2)$$

where $\sigma_I$, $\sigma_{II}$, and $\sigma_{III}$ are the principle stresses in decreasing magnitude. Early studies of ductile fracture focused on understanding failure during tensile-dominated loading when the stress triaxiality is 1/3 (uniaxial tension) or greater. It is now widely accepted that the failure strain decreases with

increasing stress triaxiality for stress triaxialities of 1/3 or greater [31, 37, 38]. This has led to the formulation of several ductile fracture criteria based on quantifying the macroscopic loading response of a porous, ductile material, *e.g.* references [32, 33].

Based on the well-known study by Johnson and Cook [39], it was generally held that failure strain continues to increase as stress triaxiality decreases below 1/3. However, in their 2004 study of fracture in 2024-T351 aluminum, Bao and Wierzbicki [36] demonstrated that this is not always true. Instead, below a stress triaxiality of about 1/3, they observed that failure strain decreased with decreasing stress triaxiality, reached a minimum for conditions of pure shear (a stress triaxiality of 0), and increased rapidly for negative stress triaxialities. This relationship is presented in Figure 53(a). Several subsequent studies reported similar relationships between failure strain and stress triaxiality [20, 40, 41]. Accordingly, shear-modified Gurson [23], Mohr-Coulomb [42, 43]), and other [21, 44, 45] models were formulated to capture the effects of shear-dominated loading.

To accurately calibrate these new phenomenological models, Teng and Wierzbicki [11] proposed that there are two basic mechanisms of failure: void growth and shear decohesion. These proposed mechanisms are based on the assumption that the material contains preexisting voids or that they nucleate early in the deformation process. Consequently, it is assumed that the rate-limiting step in failure is the growth and coalescence of these voids [32, 46, 47, 48, 49]. Barsoum *et al.* [20, 21, 44] subsequently demonstrated that these mechanisms are better described as failure by intervoid necking and intervoid shearing, respectively. These mechanisms are defined as the internal necking of the ligaments between voids leading to their gradual enlargement and coalescence, and shear localization between voids leading to their elongation along the shear axis and coalescence [20, 21]. The stress-state-based competition between these two mechanisms is thought to explain why the left and right branches of the fracture envelope in Figure 53(a) are often observed [20, 21].

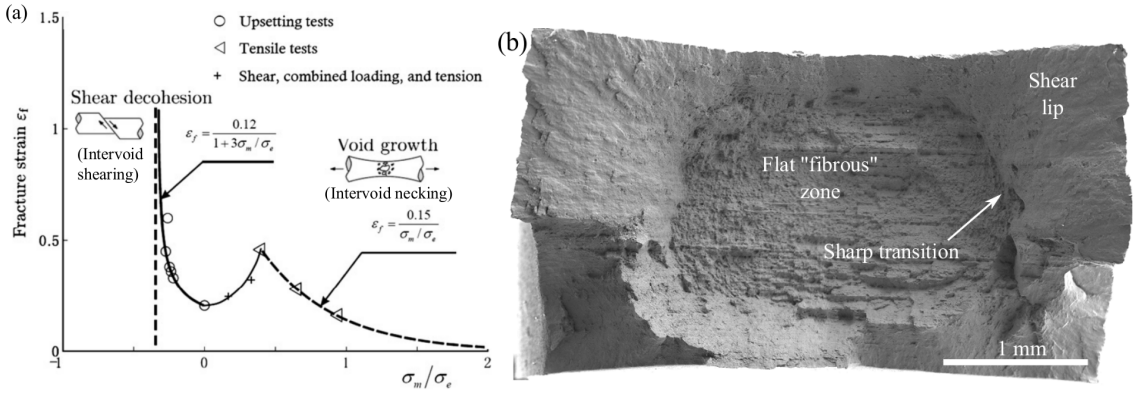


**Figure 1: A plot of the fracture strain for Al 2024-T351 specimens tested under different stress triaxialities ( $\sigma_m/\sigma_e$) is provided in (a). Teng and Wierzbicki later proposed that the two distinct branches of the fracture envelope indicate that there are two failure mechanisms, which they called void growth and shear decohesion [11]. Barsoum et al. subsequently described these mechanisms as intervoid necking and intervoid shearing [20, 21]. This figure was modified from reference [23]. The image in (b) shows an example tensile fracture surface from a rectangular Ti-6Al-4V specimen tested in uniaxial tension for the second Sandia Fracture Challenge [25]. Two distinct mechanistic regimes are evident and typical of many bulk metals: a flat fibrous zone typically associated with void nucleation, growth, and coalescence, and a peripheral shear lip.**

However, the recent work of Ghahremaninezhad *et al.* [50, 51]and others [52, 53] raises some concerns about this conclusion. All of these works reported that failure strain continuously *increased* with

decreasing stress triaxiality even for stress triaxialities below 1/3. Moreover, cavitation, *i.e.* the nucleation, growth, and coalescence of voids, was never observed in an Al 6061-T6 material when a state of pure shear was maintained throughout testing [51]. One of the unique aspects of these studies was that strain was measured at the microscale rather than at the macroscale, as is more commonly reported. Ghahremaninezhad *et al.* [51] argued that the discrepancy between their results and those reported by Beese *et al.* [40] for the same material could be explained by the different scales at which strain was measured in these studies. It is unclear if microscale strain measurements will resolve this controversy, though. Using Al 2198, Morgeneyer *et al.* [54] demonstrated that once strain-localization in a shear band occurs, voids nucleate and coalesce upon a small additional microscale strain. Macroscale strain measurements also provide contradictory results. For example, for stress triaxialities between 0 and 1, Johnson and Cook [39] reported that ductility increased with decreasing stress triaxiality in copper and iron but that the failure strain for a 4340 steel specimens loaded in torsion $\eta \approx 0$ was significantly lower than that measured in tension.

In the present investigation we hypothesize that there is a more fundamental explanation for these conflicting results than that proposed by Ghahremaninezhad *et al.* [51]: fracture is not just controlled by two mechanisms. Rather, as many as seven different mechanism can control fracture. Additionally, these mechanisms are not necessarily independent or exclusive, but can work in sequence during the rupture process. These seven mechanisms are illustrated schematically in Figure 2 and are defined as follows:

1. intervoid necking: the necking of intervoid ligaments leading to void growth and coalescence [55].
2. intervoid shearing: the nucleation of voids in a shear band and the subsequent elongation of these voids along the shear band. This causes intervoid shearing leading to void coalescence and creates a macroscale crack in the plane of the shear band [20, 21].
3. void sheeting: shear localization between existing voids and the near-simultaneous nucleation and coalescence of new voids in this localization to create a ductile crack linking the preexisting voids [19].
4. the Orowan alternating slip (OAS) mechanism: void nucleation at the intersection of two shear bands and the subsequent growth of this prismatic void by a process of alternating slip along these shear bands [56].
5. necking to a point: failure without cavitation by necking to a chisel edge or a point [57],
6. single-plane catastrophic shear: failure without cavitation by slipping of the material along a single shear band [24]. If not interrupted by another mechanism, this will lead to specimen separation.
7. multi-plane catastrophic shear: failure without cavitation by slipping of the material along multiple shear bands [26]. If not interrupted by another mechanism, this will lead to specimen separation along a chisel edge, much like necking off. This mechanism is also referred to as slipping off [2, 58].

Because both intervoid shearing and void sheeting produce ductile cracks that link multiple voids along a shear band, these terms have occasionally been used synonymously. They are, however, two distinct mechanisms, with intervoid shearing characterized by the nucleation of a few voids and their subsequent growth along the shear band (void growth is rate limiting), while void sheeting is characterized by the nucleation of many voids in such close proximity they coalesce after relatively little growth (void nucleation is rate limiting). Necklace coalescence, or coalescence in columns, is another void coalescence mechanism whereby rows of voids coalesce along the tensile axis. This mechanism is observed in steels containing elongated MnS inclusions and may be a specialized case

of intervoid necking [59]; hence, it is not discussed further in this article. Examples of specimens that failed by each of the 7 mechanisms illustrated in Figure 2 are presented in Figure 3.

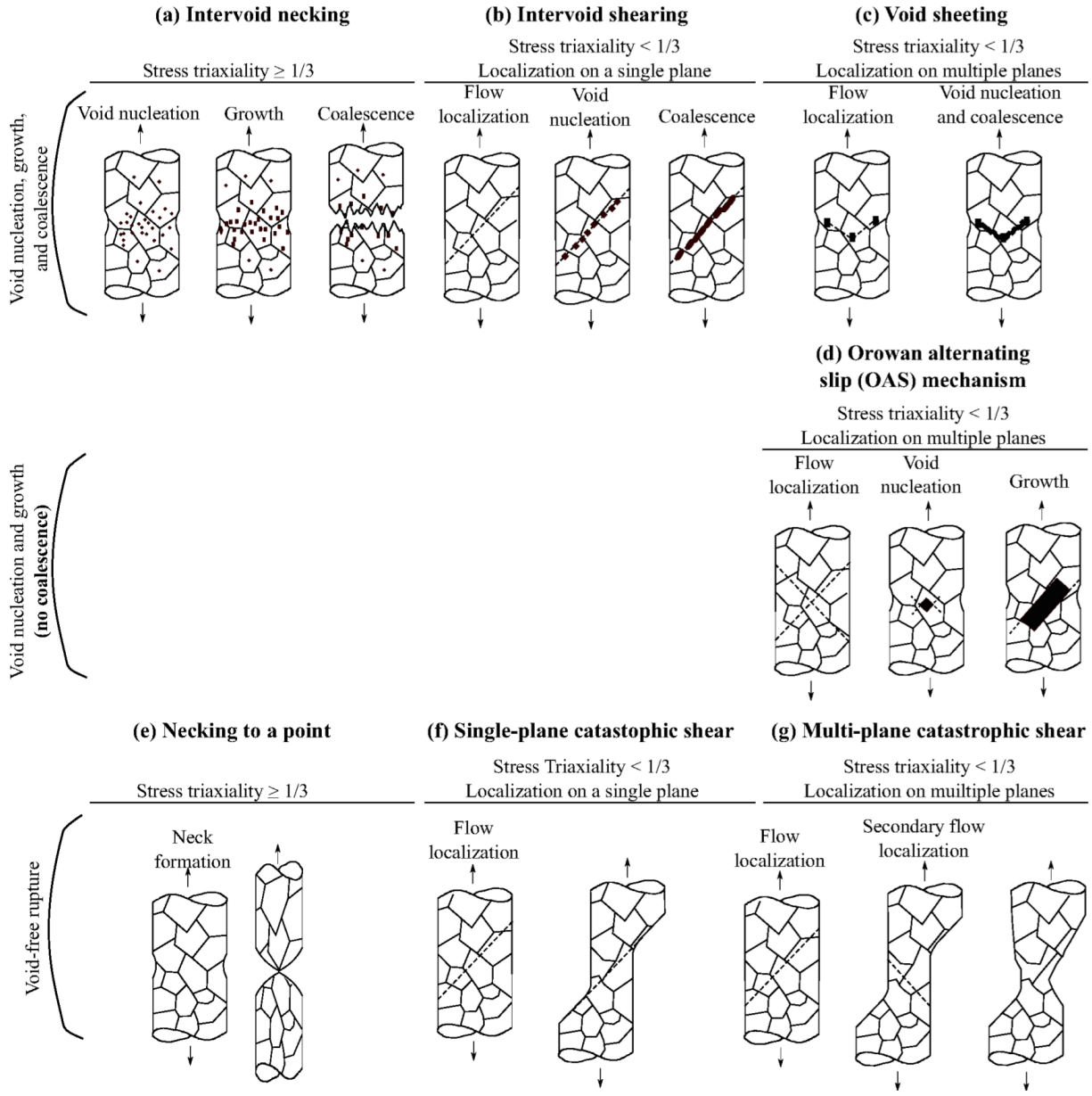


**Figure 2: Schematic representations of seven different macroscopic ductile fracture mechanisms are shown: (a) intervoid necking, (b) intervoid shearing, (c) void sheeting, (d) the Orowan alternating slip (OAS) mechanism, (e) specimen separation by necking to a point, and (f) and (g), which show specimen separation by single-plane and multi-plane catastrophic shear, respectively. Detailed definitions of each of these mechanisms are provided in the text.**

Several recent studies have examined how the competition between intervoid necking and intervoid shearing depends on stress state, but the other five failure mechanisms are usually overlooked [20, 21, 41]. In instances where other failure mechanisms were considered, it was always assumed that fracture was controlled by a single mechanism for a given stress state and material. Bridgman [60] and French and Wienrich [26, 58, 61, 62] showed that the transition from failure by intervoid necking to multi-

plane catastrophic shear depended on the stress state, with multi-plane catastrophic shear only observed when a large, compressive, hydrostatic stress was applied. Spencer *et al.* [17] later demonstrated that small differences in iron content between otherwise nominally identical AA 5754 sheet materials determined whether or not specimens failed by intervoid shearing or by the OAS mechanism. However, these and similar studies [63] have only characterized the late stages of fracture. It is thus unclear if other mechanisms played a role during the early stages of failure.

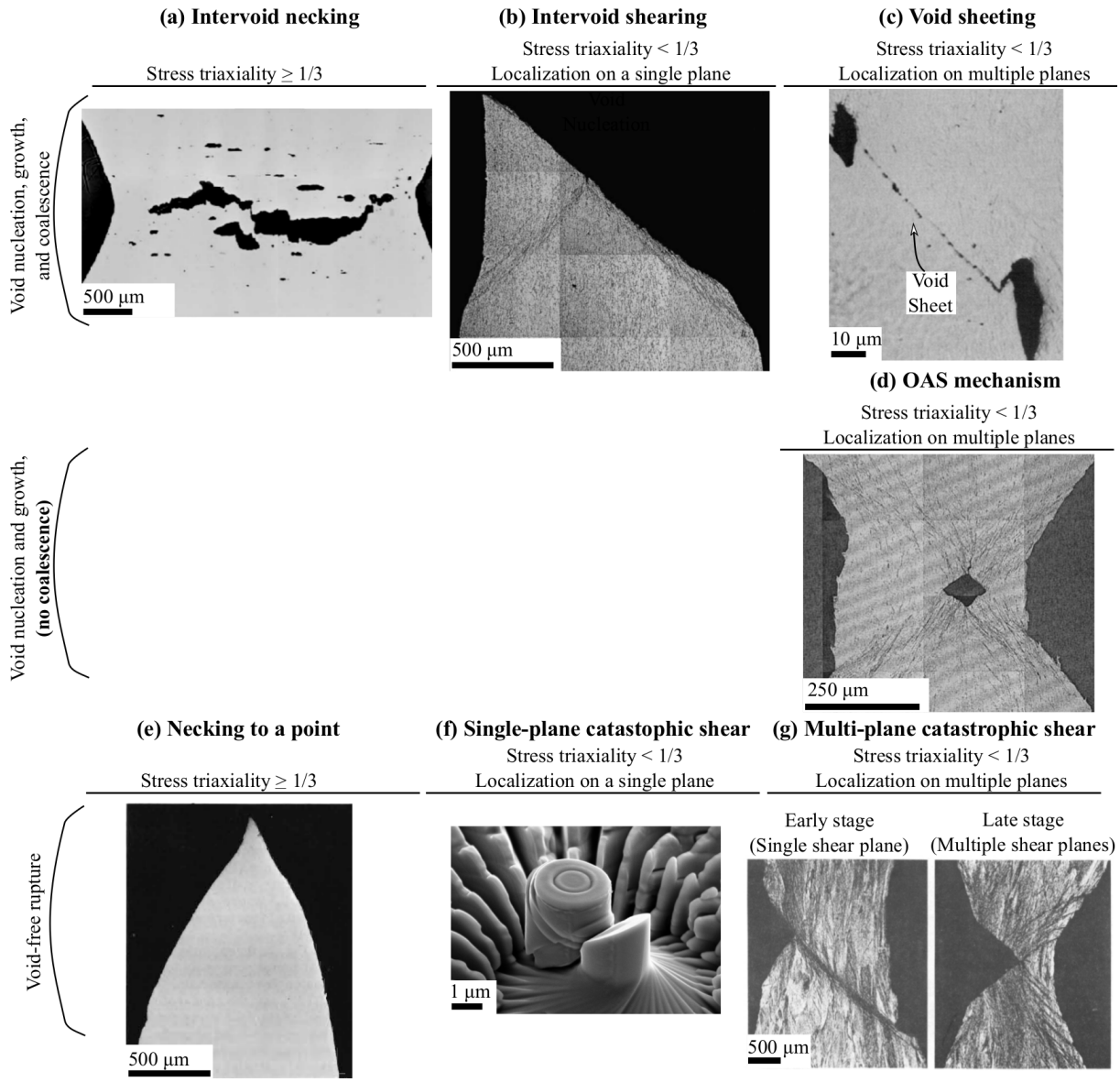


**Figure 3: SEM images of specimens whose rupture process was controlled by (a) intervoid necking, (b) intervoid shearing, (c) void sheeting, (d) the OAS mechanism, (e) necking to a point, (f) single-plane catastrophic shear, and (g) multi-plane catastrophic shear are provided. In order, these images are from references [10], [17], [19], [22], [24], [26].**

In the present study we propose that fracture is frequently controlled by a sequential progression of multiple mechanisms. In addition, we hypothesize that these mechanisms not only compete with one another but can also facilitate each other. A classic, but often overlooked, example of this is the case of cup-and-cone failure in structural metals. The fracture surface of most tensile bars shows both a

central flat fibrous zone of ductile dimples and a sharp, well defined transition to a peripheral shear lip region. An example of this is shown in Figure 53(b). However, nearly all failure models, as illustrated in the Sandia Fracture Challenges [25, 30], predict either no transition or a smooth transition. We argue that because there are at least two separate mechanisms, *e.g.* intervoid necking and intervoid shearing, operating in sequence during this failure process, two or more models would be necessary to accurately represent the progression of fracture.

To examine these hypotheses, the fracture processes of high-purity copper, nickel, and aluminum were characterized using interrupted deformation experiments and a variety of characterization methods. These three materials are all face-centered cubic (FCC) and deform by slip during quasistatic, room-temperature deformation. These materials were chosen as model systems for their pedagogical simplicity, *i.e.* they are all ductile, single-phase materials. Moreover, these three materials illustrate that not all FCC metals fail by the same mechanism, a point of controversy in the literature. Some observers have reported that these materials fail by necking to a point [22, 57, 64], but a recent study of high-purity copper concluded that it failed by the OAS mechanism [63]. These specific materials were also chosen to examine the influence of strain-hardening capacity and dynamic recrystallization on the failure process. Tekoglu *et al.* [65] predicted that the competition between intervoid necking and intervoid shearing depends on strain-hardening capacity. Hence, two materials with very different strain-hardening capacities (copper and nickel) were chosen. Copper and nickel have relatively large and small strain-hardening capacities, respectively, with nominal strain-hardening constants of $m_{Cu}$= 0.54 and $A_{Cu}$= 315 [66] and $m_{Ni}$= 0.39 and $A_{Ni}$= 138 [67]. High-purity aluminum was chosen to study how dynamic recrystallization affects the fracture process. Dynamic recrystallization has been observed in this material during room-temperature deformation of specimens with purities of 99.99% or greater [68, 69]. The focus of this study was on failure during uniaxial tension in sheet specimens of these three materials, but the fracture surfaces of wire specimens of each material were also characterized to understand the damage progression under an isotropic state of constraint.

Although this study is restricted to high-purity metals, these results are also relevant to metals that contain second-phase particles. In pure metals, voids nucleate at features such as grain boundaries and deformation-induced dislocation boundaries [12, 70, 71], while second-phase particles are the primary void-nucleation site in most engineering materials [2, 72]. Second-phase particles likely accelerate the void-nucleation process [73] and void-based failure mechanisms are favored in many materials. The failure process in pure metals thus illustrates a wider range of failure mechanisms than is observed in most engineering materials while simultaneously providing information about the competition between void-based failure mechanisms.

## 1.2. Experimental Methods

Seven aluminum, copper, and nickel materials having different purities and geometries were examined in this study. Table 1 summarizes the purity and geometry (wire or sheet specimen) of these different materials. Material purity is abbreviated as the number of nines of the majority element in the material, *e.g.* 99.999% aluminum is abbreviated as 5N-Al. At least one wire and one sheet specimen of copper, nickel, and aluminum were tested in this study. The as-received diameter (for wires) and sheet thickness (for sheet materials) and the figures relevant to each material are provided in Table 1. In addition, if inclusions were observed in the material, the average diameter of these inclusions is listed. All materials were procured from ESPI Metals (Ashland, OR). The as-received microstructures of these materials are described in section 3 as appropriate.

**Table 1. A reference list of the materials tested for this study is provided. For each material, the wire diameter or sheet thickness, the tests performed on them, and the figures relevant to them are listed. Material purity is designated by the number of nines of that material, e.g. 5N-Al is 99.999% aluminum. If inclusions were observed in the material, the average diameter of these inclusions is reported. Seven different materials were characterized: an aluminum wire material, two aluminum sheet materials, a copper wire material, a copper sheet material, a nickel wire material, and a nickel sheet material.**

| Material | Diameter or Thickness (mm) | Inclusion Diameter (nm) | Number tested | Relevant Figures |
|---|---|---|---|---|
| 5N-Al Wire | 1.27 | None | 1 | Figure 5 |
| 4N-Al Sheet | 2.07 | None | 1 | Figure 6 |
| 5N-Al Sheet | 2.07 | None | 7 | Figure 6 |
| 5N-Cu Wire | 1.07 | ~500 | 1 | Figure 5 |
| 3N-Cu Sheet | 1.62 | ~200 | 13 | Figure 7, Figure 8, Figure 9 |
| 4N-Ni Wire | 0.76 | None | 1 | Figure 5 |
| 4N-Ni Sheet | 2.07 | None | 9 | Figure 10, Figure 11, Figure 12 |

All materials were tested in quasistatic, uniaxial tension at room temperature. At least one specimen of each of the seven materials was elongated to failure. Wire specimens were cut from the as-received wire spools, gripped using pneumatic grips, and elongated to failure at a constant cross-head displacement rate of 0.127 mm/s. The wire length between the grips was approximately 100 mm, though strain in these wire specimens was not measured. Tensile specimens were extracted from the sheet materials using waterjet cutting. The edges of the gauge regions were subsequently deburred and ground smooth using a handheld grinder. The geometry of sheet tensile specimens was identical to that of the hourglass-shaped tensile bars used by Noell *et al.* [71]. Sheet tensile specimens retained the as-received sheet thickness (1.62 mm for the 3N-Cu sheet material and 2.07 mm for the 4N-Ni, 4N-Al, and 5N-Al sheet materials). The gauge region of sheet tensile specimens had an hourglass radius to encourage strain localization in the middle of the gauge region. The minimum gauge width was 2.79 mm and the overall gauge length was 8.47 mm.

Sheet tensile specimens were tested using displacement-control at a constant displacement rate of 0.127 mm/s. Typical engineering stress *versus* engineering strain data from tensile tests of the 3N-Cu, 4N-Ni, and 5N-Al sheet materials are provided in Figure 4. Strain measurements were performed using stereoscopic digital image correlation (DIC) [74] using a subset size of 35 pixels, a step size of 9 pixels, and a 2.35 mm long digital strain gauge. The noise level of DIC extensometer measurements was $\pm$0.004% as determined from zero-load baseline experiments. The extensometer used for these strain measurements is illustrated in Figure 4 with DIC data from a 3N-Cu tensile specimen. This figure also illustrates the three primary axes of the sheet tensile specimens: the tensile direction (TD),

the long transverse direction (LTD), and the short transverse direction (STD). In all cases, the STD was parallel to the thickness direction of the original sheet.

To understand the fracture process in these seven materials, macrofractographs of each fractured specimen were taken using secondary electron mode in a scanning electron microscope (SEM). One of the two fractured halves of each of the 5N-Al, 4N-Ni, and 3N-Cu wire specimens and the 4N-Al sheet specimen was subsequently mounted and polished flat to study the microstructure at and near the fracture surface in the plane parallel to the TD. Final polishes were performed on these specimens using colloidal silica for extended times. High-resolution electron channeling contrast (ECC) images of these specimens were then taken using a Zeiss Supra 55VP field emission SEM.

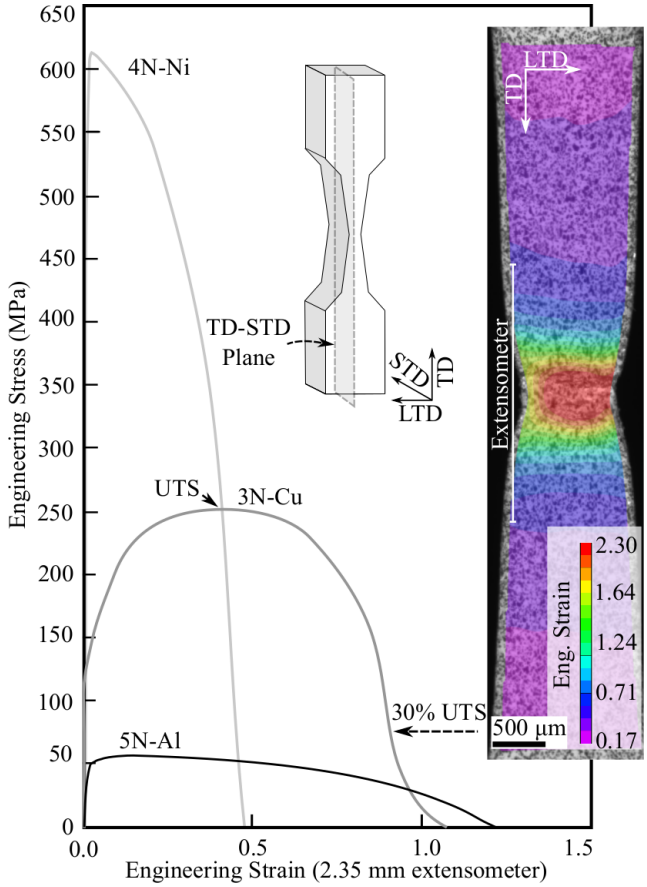


**Figure 4: Engineering stress versus engineering strain data illustrate the significant differences in flow behavior in the 5N-Al, 3N-Cu, and 4N-Ni sheet materials. The schematic drawing shows the orientation of sheet tensile specimens. These engineering strain data were measured using stereographic DIC. An example DIC dataset is shown overlaid on an image of a 3N-Cu tensile specimen. In this case, the tensile deformation was interrupted once the flow stress had dropped to 30% of the ultimate tensile stress (UTS).**

To study the fracture process in the 5N-Al, 3N-Cu, and 4N-Ni sheet materials, interrupted tensile tests were performed using the method described in [71]. This method is briefly summarized here. The force applied to the specimen was monitored throughout the test. Once the load reached a maximum at the ultimate tensile strength (UTS), this value was recorded. Tensile deformation was subsequently interrupted when the force dropped to a preprogrammed proportion of the UTS. To illustrate this method, Figure 4 shows an image of a 3N-Cu specimen whose tensile deformation was

halted at 30% of the UTS. Multiple specimens of each of the 5N-Al, 3N-Cu, and 4N-Ni sheet materials were tested and interrupted at various points before final fracture. A summary of these specimens is provided in Table 2. By examining several specimens of each material, a representative understanding of the fracture process in each of these sheet materials was acquired.

**Table 2. A summary of the interrupted tensile tests that were performed on the 5N-Al, 3N-Cu, and 4N-Ni sheet materials is provided. Two tensile specimens of the 5N-Al sheet material were interrupted at 10% of the UTS.**

| Material | Interrupted Specimens (% of the UTS) |
|---|---|
| 5N-Al Sheet | 60%, 50%, 30%, 15%, 10% (x2) |
| 3N-Cu Sheet | 90%, 80%, 70%, 60%, 55%, 50%, 40%, 30%, 20%, 15%, 10%, 5% |
| 4N-Ni Sheet | 80%, 60%, 50%, 40%, 30%, 25%, 20%, 10% |

Damage accumulation in these tensile specimens was assessed by mounting tested specimens and grinding them down to their approximate midplane. In the 3N-Cu and 4N-Ni sheet materials, strain localized in macroscopic shear bands that formed an angle of about 45with the TD-STD plane. To understand damage accumulation within these shear bands, 3N-Cu and 4N-Ni sheet specimens were sectioned revealing the TD-STD plane. Because shear bands did not form in the 5N-Al sheet material, was not necessary to examine the TD-STD plane in this material. Instead, specimens of this material were sectioned normal to the STD to observe the TD-LTD plane. This allowed a larger area of material to be characterized than was visible on the TD-STD plane. After being ground flat, the planar surfaces of tensile specimens of these three (5N-Al, 3N-Cu, and 4N-Ni) sheet materials were polished using diamond suspensions, followed by at least 24 hours of final vibratory polishing using $Al_2O_3$. For the 5N-Al sheet specimens, an additional electropolishing step was used. The electrolyte was 60mL of 70% perchloric acid, 590mL of methanol, and 350mL ethylene glycol monobutyl ether. Various voltages and electropolishing times were used since no single combination produced consistent results. ECC images were taken of the midplane cross sections of polished specimens using a Zeiss Supra 55VP field emission SEM.

## 1.3. Results

Table 3 summarizes the mechanisms that controlled fracture in each material and the corresponding stress state during damage accumulation. This table summarizes a key result of this study: for a given stress state and material, multiple mechanisms can contribute to failure. This table also highlights the significant differences between the fracture processes in the aluminum, copper, and nickel materials. Detailed descriptions of these are provided in the following paragraphs.

**Table 3. For each material, the mechanisms that controlled fracture and the corresponding stress triaxiality during damage accumulation are summarized. The OAS mechanism refers to the growth of a cavity by a process of alternating slip; no voids were observed to nucleate by the OAS mechanism. A high local stress triaxiality is defined as 1/3 (uniaxial tension) or greater, e.g. the stress state in the necked gauge region before a shear band formed. A low local stress triaxiality**

**is defined as being between 0 and 1/3 (a mix of shear and tension), e.g. the stress state in the necked gauge region after a shear band formed.**

| Specimen | Dominant Rupture Mechanisms | Local Stress Triaxiality ($\eta$) |
|---|---|---|
| 5N-Al Wire | Necking to a point | High |
| 4N-Al Sheet | Necking to a point | High |
| 5N-Al Sheet | Intervoid necking | High |
| 5N-Cu Wire | Intervoid necking→OAS | High→Low |
| 3N-Cu Sheet | Intervoid necking→Void sheeting→OAS | High→Low→Low |
| 4N-Ni Wire | Intervoid necking →Intervoid shearing | High→Low |
| 4N-Ni Sheet | Single-plane catastrophic shear →Intervoid shearing→OAS | Low→Low→Low |

The significant differences between the fracture processes in aluminum, nickel, and copper were readily apparent on the fracture surfaces of wire specimens of these three materials. These fracture surfaces are presented in Figure 5 as sketches and macrofractographs. ECC images of cross-sections of these fracture surfaces are also provided in Figure 5. The 5N-Al wire failed by necking to a point (see Figure 5(a)). A few small dimples were observed near the fracture tip, but the morphology of the fracture surface indicates that failure in this material was controlled by necking. These dimples are evidence of a void nucleation and growth process that was interrupted when the material necked to a point. The 5N-Cu wire specimen had a cup-cup fracture surface (see Figure 5(b)). The center of the fracture surface was covered in tensile dimples, defined as dimples that are roughly equiaxed in the plane of the fracture surface and elongated along the tensile axis [20]. This indicates that voids initially nucleated, grew, and coalesced in the center of the diffuse neck by intervoid necking. The slanted edges of the fracture surface were essentially dimple free, evidence that the final fracture process was controlled by the growth of a central cavity by the OAS mechanism. The fracture surface of the 4N-Ni wire was reminiscent of a classic cup-and-cone fracture surface (see Figure 5(c)). The fibrous zone in the center of the specimen was covered with tensile dimples, indicating that a central cavity formed by intervoid necking. The slanted edges of the fracture surface were covered in shear dimples, defined as dimples that are elongated along the direction of shear. This indicates that, once strain localized in shear bands, voids within these shear bands coalesced by intervoid shearing.

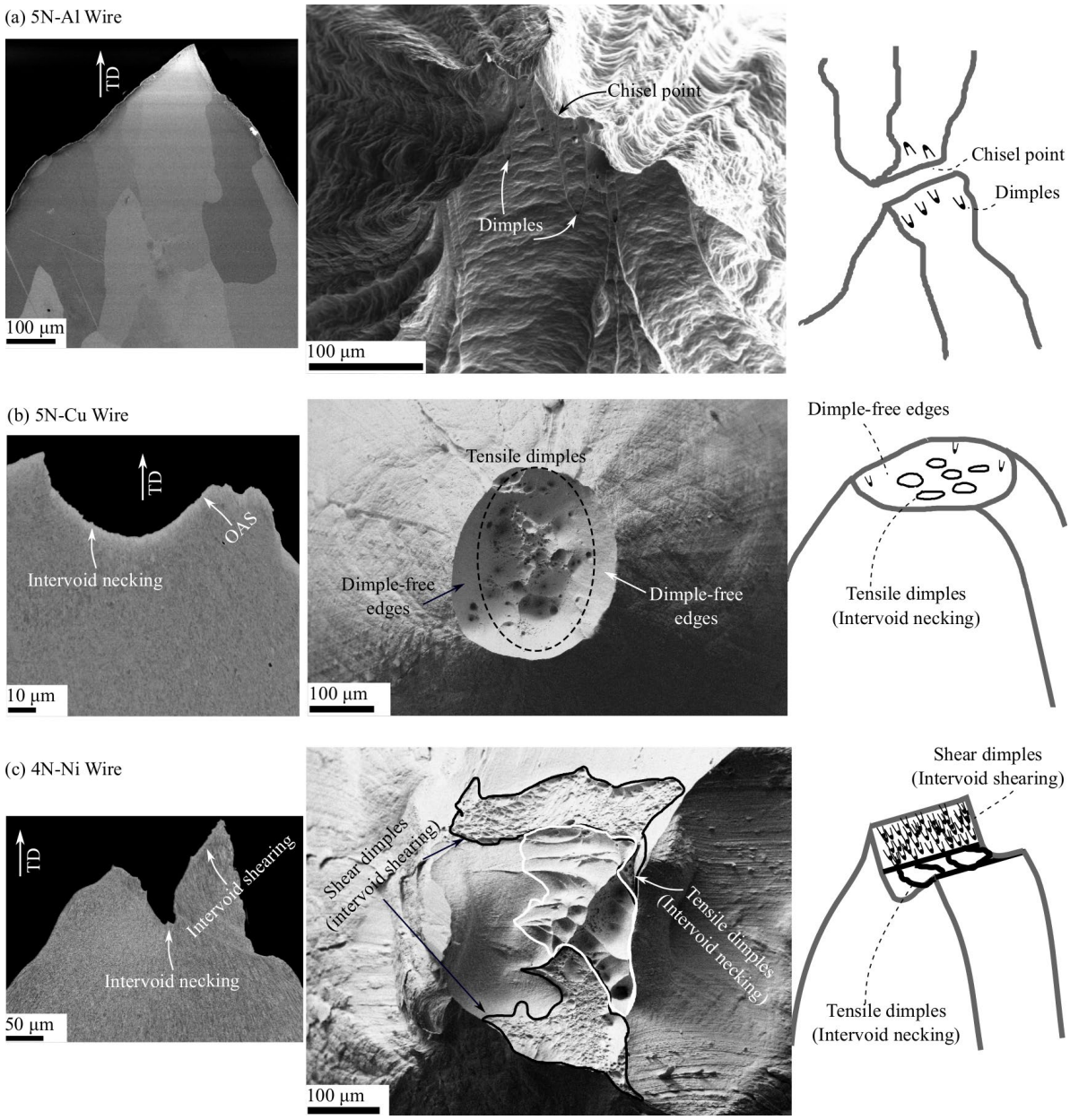


**Figure 5: The fracture surfaces of three high-purity wires of (a) aluminum, (b) copper, and (c) nickel are shown. For each material, the following are provided (left to right): an electron channeling contrast (ECC) image of a cross-section of the fracture surface, a secondary electron image of the fracture surface (taken normal to the plane of the fracture), and an illustrative sketch of the fracture surface. These images highlight the significant differences between the fracture surfaces of these three wire materials.**

The relationship between grain size and fracture mechanism in aluminum was examined by studying the fracture process in the 4N-Al and 5N-Al sheet materials, which had initial grain sizes of 2000 $\mu$m and 300 $\mu$m, respectively. The fracture processes in these two materials are illustrated in Figure 6. The 5N-Al sheet material failed by intervoid necking, as evidenced by its fracture surface (see Figure 6(a)). Additionally, voids were observed in the diffuse necks of 5N-Al sheet specimens whose deformation

was halted shortly before final fracture (see Figure 6(c)). The 4N-Al material failed by necking to a point, as can be seen from Figure 6(d) and (e). A few small dimples were observed on the fracture surface of the 4N-Al sheet material, but the morphology of the fracture surface indicates that failure was dominated by necking rather than cavitation. Shear bands did not form in either material and the stress triaxiality throughout testing remained 1/3 or greater. These observations elucidate the fact that the failure mechanisms are dependent on a number of factors beyond the stress state and elemental composition.

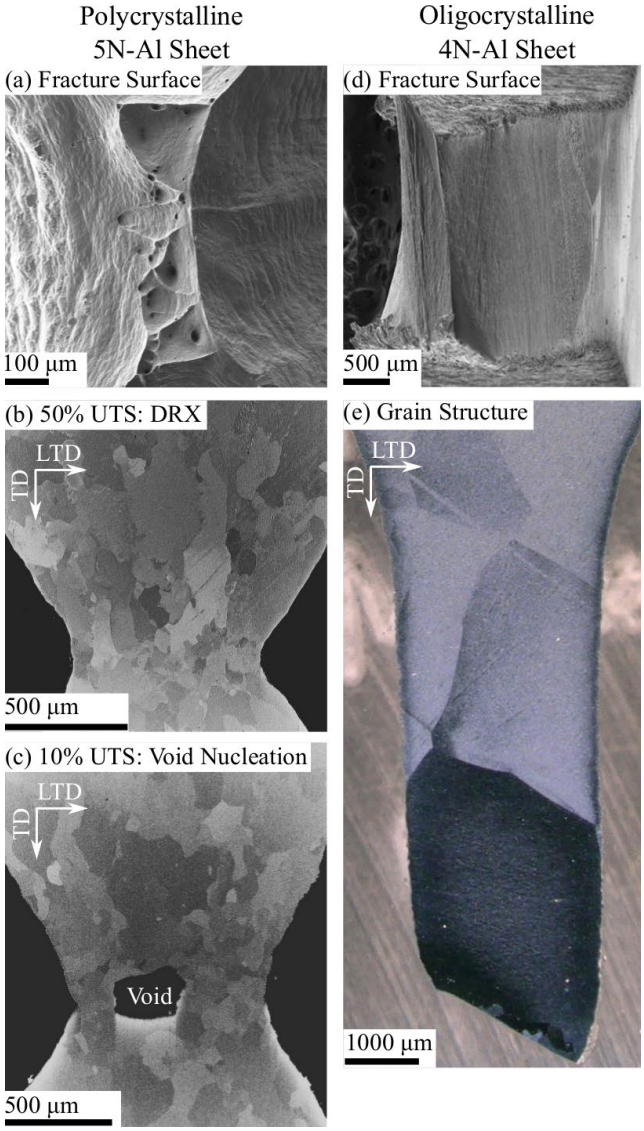


**Figure 6: The fracture processes of two different high-purity aluminum materials are shown. The polycrystalline 5N-Al material failed by intervoid necking, as the images in (a) and (c) show. Dynamic recrystallization (DRX) created new, strain-free grains in the 5N-Al sheet material, as (b) highlights. The oligocrystalline 4N-Al material failed by necking to a point, as illustrated in images in (d) and (e).**

The influence of strain-hardening capacity on the active fracture mechanism was addressed by comparing the fracture processes in a 3N-Cu sheet material to that in a 4N-Ni sheet material. Fracture in the 3N-Cu material involved three steps:

1. the nucleation of voids within the diffuse neck and the growth of these voids by intervoid necking,
2. strain localization into a shear band and subsequent void coalescence along this shear band by void sheeting to form large, prismatic cavities, and
3. the growth of these cavities by the OAS mechanism until final specimen separation.

These three stages of the process are illustrated in Figure 7 and are described in greater detail in the following paragraphs. Voids were first observed in the diffuse neck of a specimen whose tensile deformation was interrupted at 80% of the UTS; no voids were observed in a specimen interrupted at 90% of the UTS. Most voids nucleated near the center of the diffuse neck where the stress triaxiality was the largest. This is illustrated in Figure 7(a), which shows the midplane cross section of a specimen whose tensile deformation was interrupted at 60% of the UTS.

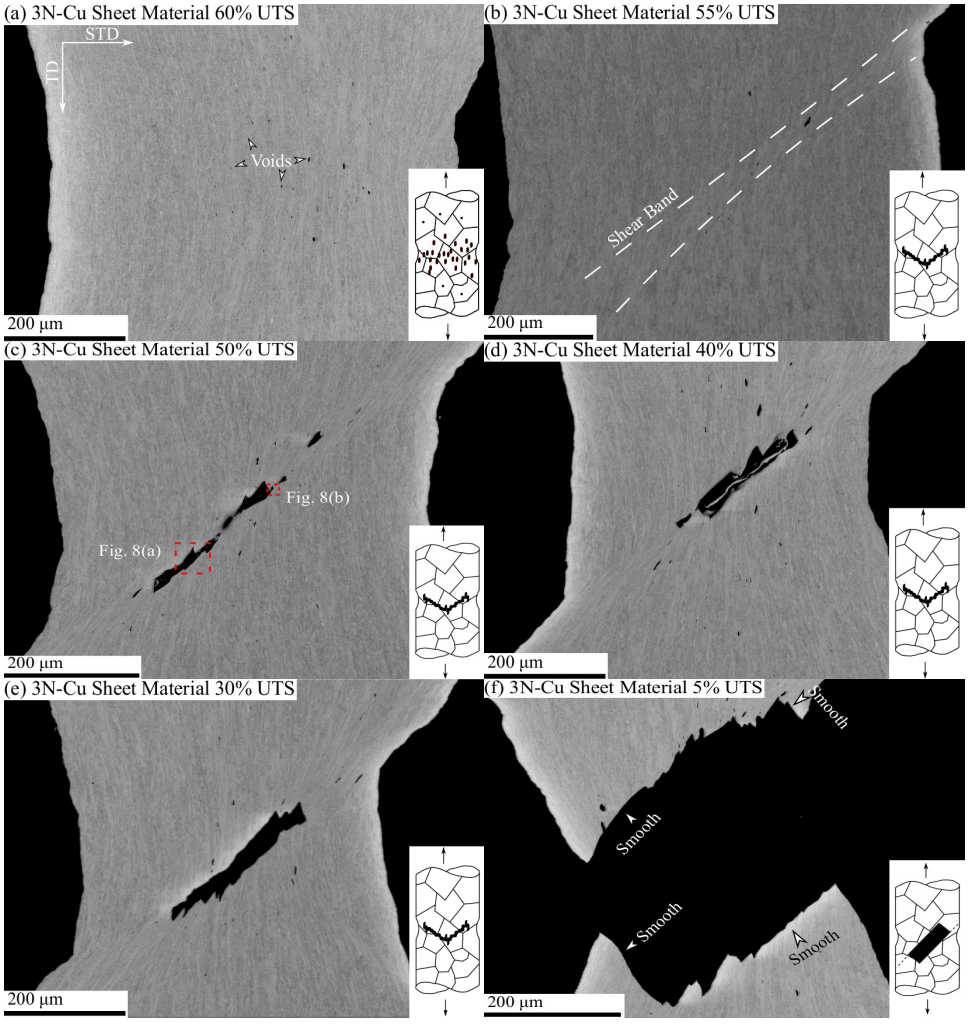


**Figure 7: The fracture process in the 3N-Cu sheet material is illustrated using images from midplane cross sections of six different specimens that were interrupted at (a) 60%, (b) 55%, (c) 50%, (d) 40%, (e) 30%, and (f) 5% of the UTS. The sketches overlaid on each image highlight the dominant fracture mechanism at this point in the fracture process: (a) void nucleation and growth by intervoid necking in the diffuse neck, (b) the nucleation of new voids in the shear band by void sheeting, (c) to (e) void coalescence by void sheeting, and (f) the final fracture of this material by the OAS mechanism.**

A macroscopic shear band formed in the 3N-Cu sheet material at approximately 55% of the UTS. This can be seen in Figure 7(b). When the shear band intersected existing voids in the diffuse neck, these voids were deformed along the axis of shear (which made an angle of about 45° with the TD). Voids that nucleated within the shear band were also elongated along the shear axis. Shortly after the shear band formed, many of the voids within it coalesced to form a series of jagged cavities. This is shown in Figure 7(c). The jagged edges of the cavity were created when voids coalesced along the shear band, as Figure 8(a) highlights. To understand the mechanism of void coalescence in this material, the interiors of the cavities shown in Figure 7(c) were inspected. This was done by tilting this specimen 70° about its STD and imaging it in secondary electron mode. An image of the inside of this cavity is provided in Figure 8(b). Shear dimples were seen along the edge of this cavity, indicating that void sheeting occurred. Further evidence of void coalescence by void sheeting was seen on the fracture surface of 3N-Cu sheet specimens. A plan-view of the fracture surface of a fractured 3N-Cu sheet specimen is shown in Figure 9. As Figure 9(b) shows, the ligaments between the tensile dimples were covered in small shear dimples, indicative of void sheeting.

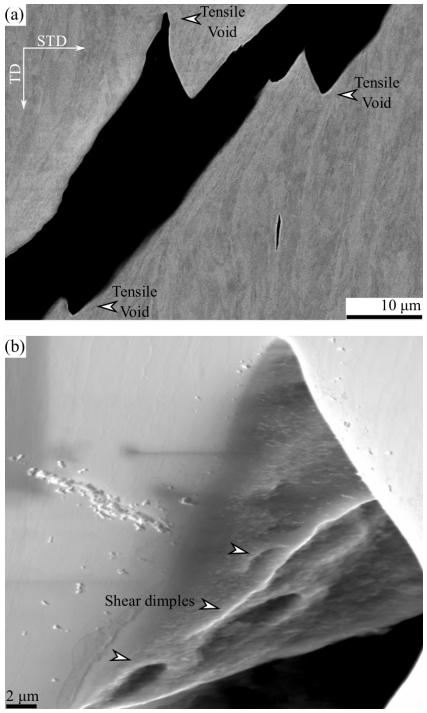


**Figure 8: High-magnification images of the cavity shown in Figure 7(c) are provided. For reference, the areas presented in (a) and (b) are labeled in Figure 7(c). The image in (a) highlights the tensile voids on either side of the cavity that coalesced to form the cavity. The secondary electron image in (b), taken after this specimen was tilted 70 about its STD, shows that these tensile voids coalesced by void sheeting. This is evidenced by the rows of shear dimples on the sides of the cavity.**

Void coalescence by void sheeting eventually created large, prismatic cavities in the center of 3N-Cu sheet specimens. Examples of this can be seen in Figure 7(d) and (e), which show images of specimens interrupted at 40% and 30% of the UTS, respectively. Once such a cavity grew by void sheeting to span approximately half of the shear band, it began to grow into material that was essentially void-free. At this point, void sheeting effectively ceased, and the final stages of cavity growth were controlled by the OAS mechanism. Evidence of this can be seen in the image provided in Figure 7(f),

which shows the midplane cross-section of a specimen whose deformation was interrupted at 5% of the UTS. Near the center of the sheet, the edges of this cavity were serrated, evidence that it formed by void nucleation and coalescence. However, near the surface of the sheet, the edges of the cavity were mostly smooth, indicating that it grew by the OAS mechanism. Images of the fracture surface of 3N-Cu sheet specimens support this conclusion. As Figure 9(c) reveals, the slanted edges of the fracture surface were almost completely dimple-free. In summary, the fracture process in the 3N-Cu sheet material was a 3-step process involving void nucleation and growth by intervoid necking, void coalescence by void sheeting to form prismatic cavities, and the growth of these cavities by the OAS mechanism.

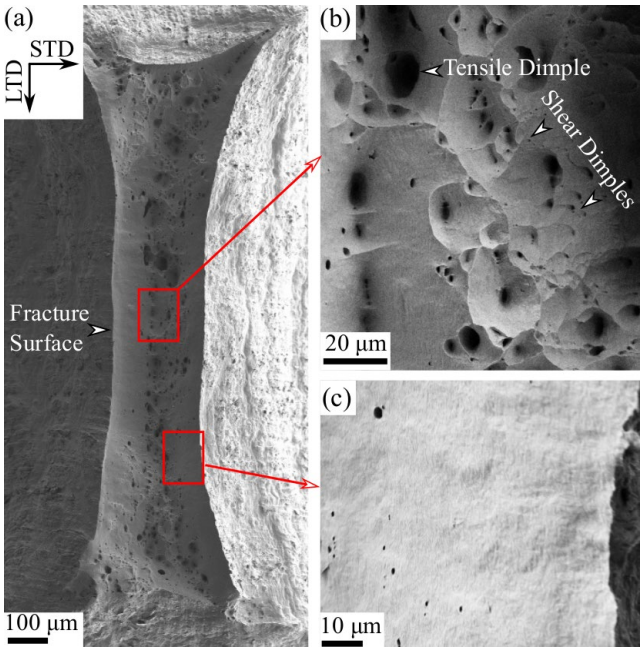


**Figure 9: A macrofractograph of a ruptured 3N-Cu sheet specimen is shown in (a). The images in (b) and (c) are high-magnification images of the areas highlighted in (a). These images show that the center of the fracture surface is covered with tensile dimples whose ligaments are covered in shear dimples. However, the slanted edges of this fracture surface are essentially dimple-free, evidence that central cavities grew by the OAS mechanism.**

Fracture in the 4N-Ni material was also a three-step process:

1. the material began to fail by single-plane catastrophic shear along a single shear band,
2. large, prismatic cavities then formed near the sheet center when voids coalesced within the shear band by intervoid shearing, and
3. the material failed when these cavities grew by the OAS mechanism until final specimen separation.

This process is illustrated in Figure 10 and is described in more detail in the following paragraphs. A macroscopic shear band formed in this material at approximately 50% of the UTS. This can be seen in Figure 10(a). Voids nucleated exclusively within this shear band; no voids were observed outside of this shear band or in specimens whose deformation was interrupted before a shear band formed. During deformation between 50% and 25% of the UTS, the two specimen halves on either side of the shear band gradually moved past each other along the shear band. This is best seen by comparing the images of 4N-Ni sheet specimens interrupted at 50% and 25% of the UTS provided in Figure

10(a) and (b). The process of single-plane catastrophic shear eventually created a small crack on one side of 4N-Ni sheet specimens, as Figure 10(b) shows.

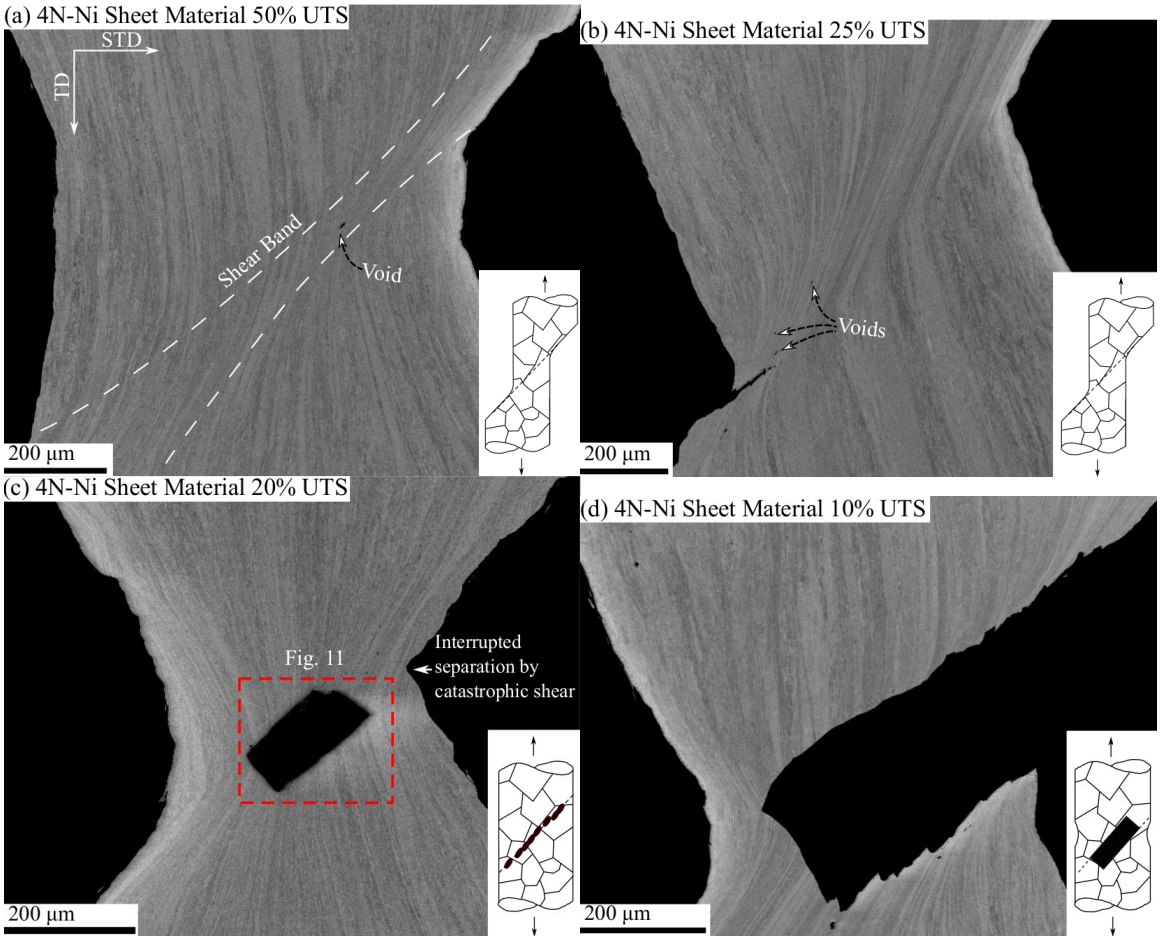


**Figure 10: The fracture process in the 4N-Ni sheet material is illustrated using images from the midplane cross sections of four different specimens that were interrupted at (a) 50%, (b) 25%, (c) 20%, and (d) 10% of the UTS. The sketches overlaid on each image highlight the dominant fracture mechanism at this point in the fracture process: (a) the formation of a macroscopic shear band, (b) the two halves of the material catastrophically shearing past each other, as can be seen by comparing this image with that in (a), and the nucleation of voids in the shear band, followed by the coalescence of these small voids leading to (c) the formation of a central cavity by intervoid shearing, and (d) the growth of this cavity by the OAS mechanism. From these images, it appears that the transition from single-plane catastrophic shear to intervoid shearing occurred suddenly, though it is likely that the catastrophic shear process enabled void coalescence by elongating the voids along the shear axis.**

Failure by single-plane catastrophic shear was interrupted by the formation of large, prismatic cavities in the center of 4N-Ni specimens at about 20% of the UTS. One of these cavities can be seen in Figure 10(c). Two approaches were used to understand how such cavities formed. First, the interior of the cavity shown in Figure 10(c) was inspected by tilting this specimen 70° about its STD and characterizing it using secondary electron imaging. Images of the inside of the cavity are provided in Figure 11. Two distinct regions were observed along the sides of this cavity and are highlighted in Figure 11. Near the center of the cavity, rows of shear dimples were observed, see particularly Figure

11(b). This suggests that the cavity formed when voids coalesced by intervoid shearing. Alternatively, most of the sides of the cavity were smooth and dimple-free. This indicates that, once formed, the cavity grew by the OAS mechanism. Further evidence that prismatic cavities formed by intervoid shearing and grew by the OAS mechanism was observed on the fracture surface of 4N-Ni sheet specimens. A macrofractograph of a fractured 4N-Ni specimen is shown in Figure 12. As the image in Figure 12(b) highlights, the center of the specimen was covered with rows of parallel dimples that were separated by smooth ligaments. This suggests that cavities formed by void nucleation and coalescence and subsequently grew by the OAS mechanism.

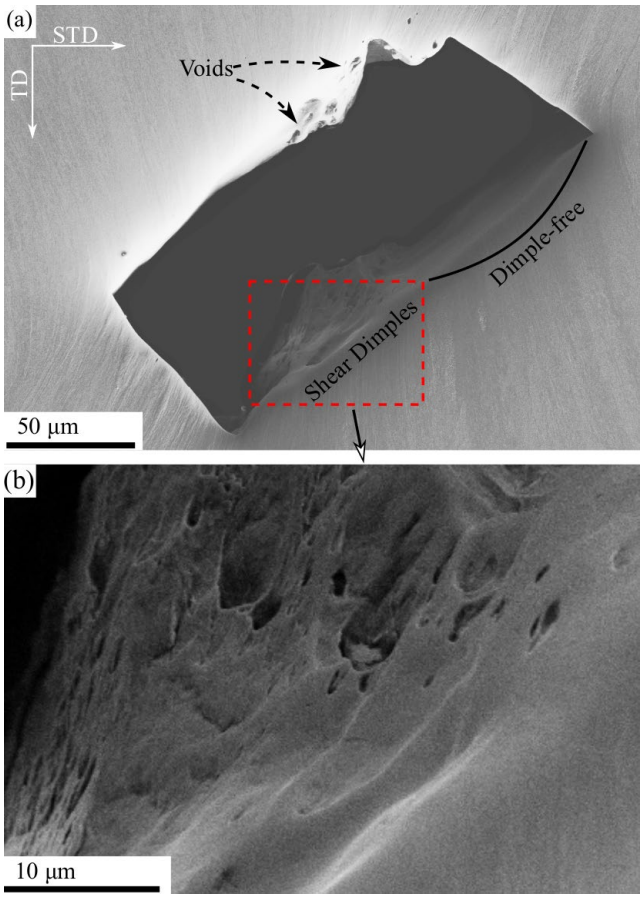


**Figure 11: Secondary electron images of the interior of the cavity shown in Figure 10(c) are provided. These images were taken after the specimen was tilted 70 about its STD to allow the interior of this cavity to be imaged. These images highlight the portions of the edges of the cavity that were either covered in shear dimples or were dimple-free.**

Once a series of prismatic cavities formed, the final stages of fracture in this material were controlled by the growth of these cavities by the OAS mechanism. This can be seen in Figure 10(d). This figure shows an image of a specimen interrupted at 10% of the UTS. A large prismatic cavity spanned most of the thickness of this specimen. As Figure 10(d) highlights, the sides of this cavity were jagged near the sheet center, suggesting that it formed by void coalescence. The edges of the cavity were smooth indicating that much of its growth was controlled by the OAS mechanism. Similarly, the slanted edges of the fracture surface shown in Figure 12(c) are essentially dimple free, indicating that cavities grew along shear bands by the OAS mechanism. In summary, the fracture process in the 4N-Ni sheet

material was a 3-step process involving single-plane catastrophic shear, void nucleation and coalescence by intervoid shearing to form prismatic cavities, and the growth of these cavities by the OAS mechanism.

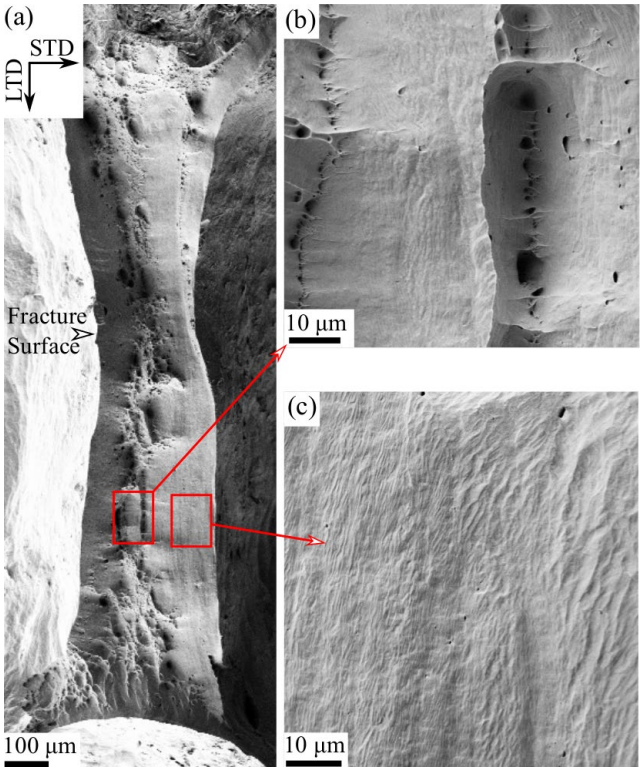


**Figure 12: A macrofractograph of a ruptured 4N-Ni sheet specimen is shown in (a). The images in (b) and (c) are high-magnification images of the areas highlighted in (a). These images show that the center of the fracture surface was covered with approximately parallel rows of dimples while the edges were essentially dimple-free.**

## 1.4. Discussion

Currently, phenomenological fracture models either consider void nucleation, growth, and coalescence [36, 41] or failure by shear-localization [54, 65, 75] and assume that a combination of these mechanisms dominates rupture. It is thus generally held that the fracture mechanism will only change when the local stress state changes, such as when strain localizes to form a shear band in the necked gauge region of a tensile bar. However, the results of this study show that this assumption is false: failure can be controlled by as many as seven different mechanisms. These seven mechanisms are not always distinct and sometimes act in concert or competition with one another. Indeed, for a given stress state and material, multiple mechanisms often work together in a sequential manner to cause fracture. This study provides the first report of how these different mechanisms interact with one another and of the factors that control the competition between them

### *1.4.1. Damage mechanisms facilitate subsequent fracture mechanisms*

The fracture process in the 4N-Ni sheet (see Figure 10 and **Error! Reference source not found.**) demonstrates that fracture mechanisms can be facilitated by preceding mechanisms. Failure in this material began with single-plane catastrophic shear, progressed to void coalescence by intervoid

shearing, and ended when central cavities grew by the OAS mechanism to span the specimen cross-section. Each fracture mechanism was facilitated by the mechanism(s) that preceded it. Single-plane catastrophic shear gradually brought voids in the shear band closer together until they coalesced by intervoid shearing. Intervoid shearing then created a central, prismatic cavity at the center of the shear band. This cavity was well-positioned to grow by the OAS mechanism along the shear band created by single-plane catastrophic shear.

The sequential fracture processes in the 4N-Ni wire and 3N-Cu sheet materials also illustrate how one failure mechanism can facilitate subsequent mechanism(s). In the 4N-Ni wire material, catastrophic shear was impeded by the cylindrical geometry and voids nucleated throughout the diffuse neck. When some of the voids in the center of the neck coalesced to form a central cavity, strain subsequently localized in shear bands near the edges of the specimen. Preexisting voids that were intersected by these shear bands then coalesced by intervoid shearing to cause fracture. In the 3N-Cu sheet material, void sheeting created a cavity in the center of the shear band that was then well-positioned to grow by the OAS mechanism. These results demonstrate that the seven fracture mechanisms presented in Figure 2 may act in concert to cause fracture. Phenomenological models of fracture must thus capture the interplay between different fracture mechanisms and the stress state and material.

### *1.4.2. The competition between fracture mechanisms: the effects of microstructure and strain-hardening capacity*

The competition between the seven failure mechanisms presented in Figure 2 depends not only on the local stress state but also on the microstructure and the strain-hardening capacity. In particular, this study shows that:

1. the competition between the void-based and void-free mechanisms shown in Figure 2, *i.e.* the competition between mechanisms (a) to (d) and (e) to (g), is microstructure-dependent, and
2. the competition between intervoid shearing and void sheeting depends on the strain-hardening capacity.

The present investigation demonstrates that microstructural evolution during deformation can influence the fracture process by eliminating and/or creating void-nucleation sites. Because void nucleation depends on the volume-density of sites at which voids can nucleate in the material, previous studies have examined the relationship between the volume-density of second-phase particles and the fracture mechanism [17, 63]. However, a recent study of void nucleation in high-purity Tantalum (a body-centered cubic (BCC) metal) demonstrated that, in some cases, voids can also nucleate at deformation-induced dislocation boundaries [71]. It is conjectured that voids in the nickel materials likely nucleated at similar features, which are known to form during plastic deformation of high-purity FCC metals [76]. Voids in the copper materials may have nucleated at similar microstructural features or at the ≈200 nm and ≈500 nm inclusions observed, respectively, in the Cu sheet and wire materials. Alternatively, in the high-purity aluminum materials, dynamic recrystallization eliminated deformation-induced dislocation boundaries. Presumably, grain boundaries were then the only remaining microstructural feature at which voids could nucleate in these materials. In the 5N-Al wire, most of the grain boundaries were eliminated by dynamic recrystallization. Thus, in this case, microstructural evolution during loading eliminated most of the microstructural features at which voids could nucleate. On the other hand, the dynamically recrystallized grain size in 5N-Al sheet material was similar to the as-received grain size. Voids may have nucleated at grain boundaries in this material, and subsequently grew and coalesced, leading to failure.

The primary void-coalescence mechanism during shear-dominant loading depends on the strain-hardening capacity. In particular, a low strain-hardening capacity favors void coalescence by intervoid shearing while a high strain-hardening capacity favors void coalescence by void sheeting. This relationship was evident from the different void-coalescence mechanisms observed in the 4N-Ni and 3N-Cu sheet materials, *i.e.* intervoid shearing and void sheeting. Teirlinck *et al.* [9] argued that such a relationship must exist since void coalescence by intervoid shearing can only occur when strain hardening within the shear band can no longer compensate for the increased shear stress associated with a loading increment. Based on this argument, they proposed that the propensity for void sheeting depends on the strain-hardening constants ($m$ and $A$), the von Mises stress ($\bar{\sigma}$), the density of spherical voids per unit volume $N_v$, and the average void volume ($V$) as

$$m\left(\frac{A}{\bar{\sigma}}\right)^{1/m} = VN_v \qquad (3)$$

To elucidate this proposed model, Figure 13 presents a plot of $VN_v$ as a function of $\bar{\sigma}$ for copper and nickel. As discussed in the introduction, intervoid shearing is controlled by void *growth* while void sheeting is controlled by void *nucleation*. Previous studies indicate that voids grow by slip [77, 78, 79, 80]. While the factors that control void nucleation are still poorly understood [25, 30, 55, 59], it is presumed that it depends on some combination of the local stress and strain states and the local density of dislocations and vacancies [48, 71, 81]. Hence, in materials where strain hardening impedes slip, void nucleation rather than void growth may control the rate of void coalescence. Depending on the kinetics of void nucleation, *i.e.* the local density of void nucleation sites and the rate at which they are activated, this may result in a significant increase in the amount of shear strain a material can accept before fracture. Alternatively, in materials with a low strain-hardening capacity, when a small volume fraction of voids nucleates, failure likely occurs almost immediately after a state of localized shear develops. This may explain why shear localization is sometimes observed to coincide with fracture in materials with low strain-hardening capacities that already contain a significant volume fraction of voids [17, 54].

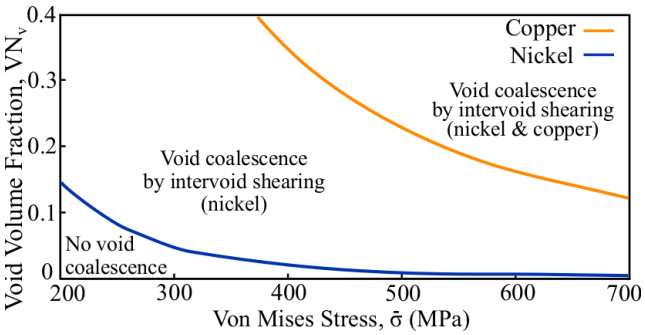


**Figure 13: Plots of void volume fraction ($VN_v$) versus the von Mises stress ($\bar{\sigma}$) at which void coalescence by intervoid shearing occurs for nickel and copper are shown. These plots are based on equation $m\left(\frac{A}{\bar{\sigma}}\right)1/m = VN_v$ ( *3* ) [9]. Because copper has a much larger strain-hardening capacity than nickel, equation $m\left(\frac{A}{\bar{\sigma}}\right)1/m = VN_v$**

### *1.4.3. Relating rupture mechanisms to phenomenological fracture models*

The present observations suggest that phenomenological fracture models should describe failure as a sequential process controlled by multiple mechanisms rather than by a single, dominant mechanism. Fundamentally, the competition between these mechanisms and the transition from one mechanism to another depends on the local stress state, the resistance to void nucleation, the resistance to void

growth, and the intrinsic plastic flow behavior of the material. The results of this study suggest that the resistance to void growth is related to the strain-hardening capacity of the material, though other factors likely also play a role. Void nucleation is, however, much more poorly understood. At present, many fracture models simply assume a pre-existing void fracture [23, 32, 42]. More advanced approaches randomly seed the material with voids as a function of global stress or strain [48, 82]. These results indicate that the fracture mechanism is significantly influenced by both when and where voids nucleate. Consider, for example, the sequence of fracture mechanisms in the 3N-Cu sheet material. Before a shear band formed, voids primarily nucleated near the center of the sheet. These voids subsequently coalesced by void sheeting to form a central cavity. Void sheeting did not control the final stage of failure, though, because very few voids nucleated near the edges of the sheet. The final stages of fracture were instead controlled by the growth of prismatic cavities into material that was nearly void-free, *i.e.* the OAS mechanism. If, on the other hand, voids had nucleated more readily throughout the cross-section, it is likely that void sheeting would have caused specimen separation. Current approaches to modeling void nucleation are thus generally insufficient to predict which fracture mechanism or sequence of mechanisms controls failure.

In addition, because the effects of one mechanism can enable and/or suppress others, the entire series of fracture mechanisms must be predicted to accurately model failure. This is a challenging task. A failure mechanism map in stress triaxiality/true reduction in load bearing area space may be able to provide a first-order approximation of which mechanisms could contribute to failure for a given material. True reduction in load bearing area is here defined as the reduction in area from necking and/or shear deformation plus the void area fraction in the thinnest ligament. Examples of two such maps are provided in Figure 14. The map in Figure 14(a) is loosely based on the observed failure sequence in the 4N-Ni materials, which had a high resistance to void nucleation and a low resistance to void growth. Alternatively, the map in Figure 14(b) shows an example of the failure process in a material in which void nucleation is almost entirely suppressed, such as the 5N-Al wire material used in this study. For a given material, such maps could be used to predict the transition from one fracture mechanism to another. It is important to note, though, that this approach has the serious downsides of capturing neither the importance of where voids nucleate nor how different mechanisms enable one another. In addition, it can only be related to failure strain if the relative ductilities of different fracture mechanisms have been determined. In the end, these aspects must be included before the entire sequence of fracture mechanisms can be predicted.

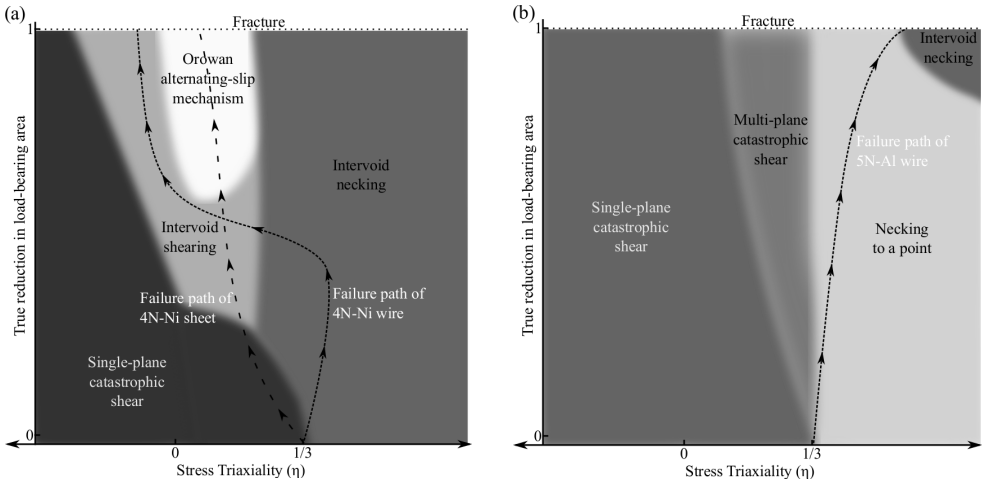


**Figure 14: Two examples of fracture mechanism maps are provided. The map in (a) is loosely based on the observed failure sequence in the 4N-Ni materials, which had a high resistance to void nucleation and a low resistance to void growth. The map in (b) shows an example of the failure process in a material in which void nucleation is almost entirely suppressed, such as the 5N-Al wire material used in this study.**

## 1.5. Summary and Conclusions

Current approaches to studying ductile fracture generally assume that failure is controlled by void growth and coalescence through either intervoid necking or intervoid shearing. Phenomenological models that incorporate a mechanistic approach to fracture have focused on how the stress state influences the rates of and competition between these two mechanisms [20, 21, 36, 44, 83]. While these approaches are useful, they disregard the fact that fracture can be controlled by at least seven different mechanisms. In this study, the interaction between these different failure mechanisms was investigated by characterizing the fracture of high-purity aluminum, nickel, and copper. Unlike previous studies, the entire failure process in these materials from the formation of a diffuse neck to final specimen separation was examined. These observations demonstrated the following:

a) The failure process frequently involves a progression of several mechanisms in a sequential manner. When this occurs, one failure mechanism often facilitates the mechanisms that come after it.
b) The microstructural evolution that occurs during deformation prior to failure can either eliminate or create void-nucleation sites in the material. This can significantly influence the competition between different failure mechanisms. The creation or elimination of void nucleation sites by microstructural evolution is particularly important in materials where void nucleation at second-phase particles is suppressed, as is the case in high-purity materials and materials with small, well-bonded second-phase particles.
c) The competition between intervoid shearing and void sheeting depends on the strain-hardening capacity, with a low strain-hardening capacity favoring intervoid shearing and a high strain-hardening capacity favoring void sheeting.
d) It is hypothesized that the reported discrepancies in strain-to-failure under shear-dominated loading are due not only to differences in the spatial resolution of strain measurements but also to differences in dominant mechanism for a particular material/condition and under-representation of the multiple mechanisms that can contribute to failure. To accurately predict

fracture, the complex interplay between different fracture mechanisms, material properties, and the microstructure must be understood and modeled.

# 2. THE MICROMECHANICS OF VOID NUCLEATION

Ductile rupture in metals is a phenomenon that affects a wide range of applications from forming of automotive body panels to failure of solder joints in microelectronics. The incipient stage involves the formation of internal voids, a critical transition state which is difficult to predict. Early observations on ductile rupture have led to several conflicting or competing models which describe the nucleation phase. The present review distinguishes the nucleation process based on the microstructural features which can trigger nucleation: second-phase particles, grain boundaries, and dislocation cell boundaries. For each of these features, a review of observations leads to a critical assessment of modeling approaches. Specifically, the role of defect-defect interactions on processes such as vacancy condensation can help to rationalize known controlling factors such as the role of stress-state and strain accumulation on the void nucleation processes. As a result of this review, it is possible to define critical experiments and model developments that will enable improved prediction of ductile rupture processes and design of damage-tolerant materials.

## 2.1. Introduction: Early concepts and misconceptions

More than seventy years after Constance Tipper proposed that ductile failure is a multi-step process consisting of void nucleation, growth, and coalescence [72], failure predictions for metallic components remain challenging. At the core of the problem, there is lack of consensus on the governing conditions and mechanisms for the incipient nucleation of damage in metals. Historically, modeling and experimental efforts have focused on void growth and coalescence, particularly under high-triaxiality conditions [2, 31, 32]. These efforts have produced well-validated models for the response of a porous, ductile material loaded in tension [33, 84, 85]. However, such models invariably assume that the material contains a preexisting distribution of voids or that voids nucleate at a critical stress and/or strain. Void nucleation in these models is thus mechanism-agnostic. An increasing number of studies have demonstrated, though, that the distribution and morphology of incipient voids can profoundly influence many aspects of failure, including strain-localization and the failure mechanism [48, 59, 86, 87, 88]. Accurately modeling void-nucleation is thus critical to predicting the mechanical integrity of metallic structures.

Before considering how voids form, it is first necessary to define what a void is in the context of ductile rupture and, hence, what it means for a void to nucleate. There are two interrelated requirements before an incipient void (e.g., a microcrack or vacancy cluster) nucleates and becomes a failure-relevant void: it must be stable, and it must grow within an experimentally relevant time-scale such that it precipitates into failure. By stable, we mean that the incipient void cannot dissipate away (e.g., vacancy cluster disperses) or collapse into another defect (e.g., a dislocation loop). Stability depends on many factors, including the local stress state, temperature, and the mechanism(s) that control the initial stages of growth. For instance, microcracks formed during tensile deformation may collapse if the part is subsequently loaded in compression. With respect to the second requirement for nucleation, the void growth rate is dependent upon the growth mechanism. One common hypothesis is that voids grow by dislocation nucleation, in which case a void is considered to have nucleated when it is large enough to nucleate dislocations [84]. However, it was recently shown that void growth by dislocation emission is probably not realistic during quasistatic testing conditions [82]. If voids instead grow by absorbing dislocations, a void can be regarded as nucleated when the dislocation population around it is sufficient to sustain its growth. Vacancy clusters or microcracks smaller than this critical size would be annihilated by a gliding dislocation [89]. Clearly there is no simple and universal definition, in terms of a critical size or microstructural state, for when a void is considered to

"nucleate." The specific microstructural features and associated mechanisms must be taken into account.

Despite the ambiguity around when a void is said to nucleate, it is well established that void nucleation is driven by plastic deformation and often occurs where this process is inhomogeneous, *e.g.* at second-phase particles, non-metallic inclusions, or grain boundaries [90]. The subsequent growth and coalescence of these voids creates the classic "dimpled" fracture surface presented in Figure 15. While voids are widely assumed to originate at particles or inclusions, populations of particle-free dimples filling a spectrum of length scales are also observed on the fracture surfaces of many materials [91]. Proposed void nucleation mechanisms, summarized in Table 4 and Figure 16, include both particle-stimulated and particle-free mechanisms. As Figure 16 illustrates, these mechanisms can produce incipient voids with significantly different morphologies.

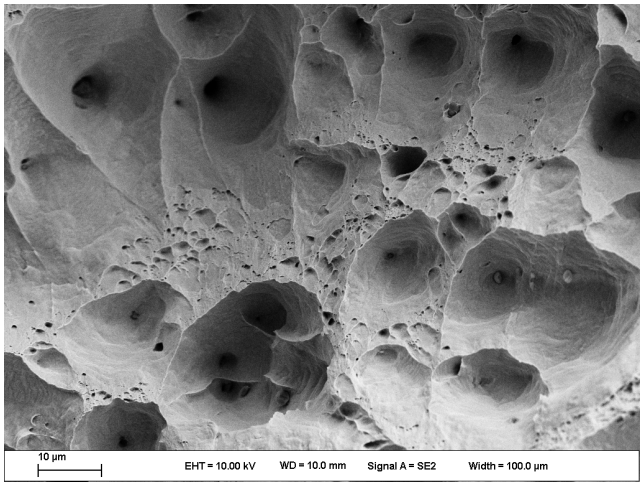


**Figure 15. An SEM image of the fracture surface of a wrought Nickel 200 specimen exhibiting the classic "dimpled" fracture surface is shown. Dimples spans a large spectrum of length scales in metals, and small dimples in many materials are not always associated with particles or inclusions.**

To date, the vast majority of studies on void nucleation have focused on particle-stimulated void nucleation. Classically, the critical conditions for particle-stimulated void nucleation have been addressed in terms of the mechanical conditions at the particle/matrix interface. For example, many studies have examined the relationship between the local stress state and particle delamination [92, 93]. This perspective has been covered extensively in prior reviews of void nucleation (see References [59, 94, 95, 96] for classic perspectives and References [57, 97] for more recent treatments of the topic). These results are summarized in Section 3.

The specific microstructural configuration that gives rise to the nucleation event are, however, generally ignored, both for the case of particle-stimulated and particle-free void nucleation. Modern experimental observations and computational tools indicate, though, that void nucleation results from specific defect-defect interactions. Here, by defect-defect interactions we mean interactions between the various deformation-related defects, such as vacancies, dislocations, twins, and deformation-induced phases, and with other microstructural defects, such as second-phase particles and grain boundaries. In an alternative approach to prior reviews of void nucleation, the focus of the present study is on the role of defect interplay during void nucleation. Particular focus is drawn to the insights

provided by modern characterization and computational tools such as electron backscatter diffraction (EBSD), X-ray microtomography, and atomistic simulations. Three general cases are discussed: void nucleation at particles (Section 4.1), at grain boundaries (Section 4.2), and at deformation-induced dislocation boundaries (Section 4.3). Particular attention is given in this section to void nucleation by vacancy condensation, which received limited attention in previous reviews of room-temperature ductile fracture. While the focus of this review is on void nucleation during quasistatic deformation at temperatures less than approximately one-third the melting temperature, void nucleation is also sensitive to both temperature and strain rate. The effects of these external factors on void nucleation are briefly discussed in Section 5.

**Table 4: A brief summary of the five proposed void-nucleation mechanisms is provided.**

| Void nucleation mechanism | Favored by | Nucleation Criteria |
|---|---|---|
| Particle fracture | • Large, brittle particles<br>• Low interfacial energy<br>• High interfacial strength | • Local stress<br>• Particle toughness/strength |
| Particle decohesion | • Small, ductile particles<br>• High interfacial energy<br>• Low interfacial strength | • Local stress<br>• Interfacial energy |
| Grain boundary cleavage | • Materials with limited and localized plasticity (*e.g.*, HCP metals)<br>• High interfacial energy | • Interfacial energy<br>• Local stress<br>• Local defect content<br>• Grain boundary geometry<br>• Active slip system(s) |
| Vacancy condensation | • Elevated temperatures (high vacancy diffusivity and concentration)<br>• Vacancy production via cold working | • Vacancy concentration<br>• Local dislocation density<br>• Hydrostatic stress |
| Dislocation boundary decohesion | •High misorientation dislocation boundaries | •Local dislocation density<br>•Local strain/stress |

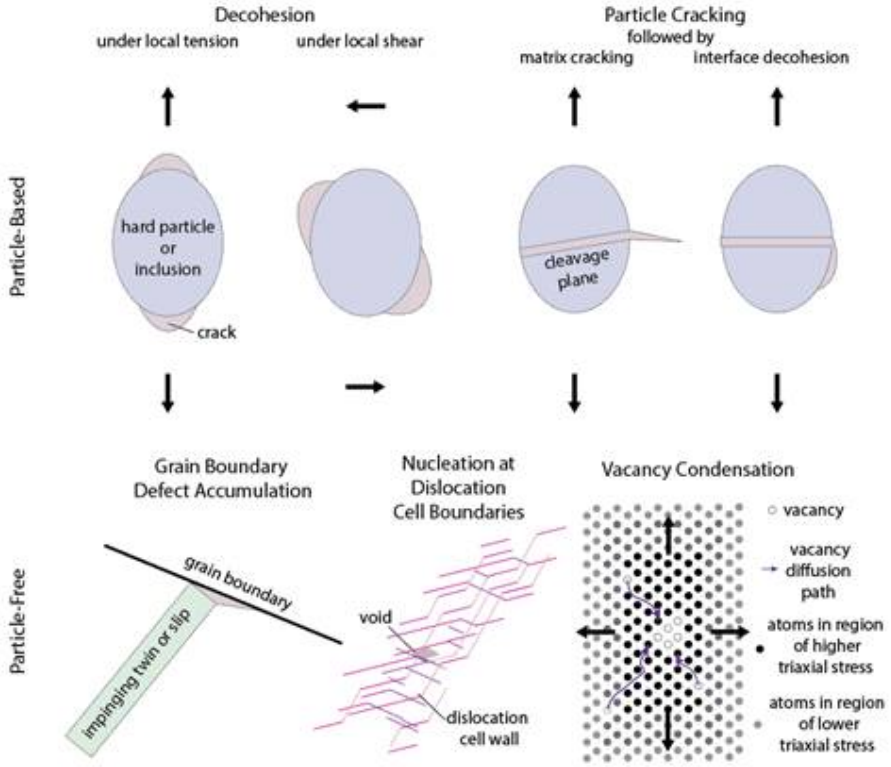


**Figure 16.** Schematic illustrations for mechanisms of void nucleation involving hard particles (top row) or at other microstructural features (bottom row).

## 2.2. A brief review of the mechanical conditions that enable nucleation at 2nd-phase particles

Second-phase particles and inclusions can play two distinct mechanistic roles in ductile void nucleation, producing voids *via* particle cracking or *via* interfacial decohesion [98]. Classic reviews of particle-stimulated void nucleation [12, 99, 100, 101] present *post-mortem* microscopy of fractured or debonded particles and discuss how particle size, shape, and volume density affect the critical stress and strain for void nucleation. Recent reviews of ductile fracture by Pineau *et al.* [81, 97] also include data from recent *in-situ* X-ray tomography and scanning electron microscopy (SEM) studies on the mechanical conditions for void nucleation. These reviews primarily focus on the local mechanical condition for void nucleation in particles. This section summarizes these results and presents data from *in-situ* X-ray microtomography studies not covered in prior reviews.

Decades of study have examined the relationship between particle and matrix properties and the competition between particle fracture and delamination. The general trend that small, spherical particles tend to delaminate while large, elongated particles tend to fracture has been observed in many materials [102, 103, 104], though exceptions to this trend have been observed during *in-situ* SEM experiments [105]. The relationship between these parameters and the critical strain for void nucleation has also been studied in many alloy systems. Table 5 summarizes how increasing a given

parameter affects the critical strain for void nucleation for a given nucleation mechanism. As noted in these tables, strong relationships have been established between some parameters and the critical strain for nucleation, while the effects of other parameters remain unclear. For instance, Goods and Brown [102] proposed that the critical strain for delamination is a linear function of the particle radius, Tanaka *et al.* [104] hypothesized that it is inversely proportional to the square root of the radius, and Argon and Im reported that particle size had no effect on particle decohesion in materials with low particle volume fractions [102, 106].

**Table 5: For each of the parameters listed, the arrow indicates if increasing this parameter increases or decreases the critical strain for void nucleation by particle decohesion or by particle cracking.**

| Parameter | Decohesion | Cracking |
|---|---|---|
| Interfacial strength | ↑ | No effect |
| Particle size | Effects unclear | ↓ |
| Particle elongation | No effect | ↓ |
| Particle volume fraction | ↓ | ↓ |
| Stress triaxiality | Effects unclear | No effect |
| Matrix strength | Likely ↓ | ↓ |

With respect to the influence of stress triaxiality, X-ray tomography experiments are providing new insights into how this parameter affects particle-stimulated void nucleation. However, the relationship between stress triaxiality and particle-stimulated void nucleation still remains unclear. Historically, this relationship has been investigated by comparing the ductility of notched and unnotched tensile bars [107, 108]. The result that void nucleation generally occurs at lower strains in notched bars than unnotched is confounded by the fact that both the stress triaxiality and the mean stress are larger in a notched specimen than an unnotched specimen. It is now possible, though, to combine experimental characterization from *in-situ* X-ray tomography with finite element (FE) analysis to evaluate the local stress triaxiality at void nucleation. Babout *et al.* [13] investigated this relationship for both delamination and fracture of spherical $ZrO_2/SiO_2$ particles in a matrix of pure Al and a matrix of Al 2124, respectively. Decohesion appeared to depend on the local stress field at the particle interfaces [105], with particle fracture consistently occurring at a critical normal stress of 700 MPa regardless of the stress triaxiality. This suggests that particle fracture depends simply on the magnitude of the normal stress applied to the particle-matrix interface, not the overall stress state.

X-ray tomography also showed that particle fracture depends more strongly on particle morphology than on particle size. In a SiC particle-reinforced 2080 Al alloy, Chawla and coworkers [15] examined the relationship between particle fracture, size, and morphology, examining over 1500 particles. A plot from this study showing the fracture probability as a function of both size and aspect ratio is provided in Figure 17. For a particle of average aspect ratio, the probability of fracture ranged from 10% for the smallest particles to 30% for the largest particles. In contrast, for a particle of average size, the probability of fracture ranged from 20% for particles with the smallest aspect ratio to 60% for particles

with the largest aspect ratio. These data thus indicate that particle morphology is a critical factor when considering particle fracture.

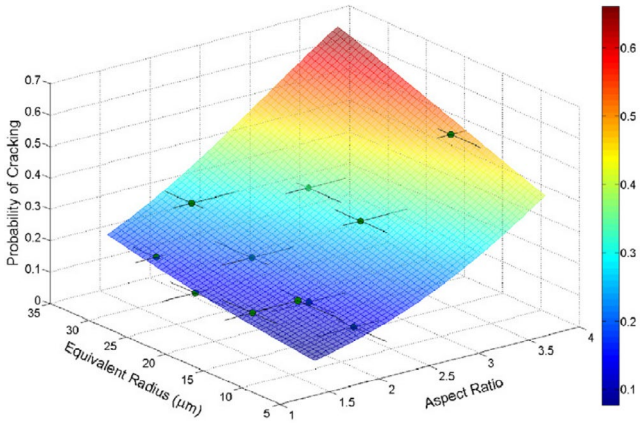


**Figure 17. A 3-D probability plot of particle cracking for SiC particles in an Al 2080 matrix. The probability of fracture increases both with increasing aspect ratio and radius but is a stronger function of aspect ratio than radius. This plot is from reference [15].**

## 2.3. The influence of defect-defect interactions on void nucleation

In this section, we discuss the local defect states in the microstructure that serves as seed sites for void nucleation. While it has long been assumed that void nucleation is enabled by local plastic deformation at specific material heterogeneities [46], little attention has been given to the specific relationships between void nucleation and defect-defect interactions. In recent decades, the emergence of characterization tools such as EBSD and X-ray tomography, combined with advances in computational tools, have allowed these interactions to be studied in detail for the first time. This section reviews these works for the following three general cases:

1. void nucleation at second-phase particles and inclusions,
2. void nucleation at grain boundaries, and
3. void nucleation at deformation-induced dislocation boundaries.

For each case, experimental observations are first presented, followed by a discussion of relevant theories and models.

### *2.3.1. Void nucleation at second-phase particles*

It has long been assumed that the mechanical drivers for particle-stimulated void nucleation are created by local plastic deformation at or near the particle/matrix interface. The local deformation around particles is often highly heterogeneous and depends on many factors. For instance, Humphreys and coworkers [109, 110] demonstrated that the lattice rotation accommodated by dislocation boundaries near silica particles in a Ni matrix increases with particle size.

Until recently, characterizing these defect states, either experimentally or computationally, was a significant challenge. Using modern computational and experimental tools, significant progress has been made in the past three decades in evaluating the defect structures created by plastic deformation. Our modern understanding of deformation-induced dislocation boundaries, based on the low energy dislocation structures (LEDS) hypothesis [107, 111], suggests that classic assumptions about dislocation pileups at the particle/matrix interface leading to void nucleation are invalid. After a short review of early studies on the relationship between twinning and particle-stimulated void nucleation, we briefly discuss this new perspective on deformation-induced dislocation boundaries. In this context, recent experimental observations and computational models of both particle fracture and decohesion are presented.

#### 2.3.1.1. Experimental Observations

Evidence that deformation-related defects strongly impact nucleation has been observed in a number of material systems. In materials that deform by twinning, void nucleation is often associated with twin/particle intersections. Beevers and coworkers demonstrated that specific twin types are associated with fracture of hydride platelets in zirconium [6]. Both $\{10\bar{1}2\}$ and $\{11\bar{2}\bar{1}\}$ twinning was observed, but fractured platelets were only associated with $\{11\bar{2}\bar{1}\}$ twins. Several studies of void nucleation in steel have also observed that twin/particle intersections are preferential sites for particle fracture [112, 113] . An example of twins intersecting cracked grain-boundary particles in a Fe-3% Si steel is shown in Figure 18.

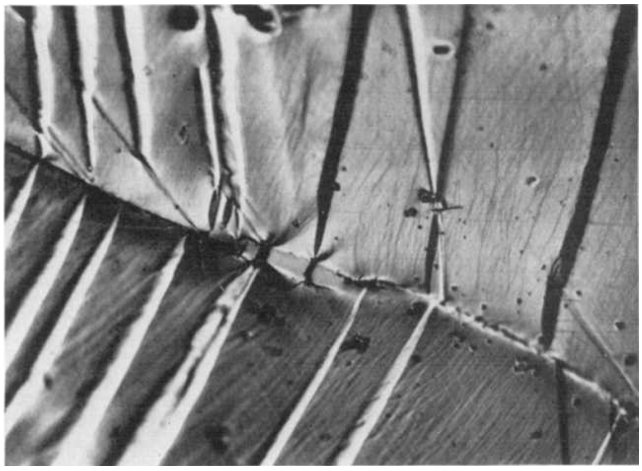

**Figure 18. (An optical image of a grain-boundary particle fractured at twin/grain-boundary intersections. This image was taken from reference [6].**

For materials that deform by slip, it has historically been assumed that dislocation pile-ups enable particle fracture and decohesion, *e.g.* see the work of Gell *et al.* [112], Barnby [114], and Ashby [115]. However, over the last three decades, the work of Hansen [16, 76, 116, 117], Kuhlmann-Wilsdorf [102, 106, 107, 108], and others [117, 118] has demonstrated that dislocation pile-ups collapse into dislocation boundaries, *e.g.* cell walls and cell block boundaries, at very small strains ($\varepsilon<1\%$). It is now generally agreed that these boundaries, rather than dislocation pile-ups, are the primary dislocation structure in cold-worked metals. For reference, both cell blocks and dislocation cell walls are illustrated

in the TEM micrograph provided in Figure 19. These structures are only visible using TEM, electron channeling contrast (ECC) imaging, or EBSD, and were thus not observed in many early studies. More information on the dislocation structures produced by cold working can be found in references [76, 102, 104], with particular attention to the debate between dislocation pile-ups and dislocation boundaries found in reference [111].

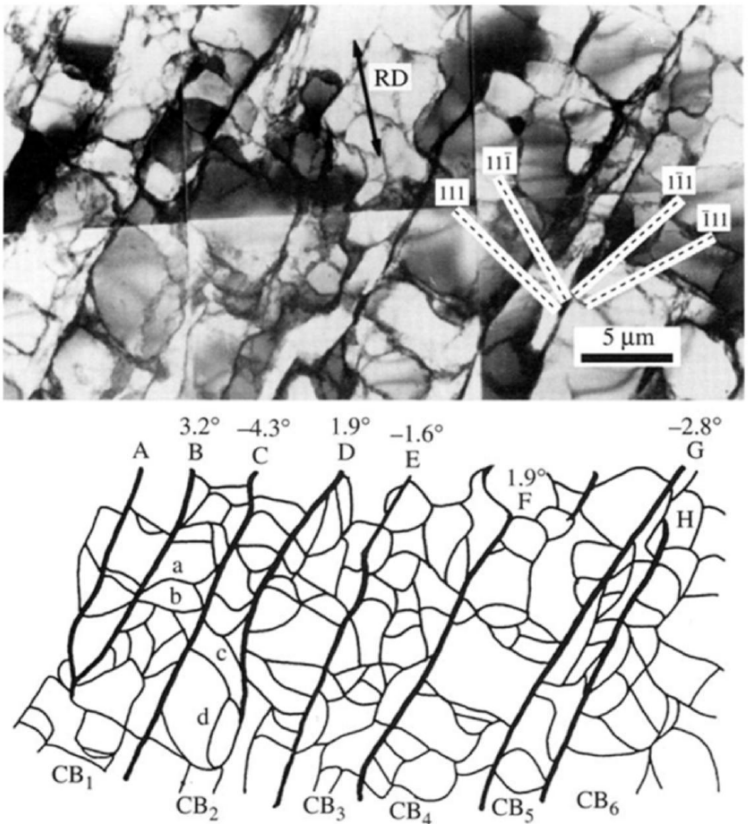


**Figure 19. (a) A TEM micrograph and (b) a sketch of the microstructure in specimen of high-purity Al reduced 10% by cold-rolling are shown. Cell block boundaries ($CB_x$) are colored black in the sketch, while cell walls are colored light gray. The rolling direction (RD) is indicated in the micrograph. Similar microstructures are created by plastic deformation in other bulk metals that deform by slip. This image was taken from reference [16].**

Based on this understanding of the dislocation structures created by cold work, it is hypothesized that dislocation boundary/particle intersections strongly influence both particle fracture and delamination. This hypothesis is supported by recent studies of particle-stimulated void nucleation enabled by EBSD. Kacher and coworkers characterized the dislocation structures around fractured Fe intermetallics in Al6061 using high-resolution EBSD and observed high densities of dislocation boundaries near the interface of cracked particles [119]. In interstitial-free steels containing TiN

precipitates, Kestens and coworkers [120] observed that particle delamination occurs at approximately the same macroscale strains (15-25%) as the transition from low-angle to high-angle cell block boundaries. EBSD data from this study suggests that particle delamination generally began at or near the intersection between particles and dislocation boundaries, though more detailed analysis is necessary to better establish this interpretation.

#### 2.3.1.2. Theories and models of particle-stimulated void nucleation

Classical theories of void nucleation at particles, either by particle fracture or interfacial debonding, focus on strength-limited nucleation, nucleation on the basis of energetic arguments, or both. Energetic approaches typically require that the local strain energy released must be equal to or greater than the fracture toughness, which is bounded by the surface energy of the two free surfaces [121]. Goods and Brown [46, 122] argued that the energetic criterion was a necessary but not sufficient condition; an additional cohesive strength criterion must be met. Indeed, this interfacial strength criterion may control in purely elastic circumstances because the strain energies associated with meeting the strength criterion are likely more than sufficient to account for the free surface generation [122].

More recently, cohesive zone models have been employed to study both particle decohesion and cracking and understand the relative roles of strength and toughness [123]. Cohesive zone models use special finite elements to model fracture, and hence are based on continuum theory. Needleman [124] was the first researcher to use cohesive zone elements to study the delamination between a two-dimensional particle and the surrounding matrix at the continuum scale with finite elements. Considering a rigid inclusion in an elastic-plastic matrix, Needleman found that the strain at which the particle delaminated—the "nucleation strain"—was sensitive to stress state, particle size, and interface properties. Numerous other researchers have applied the cohesive zone approach to the problem of particle delamination and fracture considering the behavior with various material constitutive relations, particle shapes, and particle arrangements in two- and three-dimensions [125, 126, 127, 128, 129] [130] [14]. The most advanced approaches enable simultaneous modeling of decohesion and cracking *via* dynamic finite element insertion; an example is shown in Figure 20(a) [14].

However, a key difficulty with such continuum approaches is that they ignore the highly heterogenous nature of plastic deformation. In particular, because particles are small, they interact with relatively few deformation-induced defects (e.g., dislocations, twins), making the continuum assumption suspect [131].Capturing these discrete defect interactions is likely important to understanding the decohesion process. This was shown to be true in a recent molecular dynamics study of silicon particle decohesion in copper, where dislocation emission and slip were associated with the debonding process as shown in Figure 20(b) [18]. Interestingly, many of the earliest theories of particle decohesion considered the role of dislocation interactions, but primarily focusing on the stress concentrations generated by dislocation pile ups [3, 132] rather than the active interplay between slip and decohesion observed in modern MD simulations.

*Ab initio* techniques have also been applied to the particle decohesion problem. In particular, interfacial strengths and works of separation [133, 134] have been computed for a variety of interface types. Often the interfacial strengths from these calculations exceed 10 GPa—far larger than the ultimate strength of structural metals. How to incorporate these fundamental atomistic properties into higher length scale models for particle decohesion is unclear.

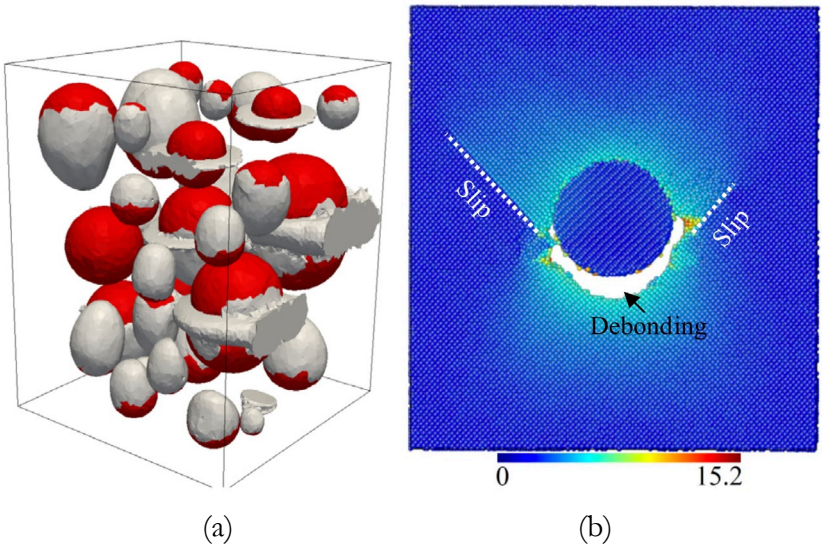


**Figure 20.(a)Three-dimensional finite element simulation of particle cracking and delamination in a metal matrix composite. Bonded particle interfaces are shown in red, free surfaces are shown in gray. Figure is from reference [14]. (b)A snapshot from reference [18] of MD simulations of Si particle debonding from a Cu matrix showing atomic displacements relative to initial configuration. Slip traces from dislocation**

### 2.3.1.3. Discussion

Modern characterization tools have provided new insights into the local microstructural state that triggers void nucleation at second-phase particles and inclusions. It has long been assumed that particle fracture and delamination is enabled by local plastic deformation at the particle/matrix interface, but the deformation microstructures related to void nucleation remain murky. Observations that specific twin types are associated with particle fracture suggest that particle-stimulated void nucleation is highly sensitive to the local defect state. Similarly, in metals that deform by slip, we speculate that specific dislocation boundary configurations enable both particle fracture and debonding, though much more work is necessary to validate this hypothesis. By combining a microstructural understanding of particle-stimulated void nucleation with classic mechanical analyses, longstanding questions in this field on the effects of particle size and stress state on void nucleation may be uncovered.

Since defect interactions plays such a critical role during nucleation at second-phase particles, any modeling technique must accurately capture the physics of these interactions. In contrast, the physical models that have been used to describe crack nucleation and growth in the past are usually approximate and simplistic. For example, the influence of local lattice defects such as dislocations is not considered. In order for micromechanical models of ductile rupture to become predictive, additional work is necessary to develop realistic fracture criteria and compute necessary fracture properties from lower scale simulations. Molecular dynamics is currently the best tool for elucidating the detailed micromechanics of nucleation but suffers from severe time-scale and length-scale limitations. Furthermore, the use of MD in such studies requires interatomic potentials that accurately resolve the properties of defects in both the primary and secondary phases, *and* the properties of the

particle interface. Even still, there are many opportunities to use existing atomistic computational techniques in order to advance our understanding of defect-mediated void nucleation at second-phase particles. This includes studies showing how slip and deformation twinning affect nucleation. Even with these details sorted out, however, relating this information to models of ductile rupture at higher length scales still remains challenging. Future modeling efforts need to focus on elucidating key defect interactions, developing physics-based models that describe the key features of these interactions, and then developing methods for upscaling this information to finite-element-type simulations which can simulate realistic particle microstructures under complex loadings.

### *2.3.2. Void Nucleation at Grain Boundaries*

Grain boundary delamination is commonly observed during ductile rupture of materials with limited plasticity, *e.g.* in many hexagonal close packed (HCP) metals and BCC metals below their ductile-to-brittle transition temperature [8, 12, 135, 136, 137, 138, 139]. This proposed mechanism is similar to particle/matrix decohesion, with one significant difference: while the particle is often fully elastic, the grains on either side of a boundary have (at least some) plasticity. As discussed in this section, grain boundary plasticity and the accumulation of dislocations on either side of the interface play a determinative role in grain boundary decohesion. These roles are often overlooked, though, and unrealistic mechanisms of grain boundary delamination that only consider the local stress state [3, 140] or dislocation density at a grain boundary [73] are still invoked in many contexts [94, 141, 142].

This section presents experimental observations of grain-boundary delamination, discusses the deficiencies of early models of grain-boundary delamination, and presents recent theoretical work in this area. Because void nucleation by grain boundary cleavage does not fundamentally depend on the deformation mechanism (slip *versus* twinning), both of these cases are treated in this section. The case of brittle failure by grain boundary cleavage, which may occur when hydrogen, solutes, or liquid metal segregates to the boundary [143], is outside the scope of the present review.

#### 2.3.2.1. Experimental observations of grain-boundary cleavage

In both pure and particle-containing metals that deform by twinning, voids are sometimes observed at grain boundary/twin intersections or twin/twin intersections. Ng *et al.* and Bieler *et al.* [12, 136] demonstrated that voids in TiAl primarily nucleate at grain-boundary/twin intersections. An example of this is provided in Figure 21. Bieler *et al.* [8] also observed that voids in high-purity α-Ti (HCP) nucleate at the intersection between $T_1$ (primary) and $T_2$ (secondary) twins, as shown in Figure 22. At low, *i.e.* cryogenic, temperatures, void nucleation in some materials occurs more readily at grain-boundary/twin intersections than at second-phase particles [144, 145]. This has been observed in the α-titanium alloy Ti-5Al-2.5Sn [145] and in nitrogen-alloyed austenitic stainless steels [139, 144]. There is also evidence that voids in magnesium alloys nucleate at grain boundary/twin intersections by boundary cleavage, though more study is needed to confirm this conclusion [146, 147, 148].

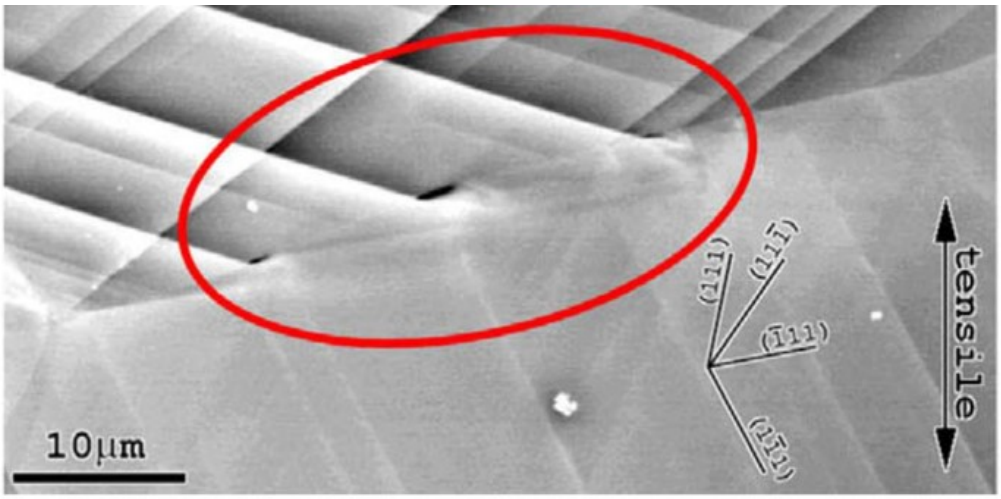


**Figure 21. An electron channeling contrast image of three incipient voids at twin/grain-boundary intersections in TiAl is shown. This image is from reference [12].**

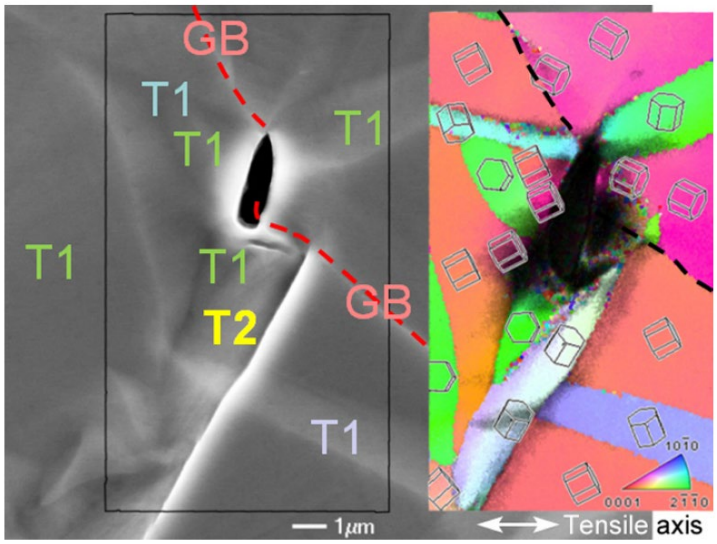


**Figure 22. An image of an incipient void at the intersection of a $T_1$ twin, a $T_2$ twin, and a grain boundary in α-Ti is shown. This image is from reference [8].**

The importance of grain boundaries to ductile fracture in BCC metals is apparent from testing single crystals, which often show tremendous ductility well below the ductile-to-brittle transition temperature of polycrystalline materials [142, 149, 150, 151]. Because of this, it has long been assumed that void

nucleation in polycrystalline BCC metals begins at grain boundaries that act as barriers to dislocation transmission, such as that shown in Figure 23 [142, 152]. However, *in-situ* experiments and atomistic simulations have demonstrated that crystal defects in the grain boundary and adjacent grains can interact in non-trivial ways and promote void nucleation. Wronski *et al.* [5] observed void nucleation *in-situ* in tungsten thin-films fractured in a TEM. Instead of dislocation pileups, arrays of edge dislocations formed on the {110} and {112} planes near grain boundaries. Voids subsequently nucleated a few microns away from grain boundaries only within the arrays of edge dislocation that formed on the {110} plane. Void nucleation by boundary cleavage was also investigated in a recent atomistic study of a planar Σ9 grain boundary in tungsten [153]. It was observed that under some biaxial stress states, a void nucleated at grain boundary dislocations. In other cases, though, lattice dislocations nucleated at the grain boundary and subsequently acted as a nucleation site for voids. These studies suggest that the defect content and atomistic structure of the grain boundary play critical roles in the propensity for void nucleation.

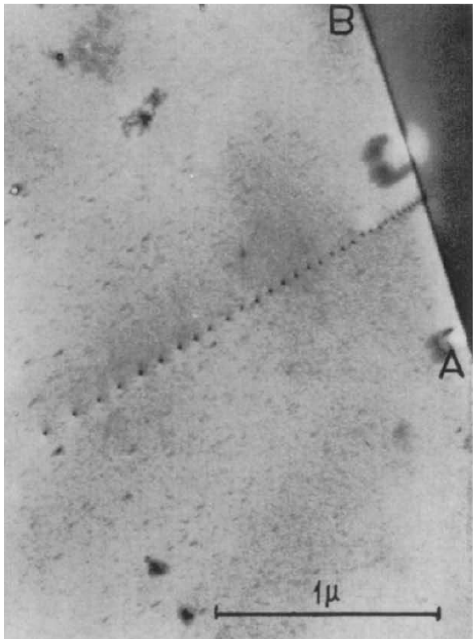


**Figure 23. A TEM micrograph of edge dislocations in a pile-up configuration in BCC tungsten is shown. Such grain-boundary pileups are not observed to nucleate cracks. This image is from reference [5].**

#### 2.3.2.2. Theories and models of grain-boundary cleavage

Early investigators proposed that void nucleation was likely associated with heterogeneities in plastic deformation, particularly dislocation pile-ups at the head of blocked slip bands [3, 132, 140]. It was hypothesized that, if a slip band is blocked by a grain boundary, the tensile stress at the head of the slip band could exceed the cohesive strength of the material and nucleate a void [3]. A schematic of this is shown in Figure 24. This mechanism of void nucleation is now known as the Zener-Stroh mechanism [141]. Zener predicted that the void would nucleate on a plane normal to the active slip

plane within the grain in which the dislocation pile-up formed [3], while others predicted that it would happen in the adjacent grain or within a polygonised array of dislocations [56].

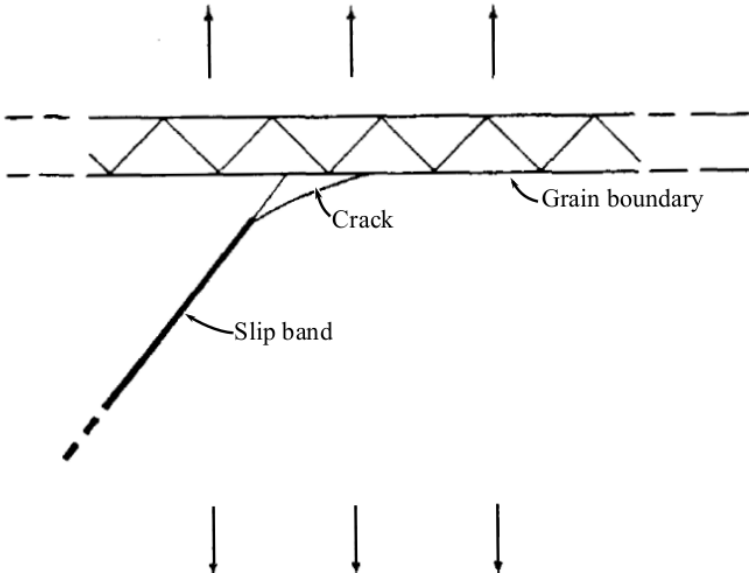


**Figure 24. The Zener-Stroh mechanism of crack nucleation at a blocked slip band is illustrated. This image was modified from reference [3]. There is little experimental evidence that this mechanism occurs during quasistatic, room-temperature deformation.**

Both energy-based and strength-based failure criteria have been invoked with the Zener-Stroh mechanism. For example, Stroh [132, 140] computed the elastic strain energy in the tensile stress region below a pile-up and assumed fracture would occur when this energy exceeded the energy of the new free surfaces of the crack. Combining his result with analysis by Eshelby *et al.* [154]on the geometry of dislocation pile-ups, Low [64] determined that the critical number of dislocations in a pile-up, $n$, for the energy-based theory was

$$n = \frac{3\pi^2\gamma}{8b\tau_a} \qquad 1$$

where $\gamma$ is the surface energy, $b$ is the magnitude of the Burgers vector, and $\tau_a$ is the applied shear stress. For common values of fracture stress and surface energy, this equation predicts that the pile-up must contain $10^2$ to $10^3$ dislocations for voids to nucleate in this manner [132, 140]. From the strength-based perspective, using Koehler's [155] expression for the maximum tensile stress ahead of a dislocation pile-up, the critical number of dislocations is

$$\boldsymbol{n = \frac{\sigma_{tensile}}{\alpha\tau_a}}$$

where $\alpha$ is a constant on the order of unity. Assuming $\sigma_{tensile}\sim 10$ GPa and $\tau_a\sim 100$ MPa, we obtain $n\sim 10^2$ dislocations, similar to the energy-based theory. While the Zener-Stroh mechanism is appealing in many ways, it has been dismissed by many researchers over the years on the grounds that:

- shear stresses on the order of the theoretical shear strength are necessary to form the pile-up

[64],

- the large dislocation pile-ups invoked by these models do not generally form during plastic deformation [111], and
- large local stresses at the head of the pile-up are likely to be dispersed by secondary slip [156].

More recent studies have demonstrated that two interrelated factors determine if voids will nucleate by grain-boundary cleavage [139, 157]:

1) Does the geometric relationship between the active slip/twinning systems on either side of the boundary allow for easy slip transfer?
2) If not, can the local stress/strain at the boundary be relaxed either by existing dislocations or by the nucleation of new dislocations?

Depending on the orientation of the grains on either side of the boundary and the activated slip system(s), a continuum of slip transfer cases may occur. At the extremes, the boundary can either be impenetrable, with no shear transfer across it, or nearly transparent to dislocations, with near perfect transmission from one side to another. For most boundaries, though, slip in one grain is transferred imperfectly into the next and some residual boundary dislocations are left behind. In these cases, the shape change at the boundary must be accommodated by local slip in the neighboring grain.

Kumar *et al.* [135] determined that void nucleation at twin/grain-boundary intersections in TiAl is facilitated by residual dislocation content within the boundary. Based on their analysis, a fracture initiation parameter, $F_1$, was proposed as

$$F_1 = m_{twin}|\boldsymbol{b}_{twin} \cdot \boldsymbol{t}| \sum_{other} \boldsymbol{b}_{twin} \cdot \boldsymbol{b}_{other} . \quad (2)$$

The geometric considerations associated with this parameter are illustrated in Figure 25 and the reasoning behind it is as follows. The Schmid factor of the operating slip (or twin) system, $m_{twin}$, drives a slip band (or twin) into the GB, which then "opens up" the GB by an amount that is proportional to $\boldsymbol{b}_{twin}$. The local tensile $\boldsymbol{t}$ then acts to open the interface further by an amount proportional to $|\boldsymbol{b}_{twin} \cdot \boldsymbol{t}|$. However, this opening can be counteracted or relaxed by slip in the opposing grain, as long as the slip systems in that grain are aligned appropriately; the potential for such relaxation is proportional to $\sum_{other} \boldsymbol{b}_{twin} \cdot \boldsymbol{b}_{other}$, where $\boldsymbol{b}_{other}$ are the Burgers vectors in the opposing grain. As noted by Bieler *et al.* [8], this parameter is maximized when multiple slip systems in the neighboring grain accommodate the twin shear, leading to a higher residual dislocation content. This factor accounted for void nucleation events at twin/grain-boundary intersections in TiAl, though it has not yet been applied to other systems.

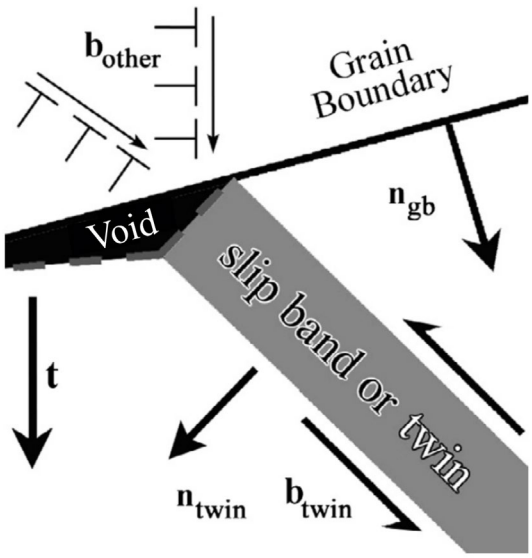


**Figure 25. The relationship between stress state, geometry, and the slip and twinning systems across a grain boundary are illustrated. This schematic is from reference [8].**

One interesting point is that the grain boundary normal $\boldsymbol{n_{gb}}$ does not appear in Eq. (6) because including it did not improve the parameter's ability to predict failure [12]. This is in contrast to the failure parameter proposed by Zhang et al. [4], who studied void nucleation at twin-GB intersections in polycrystalline BCC Mo with molecular dynamics simulations. Figure 26 shows an example from this study. The authors proposed that the propensity for void nucleation at the grain boundary is proportional to the GB displacement induced by the twin-GB intersection,

$$\Delta = t\left(\boldsymbol{b_{twin}} \cdot \boldsymbol{n_{gb}}\right),$$

where the details of the geometry are shown in Figure 26(a). As this displacement increases, so too does the local tensile stress at the grain boundary, as shown in Figure 26(c-d). This implies that thicker twins promote void nucleation.

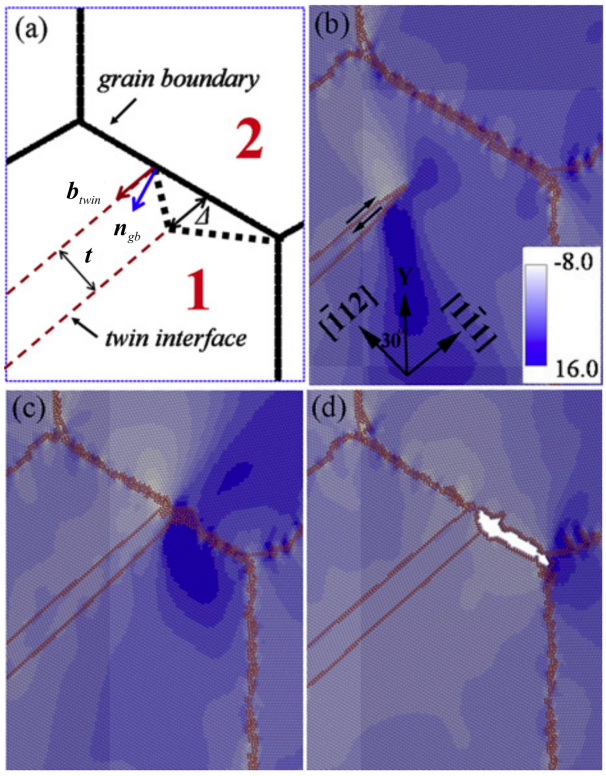


**Figure 26 (a) A schematic of the void nucleation mechanism proposed by Zhang et al. [4] is shown. (b-d) The distribution of tensile stress in the Y direction at strains of (b) 3.3%, (c) 3.4%, and (d) 3.7% are shown. Twin growth is apparent in (b), the twin collides with the GB in (c) and the nucleated void is shown in (d). This figure is adapted from reference [4].**

Müllner [144] has also analyzed the possibility of crack/void nucleation at deformation band-boundary intersections, focusing on twin-twin intersections. He argued that the head of a secondary deformation twin could be treated as a dislocation wall (or, equivalently, a disclination dipole), and that the tensile stress/strain field below the wall would nucleate a crack in the primary twin. This nucleation would be suppressed if dislocations, which were either already present or nucleated by the local stresses, could relax the stress/strain field. From this viewpoint, thinner twins, which provide less volume for dislocations to nucleate within, and lower dislocation densities would promote void nucleation, because dislocation-mediated relaxation would be more difficult. Hence, Müllner argued his theory explained why austenitic steels become brittle at low temperatures [138, 139, 144] where deformation twinning is the dominant deformation mechanism. This behavior is also observed in Ti alloys [145, 158]. Note that Müllner's theory predicts that thinner twins promote void nucleation, whereas the other two theories above predict that thicker twins promote nucleation. It is important, however, to also recognize that Müllner was focused on twin-twin intersections, not twin-GB intersections.

#### 2.3.2.3. Discussion

In materials with limited plasticity, *e.g.* HCP metals, void nucleation is often associated with twins and/or slip bands blocked by a grain boundary. Although this grain-boundary-cleavage mechanism appears similar to particle delamination, the mechanisms that govern it are complicated by the fact that material on both sides of the boundary plastically deforms. Early researchers overlooked this complexity and simply hypothesized that voids form to release the stress or strain energy created by dislocation pile-ups and twins. As discussed in this section, models that only consider the stress state or dislocation density do not accurately describe grain-boundary cleavage.

In general, local defect content and grain boundary structure play critical roles in grain-boundary cleavage, but the effects of seemingly simple parameters such as twin thickness and stress state are still unclear. For example, Kumar *et al.* [135] predicted no dependence on twin thickness, Mullner [144] predicted that thinner twins promote void nucleation, and Zhang *et al.* [4] predicted that thicker twins promote void nucleation. All three of these models invoke, more-or-less, the same mechanism for nucleation: a twin intersection introduces a stress/strain normal to the boundary, which will lead to void nucleation if that stress/strain is not relaxed in some way (e.g., dislocation motion). While this viewpoint is similar to the classical Zener-Stroh model, the focus is on twin-GB intersections rather than slip band-GB intersections. This is an important distinction because twins are intrinsically localized defects, whereas slip often occurs in a diffuse manner. That is why these theories have been successful whereas the Zener-Stroh model has been largely dismissed. Furthermore, none of these models truly identify a critical condition for nucleation, they simply provide a scaling analysis. For example, the debate harkening back to Zener-Stroh over the relative importance of energetic vs. strength considerations remains unresolved by these more modern theories.

We note that many materials do not experience deformation twinning; additional work is necessary to determine the conditions that promote void nucleation at grain boundaries in materials where dislocation-mediated plasticity dominates. Surprisingly few studies have examined grain-boundary cleavage during quasistatic loading in materials that deform by slip. Hence, even though grain-boundary cleavage was one of the first void-nucleation mechanisms proposed, much additional research is still necessary to elucidate this mechanism.

### *2.3.3. Void nucleation at deformation-induced dislocation boundaries*

Although the earliest theories of void nucleation proposed that dislocation arrays played a key role, intragranular void nucleation in particle-free metals that deform by slip remains the most poorly understood mechanism of void nucleation. Indeed, it was only recently determined that voids in ductile metals that deform by slip do not nucleate at grain boundaries. Instead, voids primarily form at the low-energy dislocation structures (LEDS) [76, 106, 107, 108, 159], *e.g.,* dislocation cells and cell block boundaries, created by plastic deformation. Observations of void nucleation at deformation-induced boundaries are presented in Section 4.1. The mechanisms proposed to explain these observations are presented in Section 4.2.

#### 2.3.3.1. Experimental observations of void nucleation at dislocation boundaries

Both *in-situ* and *ex-situ* observations demonstrate that dislocation boundaries act as void nucleation sites in pure, single-crystalline metals. Wilsdorf and coworkers observed void nucleation *in-situ* at dislocation boundaries in single-crystalline thin films of Be deformed using TEM [13, 160]. An example from this work is provided in Figure 27. *Ex-situ* TEM analysis of fractured α-Fe and Ag single crystals also showed that voids nucleate at regular intervals in the most heavily deformed areas of the crystal [161, 162, 163], suggesting that deformation before fracture created void nucleation sites.

Studies of failure in Fe single crystals by Furukimi *et al.* [164] demonstrated that the formation of dislocation boundaries is critical to void nucleation. Specimens with cross-sectional areas of 16 $\mu m^2$ and 28 $\mu m^2$ were elongated to failure, with the small specimen failing by catastrophic shear [165] and the large specimen by void nucleation, growth, and coalescence. Based on EBSD data, it appeared that dislocation boundaries only formed in the larger of the two specimens, perhaps because multiple slip systems were only activated in this specimen. Voids were observed with TEM at dislocation boundaries in the larger sample.

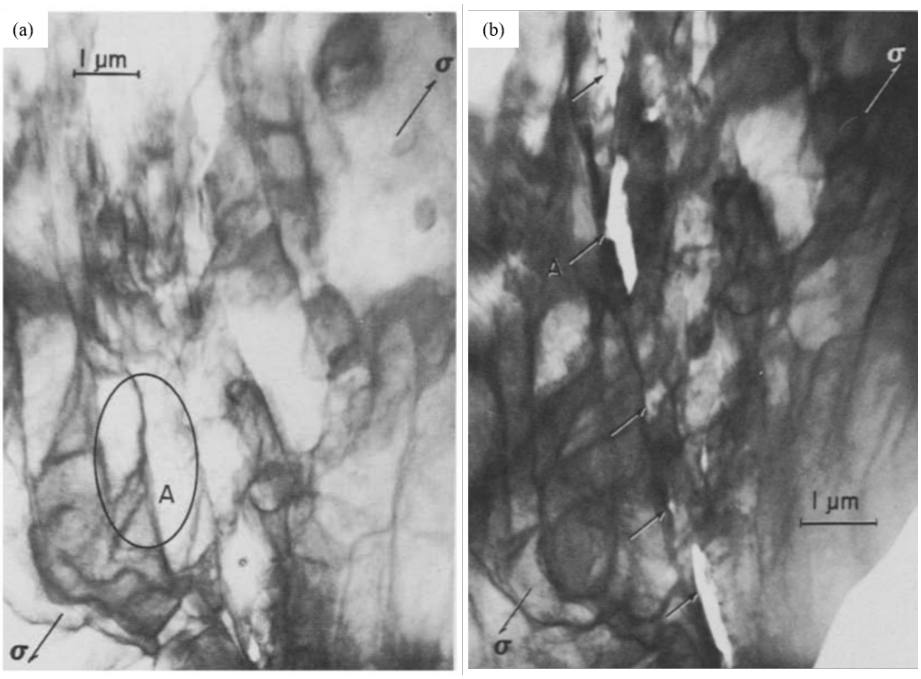


**Figure 27. TEM micrographs of (a) a strained Be single crystal before and (b) after void nucleation. These images show that voids in this material nucleated at deformation-induced dislocation boundaries, likely cell block boundaries. These images are from reference [13].**

For the case of bulk, polycrystalline metals, *i.e.,* materials with grain boundaries, Noell *et al.* [166] demonstrated that dislocation boundaries are still the primary void nucleation site. Incipient voids in high-purity Ta (a BCC metal) were observed at dislocation boundaries, particularly cell block boundaries. An example of this is provided in Figure 28. No voids were observed at grain boundaries in this study. Using EBSD and transmission Kikuchi diffraction (TKD) data, Noell *et al.* analyzed the misorientation angle across the cell block boundaries associated with void nucleation and determined that incipient voids were not always associated with a large misorientation angle. In addition, they also observed a few voids that nucleated at low-angle dislocation cell walls. These results suggest that a simple metric such as misorientation angle across a dislocation boundary is not predictive of void nucleation. Recent observations of void nucleation at dislocation boundaries in Al (an FCC metal) indicate that dislocation boundaries are the primary void nucleation site in particle-free metals that deform by slip, regardless of crystal structure [167].

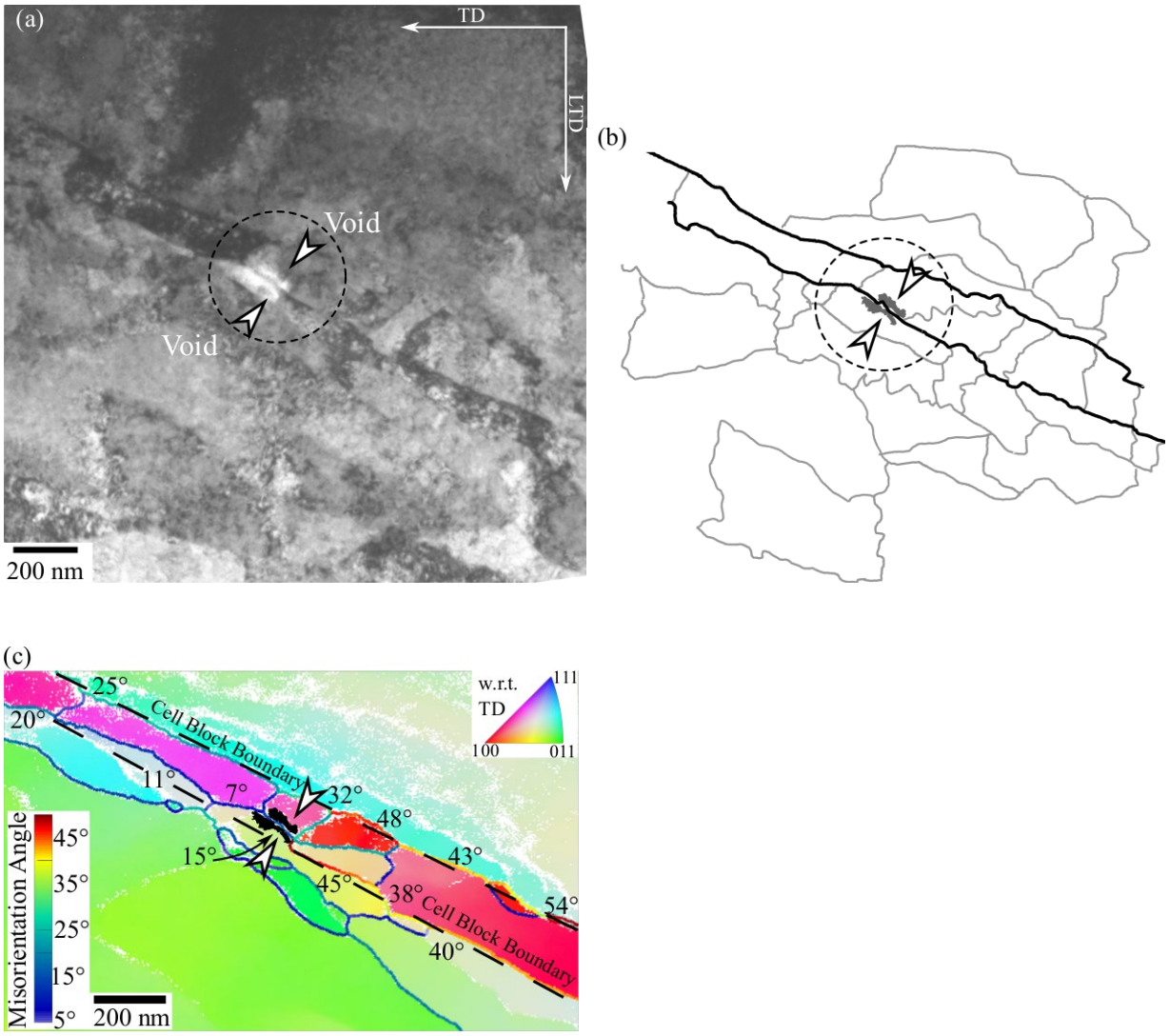


**Figure 28. A TEM micrograph of incipient voids that nucleated at a cell block boundary in a deformed, high-purity Ta material are shown in (a). A sketch highlighting the dislocation structures around these voids, with cell block boundaries colored black and cell walls colored gray, is shown in (b). Transmission kikuchi diffraction (TKD) data from the microstructure around the voids shown in (a) are presented in (c) as an IPF map colored with respect to the TD. The misorientation angle across each segment of the boundary is shown in (c). The misorientation across the portion of the cell block boundary at which voids nucleated was significantly less than that across many nearby boundaries.**

### 2.3.3.2. Theories of void nucleation at dislocation boundaries

Three mechanisms have been proposed for void nucleation at dislocation boundaries:

- nucleation via "cavity dislocation" formation

- the strain energy associated with the misorientation across the boundary drives the formation of voids as a mechanism to relieve strain energy (similar to boundary decohesion), and
- vacancy condensation within the boundary produces voids.

These three theories and experimental evidence for them are now discussed in more detail.

In 1958, Cottrell hypothesized that voids could form at slip-band intersections by dislocation combination [73]. The key concept is that certain dislocations can act as "cavity dislocations," meaning the voids can nucleate from the core of the dislocation. The prime example Cottrell considered was the reaction of two $\langle 111 \rangle$ dislocations in a BCC metal such that

$$\frac{a}{2}[\bar{1}\bar{1}1] + \frac{a}{2}[111] \rightarrow a[001]. \quad 3$$

The resulting dislocation is energetically favorable, and its Burgers vector is parallel to the $\{001\}$ cleavage plane in BCC metals—to quote Cottrell, it is a "cleavage knife." For these reasons, Cottrell proposed that this dislocation would form and nucleate a crack in the solid. While this mechanism is elegant and simple, there is no direct experimental or theoretical evidence that voids can nucleate in this way. Since Cottrell proposed such a mechanism, our understanding of the dislocation core has significantly improved with the advent of modern atomistic simulation tools [168] [169], and no study has revealed nucleation by this mechanism. For example, in recent large-scale MD simulations of plasticity in BCC Ta, many $a\langle 001 \rangle$ junctions formed but no voids or cracks were observed to form over a variety of straining conditions [170].

Wilsdorf and coworkers proposed that voids form as microcracks along dislocation boundaries to relieve the strain energy associated with the misorientation across the boundary [1, 91, 97]; the dislocations in the boundary are attracted towards the free surfaces of the void/microcrack, where they are able to annihilate and release their strain energy. The energy change associated with this process is [81]

$$\boldsymbol{\Delta E = E_{e_2} - E_{e_1} + E_{\gamma_2} + E_f + E_w} \quad 4$$

where $E_{e_1}$ is the strain energy of the boundary before void nucleation, $E_{e_2}$ is the strain energy after dislocation annihilation, $E_{\gamma_2}$ is the surface energy associated with the void's surfaces, $E_f$ is the frictional energy necessary to move the lattice dislocations, and $E_w$ is the work done by the applied stress. According to their hypothesis, void nucleation becomes energetically favorable once the misorientation across the deformation-induced boundary reaches a critical angle, since a higher misorientation means a higher dislocation density and a higher value for $E_{e_1}$ [1, 97]. Wilsdorf cited experimental observations of void nucleation at high-angle dislocation boundaries as evidence for this mechanism, *e.g.* references [13, 160, 161, 162, 163]. This theory is, however, unsupported by later experimental observations. As discussed in the previous section, Noell *et al.* [166] observed no correlation between misorientation angle of a deformation-induced dislocation boundary and the frequency of void formation. Furthermore, this theory does not explain the origin of the void nucleus/microcrack in the dislocation boundary. Rather, it is simply an analysis of whether a nucleus would be stable if it were to form.

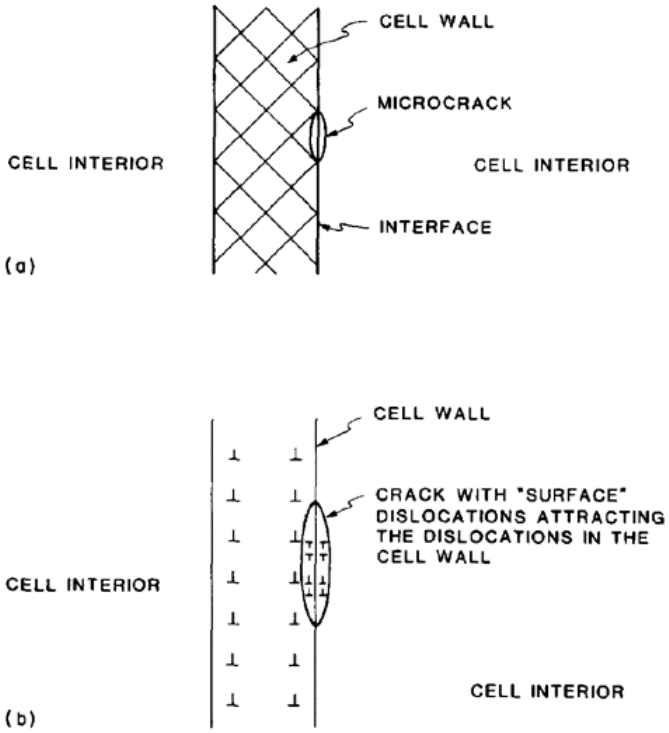


**Figure 29. A schematic illustration showing void nucleation at a dislocation cell wall is shown in (a). A dislocation model of void nucleation at a cell wall is shown in (b) with dislocations at the surface of the void embryo drawn in a smaller size. This figure is from reference [1, 2].**

The third theory, which we believe is most supported by evidence, is void nucleation by vacancy condensation. Void nucleation by vacancy condensation during room-temperature deformation has often been dismissed as theoretically impossible for at least one of the following reasons:

- the concentration of vacancies at room-temperature is far too small for voids to form,
- the room temperature diffusivity of vacancies is too slow for voids to form, and
- vacancy clusters will collapse before a stable void can form.

Most of this section thus presents experimental and theoretical studies that respond to each of these objections and demonstrate the viability of this void-nucleation mechanism.

Vacancies increase the entropy of a crystalline solid, leading to a reduction in its free energy. Hence, vacancies are always present in crystals. Statistical mechanics shows that a crystalline solid has a temperature-dependent equilibrium vacancy concentration given by [171]

$$c_v^{eq} = c_{v0} exp\left(\frac{-\Delta e_f}{k_B T}\right) \quad 5$$

were $k_B$ is Boltzmann's constant, $T$ is the absolute temperature, $\Delta e_f$ is the formation energy of a vacancy, and $c_{v0}$ is a constant in the range of 2 to 10. Here we express the vacancy concentration as the fraction of lattice sites containing vacancies (missing atoms). For typical formation energies of

common metals, equilibrium vacancy concentrations range from less than $10^{-20}$ at room temperature up to approximately $10^{-4}$ near the melting point [171].

These vacancy concentrations apply to a crystal at thermal equilibrium. There is strong experimental evidence that plastic deformation produces a vacancy supersaturation that can be as large as $10^{-3}$ [172, 173, 174]. There are two general theories for how vacancies are produced during plastic deformation. Both theories rely on the fact that vacancies are either produced or consumed (depending on the glide direction) when non-screw dislocations move out of the glide plane containing their line and Burgers vector. This is referred to as climb motion. The first mechanism, worked out in detail by Saada [175, 176, 177], is annihilation of non-screw dislocations of different glide planes. If the elastic interaction between the dislocations is attractive (typically the case if they can annihilate) and they are a short distance apart, the elastic interactions may be strong enough to induce climb motion. According to this model, the concentration of vacancies produced by cold-work is proportional to the work done as

$$c_v = A \cdot \frac{1}{G} \int_0^{\varepsilon} \sigma \, \mathrm{d}\varepsilon \qquad 6$$

where $G$ is the shear modulus, $\sigma$ and $\epsilon$ are the applied stress and strain, and $A$ is a constant on the order of 0.1 [178]. According to this mechanism vacancies are primarily produced in areas of the microstructure with large dislocation densities (*e.g.*, cell walls and boundaries).

The second mechanism involves the formation of Burgers-vector-sized edge dislocation segments on screw dislocations after they intersect and cut through forest dislocations. If the edge line direction vector has a component out of the screw glide plane, the segment is termed a jog and can only move with the gliding screw dislocation by climbing. Cuitino *et al.* [179] proposed that the vacancy concentration will depend on the jog density, $J$, the slip strain rate $\dot{\gamma}$ and the dislocation density $\rho$ as

$$c_V = \frac{b^2}{L} \int \frac{J\dot{\gamma}}{\rho} \mathrm{d}t \qquad 7$$

where $b$ is the Burgers vector and $L$ is the mean-free path for the generation of a vacancy by a moving jog. Vacancy production by this mechanism is thought to occur homogenously throughout the material. Several large scale atomistic studies have revealed this "jog dragging" mechanism for vacancy production [180, 181].

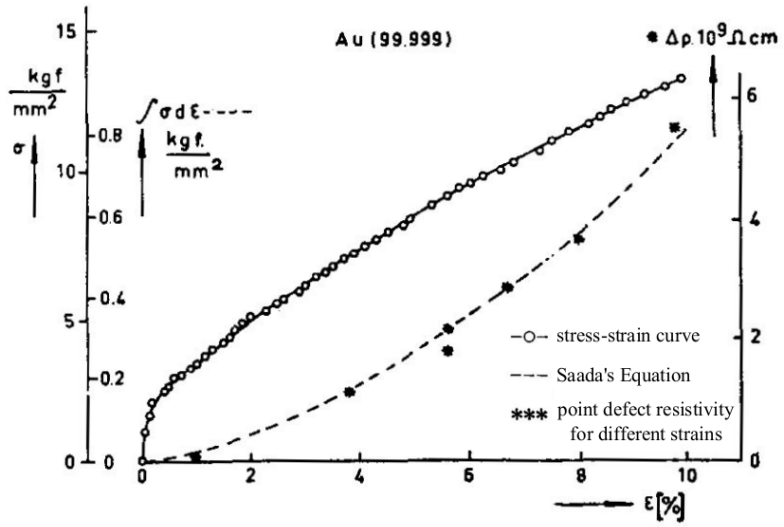


**Figure 30. Stress versus strain data from Au and the total point defect resistivity for different strains are plotted. Point defect resistivity generally increases with increasing vacancy concentration. This figure was modified from reference [7].**

Validating these proposed vacancy production relationships experimentally is a significant challenge. Using currently available techniques for measuring vacancy concentration in bulk samples, such as electric resistivity, X-ray spectroscopy, and positron annihilation spectroscopy, it is difficult to differentiate between dislocations and vacancies. For example, assumptions that are difficult to validate must be made about the trapping rate and lifetime of positrons at dislocation lines and vacancies [182]. With these caveats in mind, we now briefly present a few reports on the measured relationship between strain and vacancy concentration. The theory of Saada generally compares well with experimental data of vacancy-induced resistivity changes at low strains ($\epsilon$<10%), as shown in Figure 30 [7, 174]. Good agreement has also been found between the jog model and experimental results [172, 179], though much less attention has been devoted to validating this model. Positron annihilation spectroscopy and X-ray spectroscopy measurements of deformed samples both indicate that there is an upper limit for the deformation-induced vacancy concentration of $\sim 10^{-4}$ at atmospheric pressure, which may be reached at strains of ~100% [178]. *In-situ* X-ray spectroscopy measurements suggest that the grain boundary vacancy concentration is orders of magnitude larger than that of the matrix, as shown in Figure 31. Lastly, recent positron annihilation measurements of vacancy clusters in severely plastically deformed materials indicate that vacancies cluster during plastic deformation and that the size of these clusters depends on the material [183]. One of these datasets is presented in Figure 32.

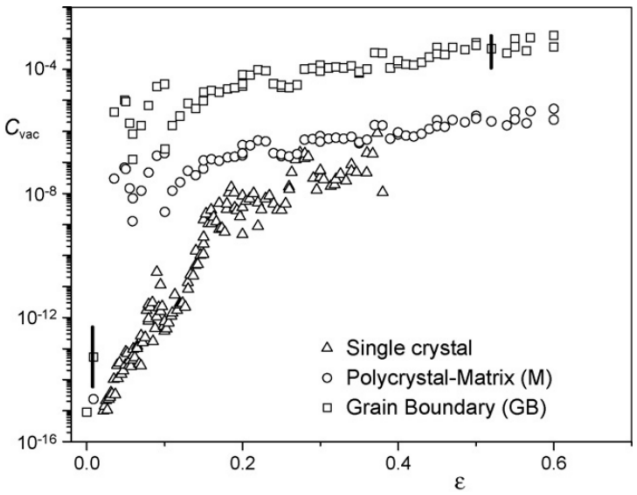


**Figure 31. The vacancy concentration produced in copper samples during compression is shown as a function of strain. Vertical lines indicate uncertainty in the data. at 2.7% strain are shown.**

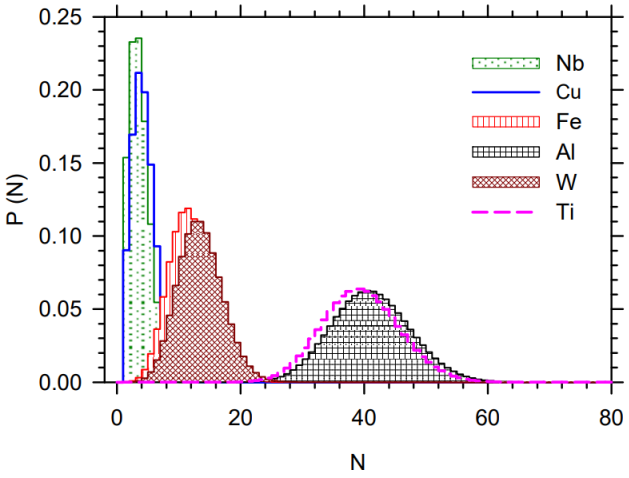


**Figure 32. The size distribution P(N) of vacancy clusters in six different severely plastically deformed samples is plotted as a function of cluster size.**

For vacancies to promote void nucleation at dislocation boundaries, they must either be present locally in appreciable concentrations or sufficiently mobile to migrate to the boundaries. This may occur in one of two ways: either vacancy production is highly heterogenous, with most vacancies produced at or near dislocation boundaries, or vacancies must be mobile enough to diffuse to void nuclei at dislocation boundaries. According to the theory developed by Saada [175, 176, 177], vacancy production *via* dislocation annihilation will occur primarily in regions with a locally high dislocation

density such as dislocation cell walls and cell block boundaries. The local vacancy concentration at these features may then be sufficient to create a large vacancy cluster. If vacancies are instead primarily produced by the glide of jogged screw dislocations, vacancy production is predicted to be relatively homogeneous. Significant diffusion may then be necessary for the vacancies to form a void embryo. Although long-range vacancy diffusion through the lattice is limited at room temperature, dislocation cores and grain boundaries provide paths for vacancy diffusion that are orders of magnitude faster than lattice diffusion [184]. Numerous atomistic studies have shown that in FCC metals, the activation energy for vacancy pipe diffusion along a dislocation core is between 0.1 and 0.3 eV (depending on the dislocation character angle and position within the core) lower than for bulk diffusion [185, 186].

Once a sufficient vacancy concentration is present in the material, the vacancies must condense together into stable void nuclei. There is a large body of literature on void nucleation in the context of classical nucleation theory, according to which the free energy change associated with formation of a *n* vacancy cluster is [187, 188, 189]

$$\Delta G = -nk_B T \ln(c_v/c_v^{eq}) - n\sigma^H \Omega + E_n \qquad 8$$

where $\sigma^H$ is the hydrostatic stress, $\Omega$ is the atomic volume, and $E_n$ is the formation energy of the cluster. Often the cluster is approximated as a spherical cavity of radius $r$ with isotropic surface energy $\gamma$, giving $E_n = 4\pi r^2 \gamma$. Eq. 8 indicates that the primary driving forces for cluster growth are vacancy supersaturation (expressed as $c_v/c_v^{eq}$) and the work done by hydrostatic stress.

However, it is important to note that as vacancy clusters grow, other types of defects beside voids are able to form, such as stacking fault tetrahedra and dislocation loops. Such defects are often formed in materials with vacancy supersaturations from quenching or irradiation [190, 191, 192, 193, 194, 195, 196, 197, 198, 199] when vacancy clusters collapse after reaching a critical size. In order to determine which defect is most stable for a given cluster size and geometry, a careful energetic analysis is necessary. For example, Gavini et al. [200] and Varvenne et al. [201] studied the energetics of voids and dislocation loops in FCC Al and HCP Zr, respectively, using *ab initio* methods. Both studies found that a 7 vacancy cluster would collapse into a dislocation loop. Note that the specific configuration of the vacancies in the cluster strongly impacts the energetic analysis. Importantly, none of these studies considered the influence of hydrostatic stress on void stability. Figure 33 is a schematic for how hydrostatic stress could influence void stability, showing that tensile hydrostatic stresses will always tend to promote void nucleation over other defects since voids maximize the volume change of the solid. Lastly, we point out that interstitial gases, such as hydrogen and oxygen, are known to promote and stabilize vacancy clusters [188, 202, 203, 204, 205]. In fact, several researchers have theorized that hydrogen-embrittlement is caused by vacancy-trapping at hydrogen leading to the formation of voids at low strains [198, 206, 207].

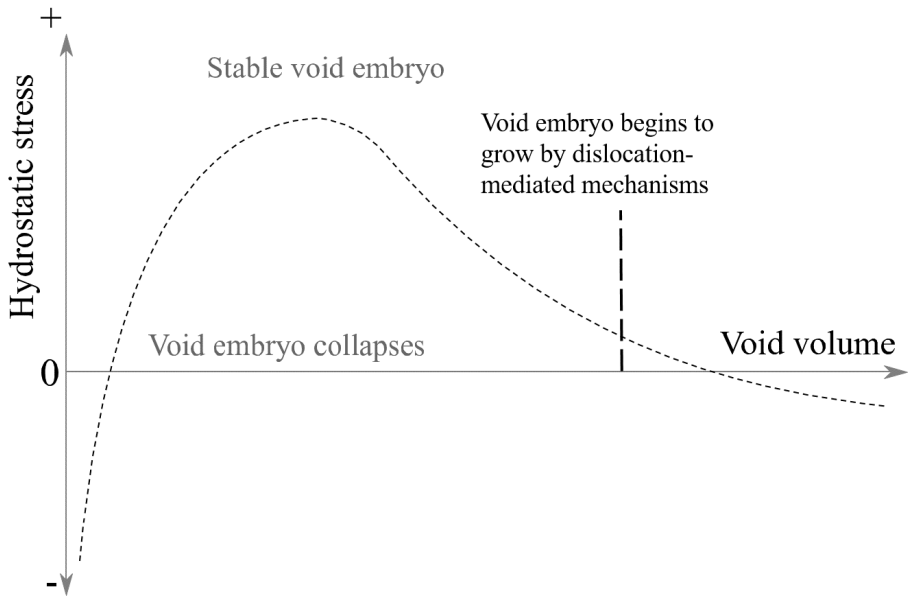


**Figure 33. A qualitative plot of hydrostatic stress *versus* the volume of a vacancy cluster is shown. This plot illustrates the concept that a vacancy cluster will collapse into a compact defect (such as a dislocation loop or a stacking fault tetrahedron) if the applied hydrostatic stress is too low.**

Lastly, for a stable vacancy cluster to contribute to fracture, it must be able to grow at experimental time scales. While the theories above only consider the energetics (thermodynamics) of void nucleation, the kinetics must also be considered. Although vacancy diffusion likely contributes to the formation of the vacancy cluster, such processes are too slow to explain the growth of micron-scale voids during quasistatic deformation near room temperature. Instead, it is generally agreed that void nuclei grow by dislocation-mediated mechanisms [179, 208]. There has been some controversy recently as to what the primary mode of dislocation-mediated growth is. While a number of authors have argued that voids grow by nucleating dislocations from their surface [209, 210, 211], Nguyen and Warner [212] showed that this process was too slow to explain experimentally observed growth rates relevant to quasi-static loading. In Chapter 4, we show that voids are able to grow much more readily in the presence of a high density of dislocations by adsorbing the dislocations [213]. We argue that an adsorption-mediated growth mechanism explains the observation made by Noell *et al.* [71] that voids tend to nucleate in dislocation boundaries, where the dislocation density is very high. From this viewpoint, a high dislocation density is necessary to enable rapid void growth kinetics, while the driving force for growth comes from the local hydrostatic stresses.

The discussion in this section suggests that vacancy clustering is a viable mechanism for void nucleation. Demonstrating this mechanism experimentally is challenging, though, and the role of vacancies during void nucleation has received relatively little attention. Perhaps the best evidence for this mechanism comes from the work of Dyson *et al.* [214], who observed that voids nucleate near grain boundaries in Nimonic 80A after room temperature deformation and subsequent annealing. An example of this is shown in Figure 34. No voids were observed before annealing, suggesting that voids nucleated by vacancy condensation when the vacancy diffusivity was increased. Voids appeared to preferentially form at boundaries where the residual stress produced by plastic deformation likely had

a large hydrostatic component. Other relevant studies in metals processed by severe plastic deformation (SPD) techniques, *e.g.,* equal-channel angular pressing (ECAP) and high-pressure torsion (HPT), revealed that networks of voids can be created in fully dense specimens during SPD. Because SPD techniques, within which tensile stresses are minimized, generally prevent void nucleation by any of the other mechanisms discussed in this article, it is hypothesized that these voids are produced by vacancy agglomeration [215, 216, 217]. This hypothesis is consistent with the observations of Zehetbauer [218] and others that SPD creates vacancy concentrations as large as $\sim 10^{-3}$ [215].

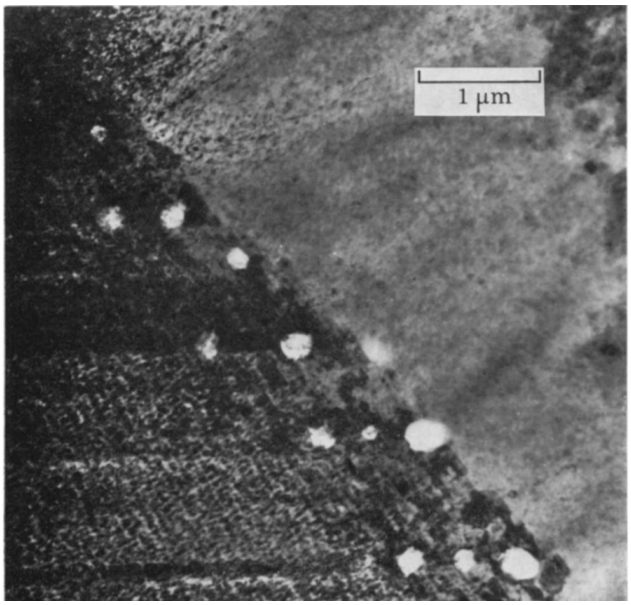


**Figure 34. An image of voids that that nucleated at or near a grain boundary in a Nimonic 80A specimen that was strained at room temperature and subsequently annealed is shown.**

### 2.3.3.3. Discussion

There is now strong experimental evidence that voids in pure, ductile metals nucleate at dislocation boundaries, but these observations have yet to be incorporated into theories of void nucleation. It has been proposed that voids nucleate at these features by vacancy condensation and/or by a cleavage-like mechanism at dislocation cores. While clever, the latter mechanism is unsupported by recent atomistic studies of dislocation-mediated plasticity. Conversely, the limited experimental work on vacancy condensation suggests that it is a viable void-nucleation mechanism during room-temperature deformation. Much work remains to determine if and how vacancies contribute to void nucleation during ductile fracture. A comprehensive computational framework for studying vacancy condensation during ductile rupture would require a thorough understanding of vacancy generation at moving dislocations, subsequent vacancy diffusion in the bulk and along dislocation cores, the dynamics of vacancy clustering, and the final transition to a rapid void growth mechanism, possibly by dislocation adsorption. Assembling such a framework is a daunting multiscale task. Experimentally, more direct examinations of incipient voids and vacancy clusters are necessary to provide further insight into the relevant generation and diffusive mechanisms.

## 2.4. External factors affecting nucleation

While the focus of the present review has been on the conditions of void nucleation under room-temperature, quasi-static loading, it is worthwhile to briefly highlight some of the key differences in void nucleation at elevated strain-rates and under creep conditions at elevated temperatures. At the outset, it is important to note that there is still no consensus on the mechanisms of void nucleation during shock (high-strain-rate deformation) or creep (high-temperature deformation). The goal of this section is thus primarily to highlight the differences between void nucleation under these conditions from those during quasistatic, room-temperature deformation. This section briefly describes the characteristics of void nucleation during shock and creep and discusses some of the proposed mechanisms.

### *2.4.1. The effect of strain rate*

Void nucleation during high-strain-rate deformation is characterized by the following aspects:

- void nucleation occurs at stresses many times larger than during quasistatic deformation [219, 220, 221],
- voids form both at second-phase particles and grain boundaries [220, 221, 222, 223, 224, 225], and
- nucleation occurs in a highly localized area of the microstructure after significantly less plasticity than during quasistatic deformation [220].

The stress a material can withstand before voids nucleate increases dramatically with increasing strain rate. For example, global stresses on the order of 5 GPa are necessary to create voids in high-purity Ta at strain rates of $10^7$ $s^{-1}$ [220]. With increasing stress, grain-boundary cleavage mechanisms such as the Zener-Stroh mechanism become feasible. The limited slip that occurs during shock loading prevents stress relaxation and likely also favors cleavage-like nucleation mechanisms [222]. This may explain why voids in engineering materials nucleate at both grain boundaries and second-phase particles during high-rate deformation [220, 221, 222, 223, 224, 225]. Grain-boundary voids are also observed in pure metals during shock loading, such as that shown in Figure 35 [220]. Recent work has shown that voids in shocked Cu and Ta primarily form on boundaries separating grains with significantly different plastic responses such that large stresses localize at the boundary [220, 225, 226].

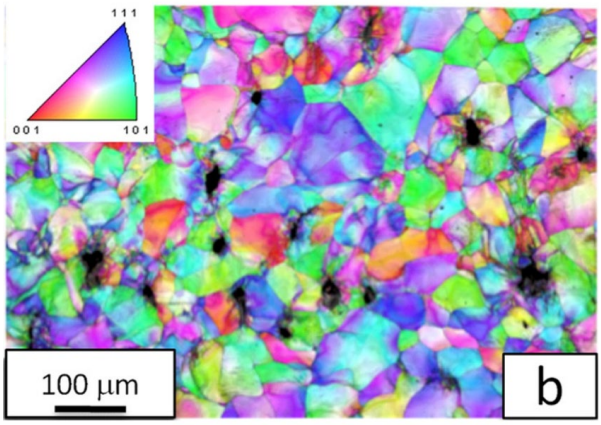


**Figure 35. EBSD data plotted as an inverse pole figure map relative to the loading direction showing the microstructure around voids in spalled Ta are shown. These images show voids that nucleated at grain boundaries.**

In summary, increasing strain rate favors cleavage-like nucleation mechanisms and hinders plasticity-based nucleation mechanisms. Fast strain rates can also produce localized heating (adiabatic shearing) or produce complex stress states, both of which can alter the characteristics of void nucleation. These topics are outside the range of the present review, though, and the reader is directed to the following references for more information [219, 222, 223].

### *2.4.2. The effect of temperature*

The general effects on void nucleation of increasing temperature are:

1. to decrease the stress at which voids nucleate [227, 228],
2. favor particle decohesion over particle cracking [229],
3. favor the formation of voids at particles on grain boundaries transverse to a tensile stress rather than intragranular particles [227, 230, 231, 232, 233], and
4. decrease the critical strain at which voids form such that, at elevated temperatures, voids nucleate continuously throughout testing, with the void density increasing approximately linearly with strain [227, 229, 230, 234].

The underlying reasons for these transitions are an increase in the equilibrium vacancy concentration, the increased diffusivity of atomic vacancies with increasing temperature, and the decreased interfacial strength of boundaries.

The general characteristics of void nucleation at elevated temperature suggest that vacancy condensation plays an important role [235, 236, 237]. Vacancy concentration and mobility is highest at grain boundaries. In addition, continuous void nucleation suggests that void nucleation is controlled by slip and vacancy diffusion rather than stress [229]. However, theoretical calculations indicate that the stress concentrations necessary to drive void nucleation by vacancy condensation are unrealistically large for creep [229]. Because of this, it has been proposed that vacancies act to lower the interfacial energy of the particle/matrix interface, thus enabling void nucleation mechanisms such as interface/interphase decohesion [229]. Others have proposed that blocked slip bands and grain-boundary sliding may produce the necessary stress concentrations for void nucleation [238, 239].

Lastly, it is important to note that several studies have reported that void nucleation may simply depend on grain-boundary sliding, not local vacancy concentration or vacancy diffusivity [238, 239, 240]. For more information on the mechanisms of void nucleation during creep, the reviews of Kassner [231, 238] and Riedel [229] may be consulted.

## 2.5. Summary and conclusions

Classic theoretical models attributed void nucleation to specific crystal defects, such as inclusion interfaces and vacancy agglomerations, and therefore to specific mechanisms. However, it is becoming increasingly clear that nucleation is most likely to result from a combination of many defect-defect interactions instead of a single mechanism. Previous mechanistic interpretations of the ductile rupture process, as shown in Figure 16, thus oversimplify the process. Instead, it is likely that several of these processes work in concert to create the worst-case conditions needed for incipient void nucleation. Indeed, atomistic studies have shown that it is essentially impossible to nucleate a void without nucleating other defects, such as dislocations and vacancies along the way.

We have shown a number of experimental and computational examples where interface-dislocation and interface-twin interactions are important. This observation, that defect interplay controls void nucleation, is important because it means a rigorous understanding of void nucleation necessitates a holistic view of deformation history and deformation mechanisms. For example, just considering the strength of a given interface or the supersaturated vacancy concentration is insufficient. Rather, the overall defect content of the crystal strongly influences the nucleation mechanisms and must be considered as a whole. The recent work by Bieler et al. [12, 157] provides an example of an analysis where multiple defects and deformation processes are considered simultaneously—deformation twins intersect with grain boundaries producing strain fields that can be relaxed by slip. Their work is largely focused on understanding scaling behaviors, however, and is far from producing a predictive, mechanistic theory. None-the-less, their work provides an example of a fruitful direction for future void nucleation studies.

These observations also bring into question the application of continuum models in studying void nucleation. Since voids nucleate at submicron length scales, void nuclei interact with relatively few crystal defects. It is difficult, or impossible, to reproduce the details of these submicron interacts with continuum theories, such as cohesive zone modeling. After all, such theories were originally developed to describe macroscopic fracture events, where quantities such as the fracture toughness and cohesive strength are well-defined.

Instead, atomistic tools are the most likely to yield insight into the process of void nucleation. Surveying the literature, there have been relatively few atomistic works focused on understanding mechanisms of void nucleation, which we have summarized here. More systematic atomistic studies focused on understanding defect-defect interactions are necessary. For example, most of the atomistic works cited here started their simulations with perfect crystals free of dislocations, vacancies, or deformation twins. Studies that examine the influence of realistic, pre-existing defect microstructures are necessary. An example of such a study is the work by Chang et al. [213], who introduced an edge dislocation in their simulation cell to assess the role of dislocation adsorption into a grain boundary on void nucleation.

The study of void nucleation has benefited greatly from modern experimental techniques; namely, EBSD, TKD, X-ray tomography, and focused ion beam milling. Indeed, most of the recent insights reviewed in this paper are a direct result of one or more of these techniques. Surprisingly few studies have applied EBSD and/or TKD to studying the microstructural features associated with particle-

stimulated void nucleation. Future work on the relationship between void nucleation and dislocation structures will likely provide new insights into longstanding questions about the roles of, for example, particle size, particle morphology, and particle spacing. New opportunities at synchrotron sources to directly relate void nucleation to the local crystallographic orientation and stress state [241] will also be critical to understanding void nucleation.

Finally, the fact that void nucleation is sensitive to defect interactions at the submicron scale means that it is likely highly stochastic; defect content varies significantly from grain-to-grain, meaning some grains will be well suited to nucleate voids while others are not. A comprehensive theory of void nucleation must therefore be statistical in nature. Future experimental and computational studies will need to leverage data-science-based approaches to identify trends and key factors affecting nucleation.

# 3. SITES OF VOID NUCLEATION IN PURE DUCTILE METALS

In the absence of pre-existing failure-critical defects, the fracture or tearing process in deformable metals loaded in tension begins with the nucleation of internal cavities or voids in regions of elevated triaxial stress. While ductile rupture processes initiate at inclusions or precipitates in many alloys, nucleation in pure metals is often assumed to be associated with grain boundaries or triple junctions. This study presents ex-situ observations of incipient, subsurface void nucleation in pure tantalum during interrupted uniaxial tensile tests using electron channeling contrast (ECC) imaging, electron backscatter diffraction (EBSD), transmission Kikuchi diffraction (TKD) and transmission electron microscopy (TEM). Instead of forming at grain boundaries, voids initiated at and grew along dislocation cell and cell block boundaries created by plastic deformation. Most of the voids were associated with extended, lamellar deformation-induced boundaries that run along the traces of the {110} or {112}.

planes, though a few voids initiated at low-angle dislocation subgrain boundaries. In general, a high density of deformation-induced boundaries was observed near the voids. TEM and TKD demonstrate that voids initiate at and grow along cell block boundaries. Two mechanisms for void nucleation in pure metals, vacancy condensation and stored energy dissipation, are discussed in light of these results. The observations of the present investigation suggest that voids in pure materials nucleate by vacancy condensation and subsequently grow by consuming dislocations.

## 3.1. Introduction

In the middle of the 20th century, the pioneering work of Tipper [72] and Puttick [2] revealed that ductile fracture is a multi-step process of void nucleation, growth and coalescence. Subsequent modeling and experimental work based on the theories of Rice [31], Gurson [32], Tvergaard [33] and Needleman [84] produced well-validated models for the growth and coalescence of voids during tensile plastic deformation under high-triaxiality conditions, *e.g.* [85] [48, 87, 88], but this is rarely observed experimentally in engineering materials. More sophisticated approaches invoke interphase/interface decohesion and/or particle cracking as the mechanisms of void nucleation [82, 84, 89]. Although this approach is often useful, it is not always applicable to metals with submicron particles [90, 91, 92] [93, 94] [59] and is clearly incorrect for pure, single-phase metals. Because these materials also fail by void coalescence [57, 95, 96, 97], an essential first step to understanding their fracture is determining where and how voids nucleate in the absence of second-phase particles.

During quasistatic loading, voids in pure, low-stacking fault energy and nanocrystalline metals nucleate at grain boundaries, triple junctions or twin intersections [12, 98, 99]. Based on these observations, it is generally assumed that voids in all pure metals initiate at these features [100]. However, the recent work of Boyce *et al.* [101] suggests that the dislocation boundaries created during deformation may also act as important sites for void nucleation. This hypothesis is supported by early investigations of void initiation in pure, single crystalline metals by Wilsdorf and coworkers. These studies, summarized in Wilsdorf's seminal 1983 review [97], established that, in the absence of particles and grain boundaries, void initiation occurs at deformation-induced dislocation boundaries. An example of this is presented Figure 53. Jagannadham *et al.* [81] hypothesized that these voids nucleated to relieve the strain energy associated with the deformation-induced boundary after a critical boundary misorientation was reached. However, the case of void initiation in a pure, bulk polycrystalline material has not been extensively investigated. This study thus examines if deformation-induced boundaries or grain boundaries are the primary site for void nucleation in pure, high-stacking fault energy metals, specifically tantalum.

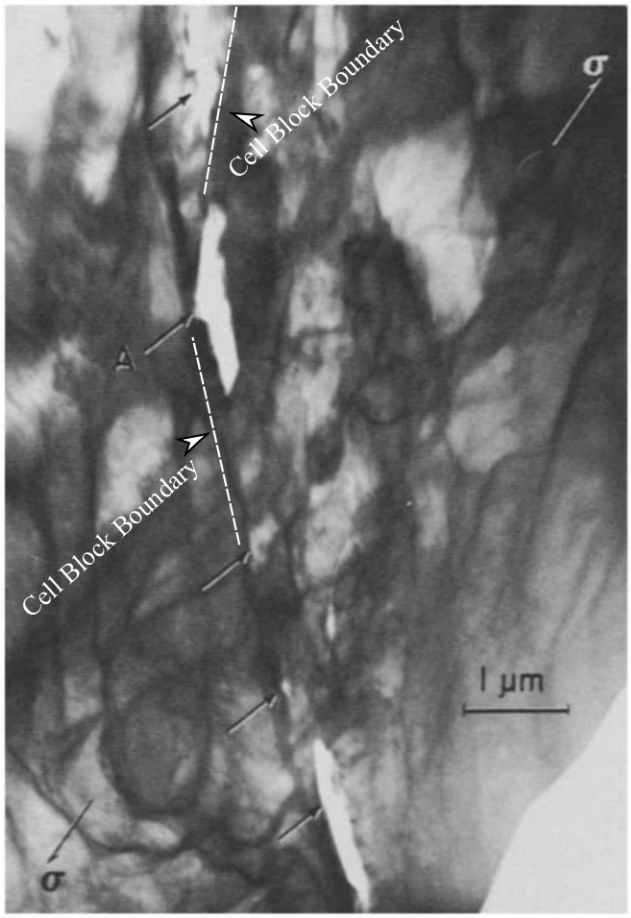


**Figure 36: The black arrows in this transmission electron microscope (TEM) micrograph mark voids that initiated at a deformation-induced dislocation boundary in a strained Be single crystal.**

Beginning with the research of Hansen and Kuhlmann-Wisldorf in the early 1990's [102], work over the past 25 years established that two distinct kinds of deformation-induced boundaries exist: dislocation cell walls and cell block boundaries (these boundaries can also be described as incidental and geometrically necessary boundaries using the terminology of Kuhlmann-Wilsdorf ) [103]. Examples of both of these are illustrated in Figure 37. Dislocation cell walls delineate small (0.5 to 2 $\mu$m), equiaxed volume elements (dislocation cells) and generally have misorientations of less than 2°[104]. Dislocation cells are typically organized into cell blocks: extended, planar features that often run parallel to the trace of a highly stressed slip system [105]. Because both kinds of deformation-induced boundaries generally form during room-temperature deformation, publications before that of Kuhlmann-Wisldorf *et al.* [102] in 1991, including Wilsdorf, generally referred to deformation-induced boundaries as dislocation cell boundaries, cell walls and subgrain boundaries and these terms are still used to refer generally to deformation-induced boundaries. However, important distinctions exist between cell walls and cell block boundaries. For example, cell block boundaries generally have significantly higher misorientation angles than cell walls. In addition, while slip activity within all the

dislocation cells in a single cell block is generally similar, different slip systems are active in neighboring cell blocks [104]. As a result, the misorientation angle across a cell block boundary increases with increasing strain, but the misorientation angle across cell walls does not vary significantly with strain (for strains greater than approximately 0.5 [102, 106, 107, 108]. If relieving the stored strain energy associated with deformation-induced boundaries is the primary mechanism for void initiation in pure metals, it is hypothesized that void initiation at deformation-induced boundaries will primarily occur at (evolving) cell block boundaries rather than (stagnant) cell walls. This study examines this hypothesis by investigating where voids initiate in polycrystalline tantalum following quasi-static tensile deformation.

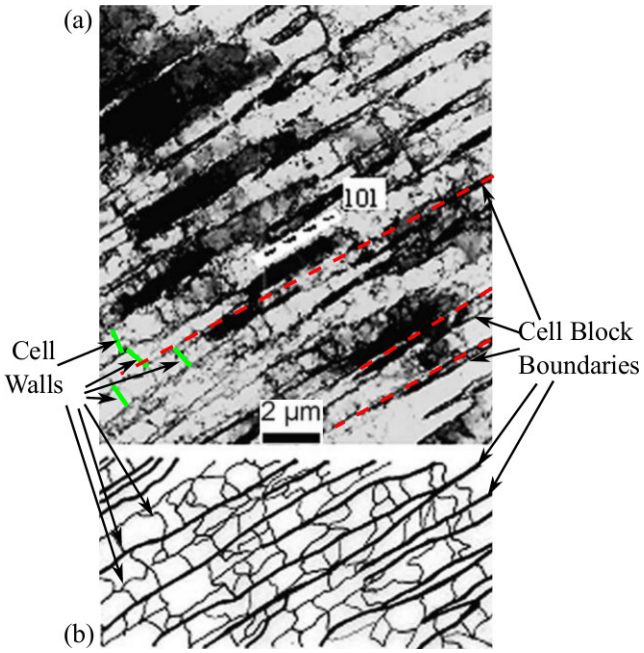


**Figure 37: (a) A TEM micrograph and (b) a sketch of the microstructure in a grain of an interstitial-free steel (a BCC metal) specimen reduced 10% by cold-rolling are shown. Cell block boundaries are marked in bold on the sketch in (b). These cell blocks are subdivided by dislocation cell walls, which are marked in light gray in the sketch in (b).**

To collect statistically-significant evidence of void nucleation in tantalum, scanning electron microscopy (SEM) was used to identify dozens of incipient voids in mid-plane (see Figure 38) cross-sections of deformed, polycrystalline tantalum tensile samples. By examining dozens of voids rather than just a few as with past work [12, 101], it is possible to form a more global perspective on the spectrum of microstructural conditions associated with void nucleation. Electron backscatter diffraction (EBSD), transmission electron microscopy (TEM) and transmission Kikuchi diffraction (TKD) were subsequently used to characterize the microstructure around these voids to answer the following questions:

- what are the microstructural feature(s) associated with quasi-static, room temperature void nucleation in polycrystalline tantalum?
- what commonalities do these microstructural features share that make them the preferred sites for void nucleation?

The answers to these questions provide an important first step towards understanding void nucleation and developing a mechanistically-based model for void nucleation in pure polycrystalline metals.

## 3.2. Experimental Procedure

Incipient voids in tantalum were characterized using *ex-situ* observations of deformed tantalum tensile specimens. Tensile deformation of these specimens was interrupted during late-stage necking but before final fracture. Tests were performed using two similar tantalum sheet materials. In spite of minor differences between these source materials, the failure process appeared generally consistent between them and hence they are both considered representative of pure tantalum failure. The first is a 99.9% Ta sheet material procured from Goodfellow Corporation (Oakdale, PA), hereafter referred to as the Ta A material. This is the same material studied by Boyce *et al.* [101]. The typical chemical analysis of this material is (in ppm) Al 5, Ca 2, Co 1, Cr 5, Cu 2, Fe 30, Mg 5, Mn 2, Mo 100, Na 10, Nb<500, Ni 3, Si 10, Sn 2, Ti 20, V 5, W 100 and Zr 10. The second Ta sheet material is a 99.996% Ta sheet material procured from H.C. Stark (Newton, MA), hereafter referred to as the Ta B material. The chemical analysis of this material, performed by the manufacturer using glow discharge mass spectroscopy (ASTM International 2004), is (in ppm) O 16, N 8, C 5, H 1, Fe .009, Ni .005, Cr .002, Cu .067, Si .05, Ti .003, Mo .42, W 3.3, Nb 5.5, Na .005, Ca .01 and Al .005. No second phases, including face-centered cubic or hexagonal close-packed tantalum [242], second-phase particles, or inclusions were observed in either material when inspected with SEM, EBSD and TEM.

Three smooth tensile bars were extracted from these tantalum materials using electrical discharge machining (EDM): a single tensile bar from the Ta A material and two tensile bars from the Ta B material. The tensile bar from the Ta A material had a thickness of 1.016 mm, a gauge width of 1.549 mm and a gauge length of 8.474. This specimen geometry is identical to the geometry of the smooth tensile bars studied by Boyce *et al.* [101]. The tensile bars extracted from the Ta B material were of nearly identical shape to the single bar extracted from the Ta A material with one notable exception: the gauge region of these specimens had an hourglass radius to ensure strain localization and necking at the center of the gauge region. The minimum gauge width of the Ta B specimens was 1.549 mm. Both tensile bars from the Ta B material were 1.000 mm thick.

The axes of all tensile specimens are defined as the tensile direction (TD), long transverse direction (LTD) and short transverse direction (STD). The final sheet rolling direction of each material was noted and used as a reference for the orientation of tensile specimens. The TD of all three tensile specimens is perpendicular to the final sheet rolling direction and the LTD is parallel to the final sheet rolling direction. EBSD measurements of the as-machined Ta A material, published in reference [101], demonstrate that grains in this material preferentially have their ⟨100⟩ or ⟨110⟩ crystallographic directions aligned along the TD; that is, very few grains in this tensile specimen have their ⟨111⟩ direction aligned along the TD. The size of grains in the as-machined Ta A material was reported by Boyce *et al.* [101] to be between 10 and 120 $\mu$m with an average size of 30 $\mu$m. EBSD measurements from the undeformed grip region of a tested tensile specimen of the Ta B material demonstrate that the texture of this material with respect to the TD is diffuse. The undeformed grain size of this material is between 10 and 195 $\mu$m with an average size of 83 $\mu$m.

To create deformation-induced voids, all three tensile specimens were elongated in uniaxial tension using displacement-control at a constant strain rate of approximately $10^{-2}$ $s^{-1}$. Typical stress *versus* strain data from one of these tensile tests is plotted in Figure 38. Deformation of each specimen was halted during late-stage necking but before complete separation. This was accomplished using the following method. First, the force applied to the specimen was continuously monitored during testing. As illustrated in Figure 38, tensile deformation was interrupted after peak load (onset of necking) when the ratio of the current load to peak load was 0.4 (Ta A), 0.65 (1st Ta B) or 0.70 (2nd Ta B). Hereafter,

the specimens are referred to as Ta 40, Ta 65 and Ta 70 to emphasize the primary distinction between these samples.

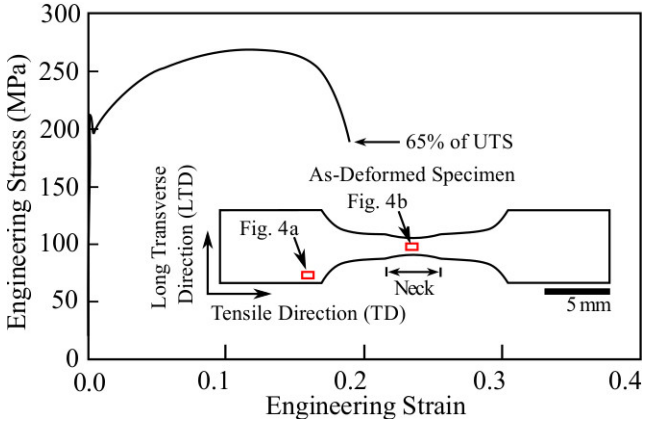


**Figure 38: A plot of stress versus strain data from a tensile test of a tantalum tensile specimen and a schematic of the tensile specimen after testing are shown. The specimen tensile and long transverse directions (TD and LTD) are indicated on the schematic. EBSD data in Figure 39 (a) and (b) are from the regions indicated in this schematic.**

The planar surface (the surface normal to the STD) of each tested tensile specimen was metallographically ground down to the approximate specimen midplane and polished to produce the approximately 40-nm surface finish necessary for EBSD. The polishing procedure is detailed in reference [101]. This procedure allowed the region of highest triaxial stress at the center of the necked gauge region to be directly observed. High-resolution electron channeling contrast (ECC) images of the polished midplane were collected with backscatter and forescatter electron imaging in a Zeiss Supra 55VP field emission SEM. These images were used to locate deformation-induced voids in the necked gauge region of deformed specimens. To verify that the polishing process did not induce voids, it was confirmed that voids were not observed outside of the necked gauge region of deformed specimens.

After locating deformation-induced incipient voids in deformed specimens, the microstructure around them was studied by EBSD. These data were collected in a Zeiss Supra 55VP field emission SEM using Oxford HKL AZtec$^{TM}$ software [243]. Areas 100 $\mu m^2$ or larger around incipient voids were examined using 4×4 binning and a 100 nm stepsize. Areas 5 $\mu m^2$ and smaller around incipient voids were examined using 2×2 binning and a 50 nm stepsize. To characterize the undeformed microstructure of the Ta B material, EBSD data were collected from the undeformed grip region of specimen Ta 70 using 4×4 binning and a 2 $\mu m$ stepsize. EBSD data from the necked gauge region of specimen Ta 70 were collected to characterize the deformed microstructure using 4×4 binning and a 300 nm stepsize. MTEX [244], an extension for MATLAB$^{TM}$, was used to analyze these data. To avoid the common EBSD pitfall of replacing unindexed pixels with interpolated "data", no interpolation was employed in the present study. Interpolation would be particularly problematic in the present study as it creates artificially smooth gradients of rotation in the absence of measured orientation gradients.

TEM foils of the material around two incipient voids were harvested from the metallographically polished surfaces using a FEI Helios dual-beam focused ion beam microscope. One of these incipient voids was on the metallographically-polished surface of specimen Ta 65 and was located using ECC imaging in an SEM. A plan-view specimen of the material around this void was extracted using the

FIB to expose the TD-LTD plane (the plane normal to the STD). A second incipient void was located below the metallographically polished surface of specimen Ta 40 by cross-sectioning the microstructure in the necked gauge region with the FIB until a void was observed. Material around this void was extracted using the FIB and a cross-section view was produced to view the LTD-STD plane (the plane normal to the TD). These TEM foils were subsequently examined in a Philips CM30 TEM operating at 300 keV and utilizing Fresnel imaging conditions.

Transmission Kikuchi diffraction (TKD) [245] was used to measure the crystallographic orientation of the deformed microstructure around both of these incipient voids. TKD was performed using a FEI XL30 field emission SEM. All TKD scans were acquired using a 4 nm stepsize and a working voltage of 30 kV. Oxford HKL AZtec$^{TM}$ software [243] was used to perform these scans. These orientation data were subsequently processed with MTEX; no interpolation of TKD data was employed.

## 3.3. Results

### *3.3.1. The Deformed Microstructure*

The gross evolution of crystallographic orientations following tensile deformation is illustrated in Figure 39. These EBSD maps were collected from the polished midplane of the undeformed grip and deformed gauge regions of Ta 70. The undeformed material, shown in Figure 39(a), consisted of equiaxed grains with an average size of 83 $\mu$m. The texture was diffuse with respect to the tensile direction (TD), though most grains had either their ⟨111⟩ or ⟨100⟩ parallel to the short transverse direction (STD). Following tensile deformation, a strong ⟨110⟩ fiber parallel to the TD was seen in the deformed microstructure shown in Figure 39(b). Grains in the deformed neck were elongated along the tensile direction and had dimensions of approximately 170 $\mu$m and 25 $\mu$m in the TD and LTD. Similar grain morphologies were observed by Boyce *et al.* in fractured tantalum tensile specimens [101]. By dividing the change in grain length along the TD by the original grain size, the local strain in the neck of specimen Ta 70 was estimated to be 1.

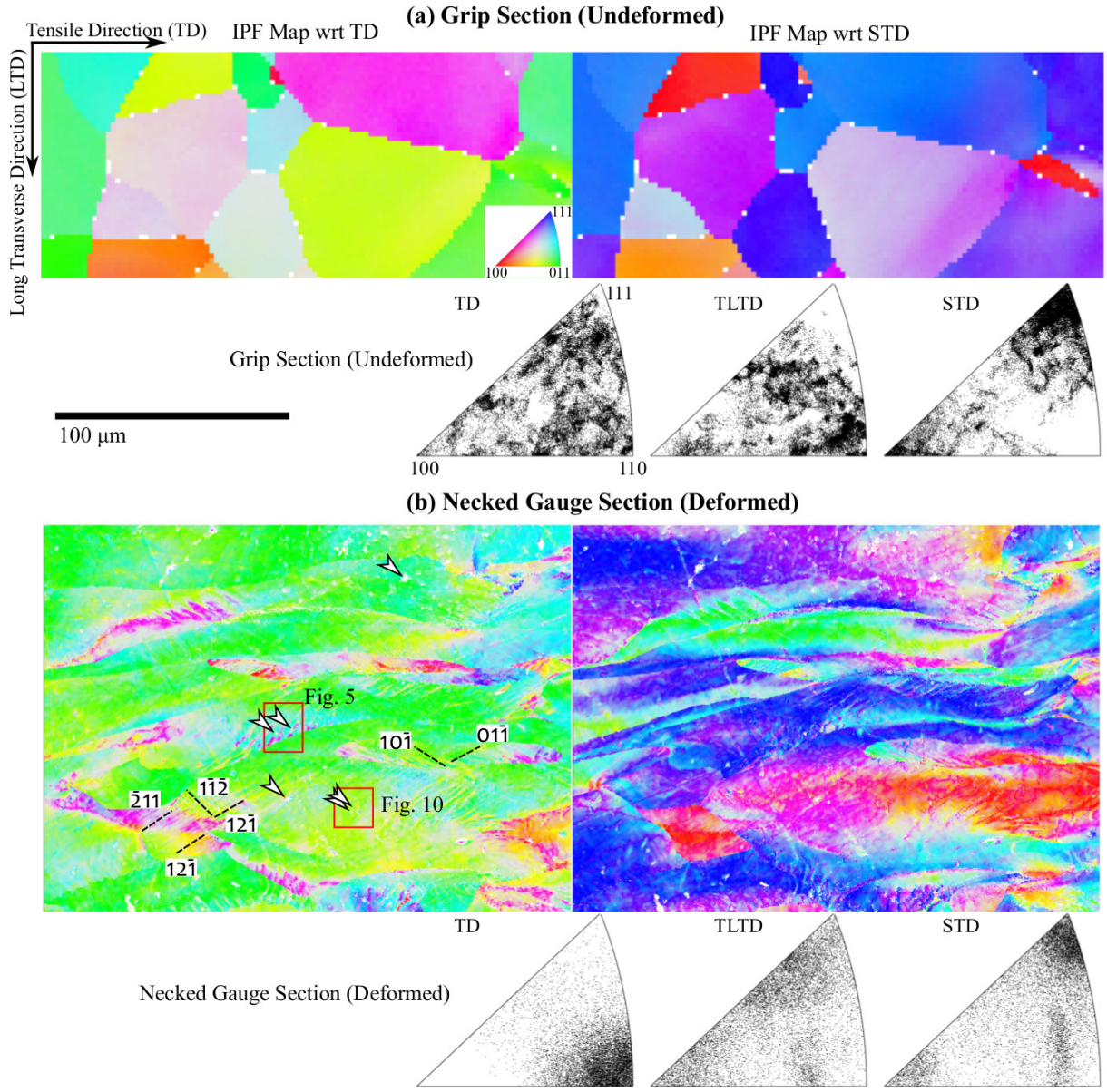


**Figure 39: EBSD data from the (a) undeformed grip and (b) deformed gauge regions of specimen Ta 70 are plotted as inverse pole figure (IPF) maps with respect to (wrt) the tensile direction (TD) and short transverse direction (STD) and as inverse pole figures. Unindexed pixels are colored white. Arrows in (b) indicate the locations of voids. Dashed lines in (b) mark the traces of crystallographic planes. See Figure 38 for reference locations. Both IPF maps are at the same scale.**

Dislocation cell block boundaries were visible throughout the deformed microstructure. They are visible throughout Figure 39(b) as lamellar features with alternating coloring, such as the alternating dark and light cyan features contained in the area labeled the "disturbed zone". Most grains contained one or two sets of well-defined cell blocks that terminated at grain boundaries and extended 10 to 30 $\mu$m into the grains interior. Far from grain boundaries, diffuse networks of dislocation cells were generally observed rather than distinct cell blocks. Many grains also contained narrow zones near the grain boundary where the spacing and shape of cell blocks was significantly different from that approximately 5 to 15 $\mu$m away from the boundary. One of these "disturbed" zones in the mantle of

a grain (near the grain boundary) [246] is highlighted in Figure 39(b). Similar disturbed zones near grain boundaries were observed in other metals after room-temperature deformation ([76, 247, 248]. These disturbed zones are likely caused by the intensified strain gradients near the grain boundaries due to inhomogeneous elastic/plastic incompatibility with the neighboring grains [249] and the pile-up of dislocations at low-transmissability boundaries [250, 251].

EBSD and TEM analysis of cell block boundaries has demonstrated that these boundaries often run parallel to the trace of a slip plane from a highly-stressed slip system, especially in BCC metals [76, 105, 252]. To investigate if the cell block boundaries shown in Figure 39(b) generally conform to this observation, the following procedure was used. First, the Schmid factor of each $\{110\}\langle 111\rangle$ and $\{112\}\langle 111\rangle$ slip system in an individual cell block was calculated. For the six slip systems in that cell block having the largest Schmid factor, the trace of the slip plane was calculated using the cell block's crystallographic orientation as the reference orientation. These traces were then compared with the trace of that cell block's boundary. If the trace of the boundary was misoriented by 6° or less from the trace of the slip plane, it was concluded that the cell block's boundary ran parallel to that slip plane. All cell block boundaries thus analyzed in this study ran parallel to the trace of a $\{110\}$ or a $\{112\}$ plane from one of the six slip systems in that cell block having the largest Schmid factor. Examples of this are marked in Figure 39(b).

## 3.4. Observations of Incipient Voids

To locate incipient voids on the polished midplane of the necked gauge region of each tensile specimen, high-resolution electron channeling contrast (ECC) images were taken in an SEM. These images revealed several large (>10 $\mu$m) cavities in specimen Ta 40 and dozens of incipient (approximately 1 $\mu$m or smaller) voids in specimens Ta 65 and Ta 70. The area fraction of submicron voids in both specimens Ta 65 and Ta 70 was approximately 0.0001. This is similar to values for void area fraction commonly used in models that assume a preexisting void population, 0.001 to 0.0001 [48, 85]. A few of the voids observed in specimen Ta 70 are identified in the EBSD data shown in Figure 39(b). Twenty of the incipient voids in specimens Ta 65 and Ta 70 were subsequently characterized using EBSD. These EBSD data and the ECC images of these voids were used to measure the salient features of these voids, which are summarized in Table 6. It is important to emphasize that EBSD data only provided the average misorientation angle across the deformation-induced boundary associated with each void, not the misorientation across the void.

**Table 6. The following information are reported for each void: the distance from the void to the closest grain boundary, the longest dimension of the void, the average misorientation across the deformation-induced boundary associated with the void and if the void was associated with a cell block boundary (CBB) or a dislocation cell wall (CW). These values were measured using ECC images and EBSD data. No grain boundary was observed in the ~10×10 $\mu$m area analyzed with EBSD around voids 3, 4, and 5; each of these voids are thus at least 5 $\mu$m away from the closest grain boundary. Deformed grains had dimensions of approximately 170 $\mu$m and 25 $\mu$m in the TD and LTD.**

| Void | Distance ($\mu$m) | Length (nm) | Misorientation (°) | Boundary Type |
|---|---|---|---|---|
| 1 | 3.2 | 990 | 22 | CBB |
| 2 | 2.1 | 500 | 32 | CBB |
| 3 | >5 | 470 | 39 | CBB |
| 4 | >5 | 470 | 39 | CBB |
| 5 | >5 | 300 | 26 | CBB |
| 6 | 3.4 | 320 | 50 | CBB |

| Void | Distance ($\mu$m) | Length (nm) | Misorientation (°) | Boundary Type |
|---|---|---|---|---|
| 7 | 4.0 | 480 | 35 | CBB |
| 8 | 12.3 | 250 | 41 | CBB |
| 9 | 6.5 | 560 | 44 | CBB |
| 10 | 23.4 | 940 | 42 | CBB |
| 11 | 11.1 | 700 | 31 | CBB |
| 12 | 6.1 | 370 | 19 | CBB |
| 13 | 0.5 | 900 | 46 | CBB |
| 14 | 1.4 | 500 | 14 | CBB |
| 15 | 0.5 | 530 | 41 | CBB |
| 16 | 4.4 | 460 | 22 | CBB |
| 17 | 3.0 | 400 | 11 | CW |
| 18 | 22.4 | 380 | 8 | CW |
| 19 | 23.5 | 250 | 10 | CW |
| 20 | 8.0 | 670 | 11 | CW |

An example of two typical voids are presented in Figure 40. These voids were located near a grain boundary in a narrow region (colored light blue in the IPF map of Figure 40(b)) misoriented approximately 10° from the surrounding grain. EBSD data reveal that this region was subdivided by distinct, well-defined dislocation cells organized into extended, lamellar cell blocks. Near the grain boundary, the average cell block orientation alternated between having approximately a $\langle 211 \rangle$ (magenta) and a $\langle 331 \rangle$ (cyan) parallel to the TD. The resulting misorientation angle across cell block boundaries varied from 10° to 35° (the misorientation angle between the $\langle 211 \rangle$ and $\langle 331 \rangle$ directions is 20.5°). Alternating $\langle 211 \rangle$ and $\langle 331 \rangle$ cell blocks were separated by boundaries that run parallel to the traces of the $(\bar{1}10)$ and $(21\bar{1})$ slip planes, respectively, as calculated using the method described previously. Outside of this region, cell blocks were separated by low-angle boundaries (5 to 10°) and dislocation cell walls were diffuse. Again, cell block walls outside of this region also ran parallel to the traces of the $(\bar{1}10)$ and $(21\bar{1})$ slip planes.

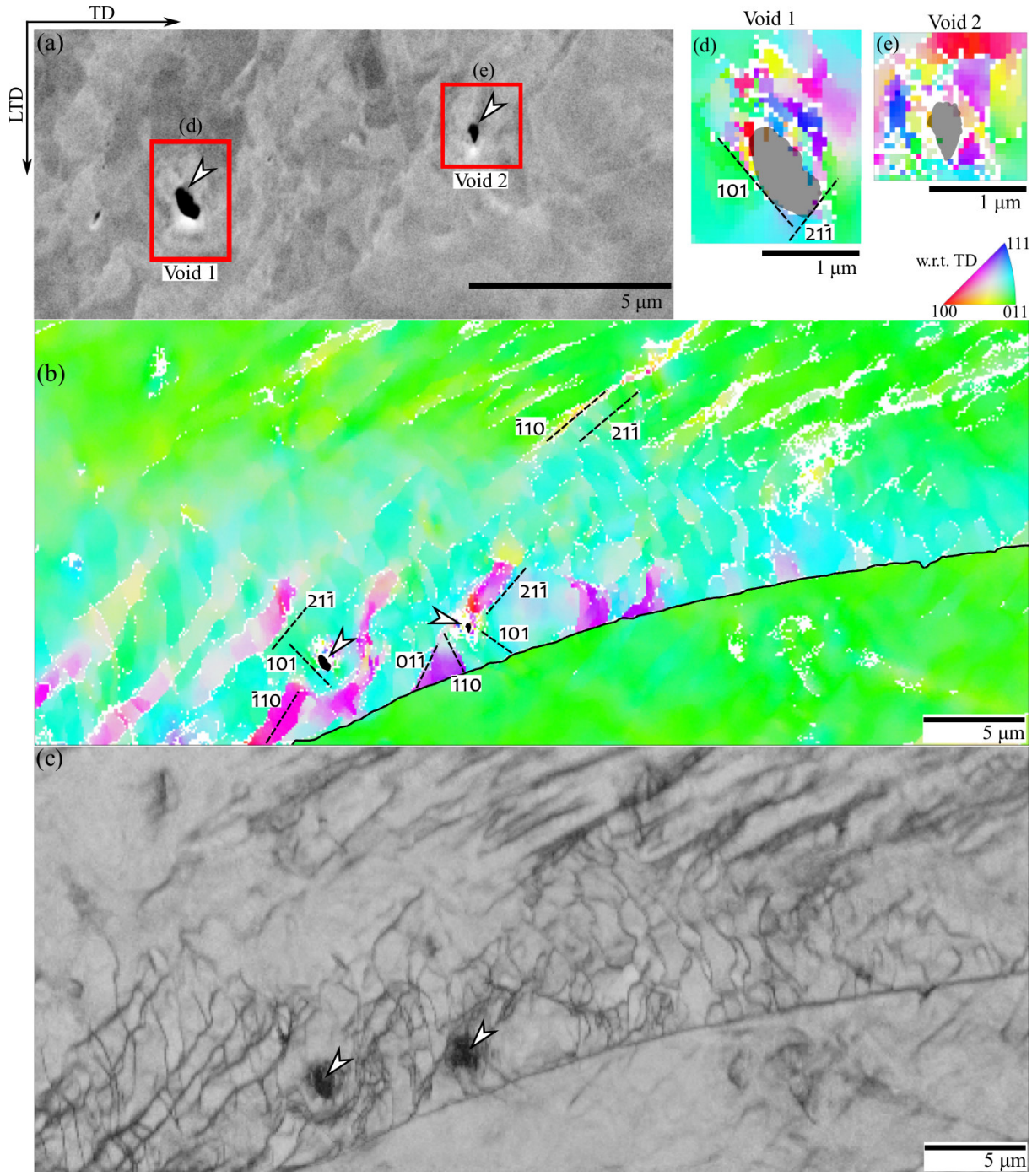


**Figure 40: An electron contrast channeling (ECC) image of two voids are shown in (a). IPF maps, plotted with respect to the TD, of the microstructure around these voids are plotted in (b), (d) and (e). A band contrast map of the EBSD data used to produce (b) is shown in (c); areas of high and low band contrast (good and bad EBSD pattern quality) are colored light and dark, respectively. The shape of each void, measured from the ECC images in (a), is overlaid on these IPF maps; all other unindexed pixels are colored white. Dashed lines in (b) mark the traces of crystallographic planes. The solid line in (b) marks a grain boundary. EBSD data in (b) and (c) were collected with a 100 nm stepsize. EBSD data in (d) and (e) were collected with a 50 nm stepsize.**

EBSD maps of the microstructure immediately around both voids, presented in Figure 40(d) and (e), demonstrate that they were surrounded by a tightly spaced network of dislocation cells, indicative of a high dislocation density near both voids. Void 1 follows the trace of the $(101)$ plane, which runs parallel to the dislocation cell walls observed within the $\langle 331 \rangle$ cell block. Similar analysis of the microstructure around void 2 was inconclusive because of the large spread of orientations around this void.

As the data in Figure 40 illustrate, none of the 20 voids examined in Ta 65 and Ta 70 initiated at a grain boundary thought to be present before deformation. Instead, all of the voids were associated with a deformation-induced dislocation boundary. Most (16 of 20) of these voids shared the following microstructural aspects:

- they were associated with a well-defined, lamellar cell block boundary that had a misorientation of at least 10° and in most cases (14 of 16) greater than 20°, across it and
- they were surrounded by a network of small, highly misoriented dislocation cells.

Boyce *et al.* [101] conjectured that there may be "specific arrangements of intersecting high-angle cell boundaries that are most susceptible to void nucleation." Most (14 of 16) boundaries were indeed high-angle (>20°), though two boundaries appear to be inconsistent with this hypothesis. Additionally, more than half (10 of 16) of these voids occurred near (within 6.5 $\mu$m) of a grain boundary in a region where the spacing and shape of cell blocks suggested that the dislocation density was higher than elsewhere in the grain.

Although EBSD is useful for large-scale characterization, it does not provide sufficient resolution to determine if voids initiate at or simply near cell block boundaries. For this reason, a plan-view (normal to the STD) electron-transparent lamella of a void that typified the microstructural aspects described above was extracted using a dual-beam focused ion-beam (FIB). An ECC image and IPF map of the microstructure around this void before extraction are presented in Figure 41(a). Transmission electron microscopy (TEM) micrographs of this lamella are presented in Figure 42. Sketches corresponding to each TEM micrograph highlight the dislocation cell walls and cell block boundaries near these voids. This image revealed that, what appeared to be a single void in the SEM was most likely two voids that initiated and grew along opposite sides of a cell block boundary, though it is also possible that it is a single void with a concave region. These voids were separated by a narrow isthmus of intact material, less than 10 nm wide. Transmission Kikuchi diffraction (TKD) data from this sample are presented in Figure 41(b) and (c). Although this technique lacks the spatial resolution to index the isthmus material, these data provide important information about the crystallographic orientation of the surrounding microstructure. First, they reveal that these voids initiated at the boundary between an approximately $\langle 110 \rangle$ oriented cell block and an approximately $\langle 100 \rangle$ oriented cell block. These data also allowed the misorientation angle across the deformation-induced boundaries near these voids to be measured. The misorientation angle across every deformation-induced boundary in Figure 41(b) greater than 5° is provided in this figure. The misorientation angle between the approximately $\langle 110 \rangle$ and $\langle 100 \rangle$ cell blocks varied, from 5 to 50°. The misorientation angle across the cell block boundary separating the voids was 15°. These TKD data were combined with the TEM data presented in Figure 42(b) to create the sketch in Figure 42(d) of the misorientation angles across the cell block boundaries and cell walls near the voids. The trace of the slip planes running parallel to these boundaries are also marked on this sketch.

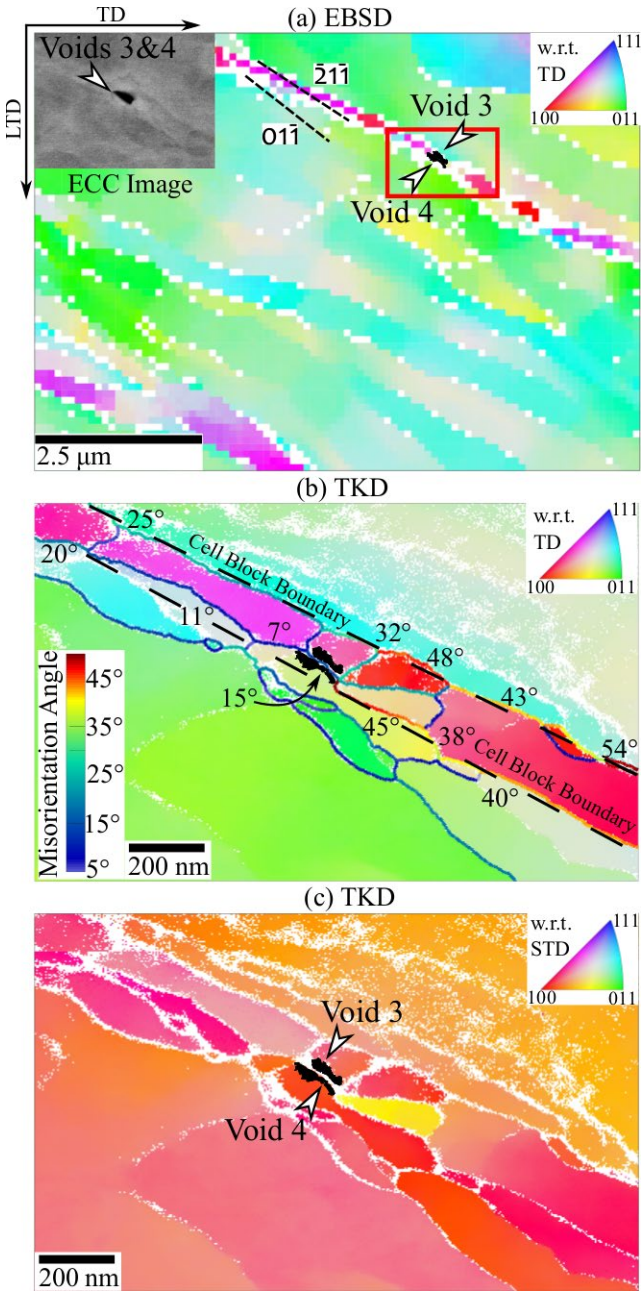


**Figure 41: An ECC image and an IPF map constructed using EBSD showing the microstructure around the two incipient voids presented in Figure 42 are provided in (a). IPF maps constructed using TKD data from this microstructure are plotted with respect to the (b) TD and (c) STD. The misorientation angle across every deformation-induced boundary in Figure 41(b) greater than 5° is colored according to its misorientation angle. The average misorientation angles across the cell block boundaries are labeled. The average misorientation angle across the boundary separating the voids is 15°.**

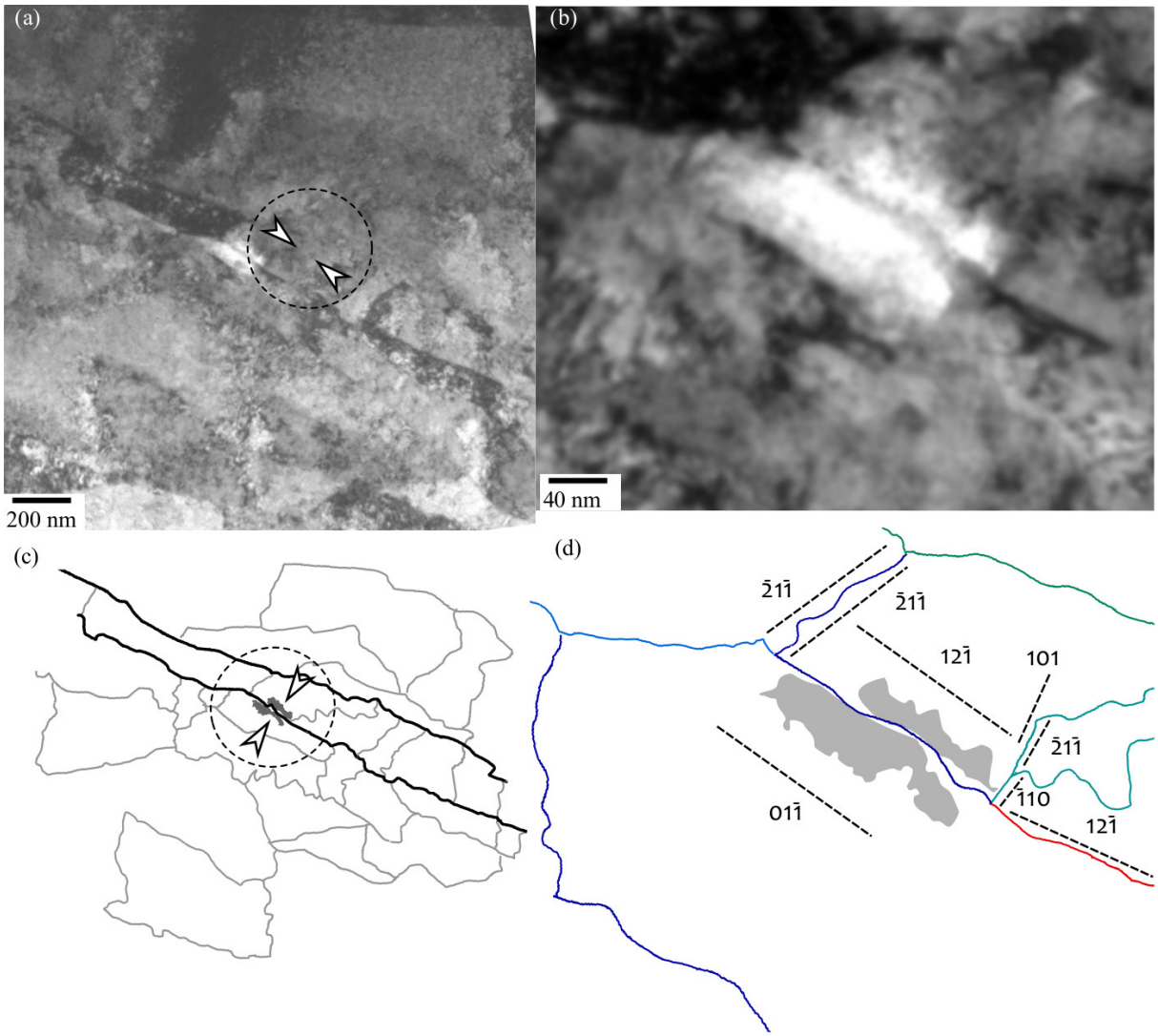


**Figure 42: TEM plan-view micrographs of two voids, labeled voids 3 and 4, that initiated at and grew along opposite sides of a cell block boundary are shown. Sketches below each image illustrate the dislocation structure around these voids. The shape of the voids from (a) and (b) are overlaid on the sketches shown in (c) and (d). The cell block boundaries and cell walls identified in (a) are colored black and gray, respectively, in (c). The deformation-induced boundaries in (d) are colored according to the average misorientation angle across them, as measured using TKD data. Dashed lines in (d) mark the traces of crystallographic planes.**

To prove conclusively that voids do not initiate at grain boundaries, one would have to characterize the entire void in three-dimensions. At a minimum, submicron voids would first have to be located below the surface using X-ray microtomography or a similar technique with adequate resolution. However, for the present study, it was instead chosen to locate a three-dimensional void below the metallographically polished surface and characterize its cross-section normal to the TD. To locate such a void, FIB was used to cross-section material in the necked gauge region of a specimen until an

incipient void was located. Practically, the small volume density of voids in specimens Ta 65 or Ta 70 (approximately 0.0001) offered only a very low probability of unearthing a subsurface void. To increase the likelihood of success, the necked gauge region of specimen Ta 40, which had a larger density of voids, was cross-sectioned using FIB. After many unsuccessful attempts, a single incipient void was found below the metallographically polished mid-plane of this specimen's necked gauge region. A cross-section normal to the TD was extracted using a FIB lift-out technique and polished until it was electron transparent.

TKD data and a TEM micrograph of the incipient void found below the metallographically polished surface of Ta 40 are shown in Figure 43. Figure 43(a) shows TKD data plotted as an IPF map colored with respect to the TD. Deformation-induced boundaries in Figure 43(a) with a misorientation of greater than 5° are labeled according to the average misorientation angle across them. Figure 43(b) shows the same TKD data as an IPF map colored with respect to the STD. The arrow in Figure 43(b) highlights the small, highly-misoriented cell observed at one end of this incipient void. It is conjectured from these TKD and TEM data that this cell is one end of a larger cell block that was truncated during sample preparation. The TEM micrograph in Figure 43(c) and the corresponding sketch in Figure 43(d) reveal the structure of the deformation-induced boundaries around this void. Together, these TKD and TEM data show that this void initiated at and grew along a cell block boundary with an approximately 10 to 15° misorientation angle across it. This cell block boundary followed the trace of the $(\bar{2}11)$ and $(\bar{2}1\bar{1})$ slip planes. Intriguingly, the left end of the void intersected a high-angle boundary between what are likely two cell blocks: one oriented with its $\langle 100 \rangle$ parallel to the TD, the other with its $\langle 110 \rangle$ parallel to the TD.

The results presented in the previous paragraphs characterized sixteen of the twenty incipient voids observed in specimens Ta 65 and Ta 70 and the only incipient void examined in specimen Ta 40. Figure 44 presents one of the four voids that did not exhibit these characteristics. The ECC image and EBSD data presented in this figure show an incipient void surrounded by a diffuse dislocation structure. Instead of clearly-defined, lamellar cell blocks, the only distinct dislocation structure near this void was a dislocation cell, faintly visible in the inset provided in Figure  Figure 44(c) and misoriented approximately 10° relative to the surrounding microstructure. Three other voids also initiated at a dislocation cell wall within a diffuse dislocation structure with no distinct cell blocks. In each case, the misorientation angle across the dislocation cell wall associated with the void was 10° or more.

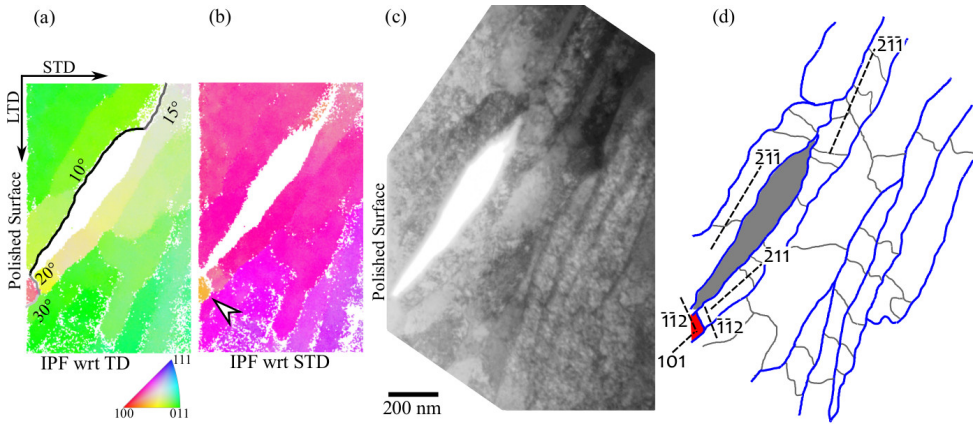


**Figure 43: TKD data from the microstructure around a void are plotted as IPF maps with respect to the (a) TD and (b) STD. The average misorientation angle across each deformation-induced boundary greater than 5° is provided in (a); the average misorientation across the void is 10°. A TEM micrograph of this void is shown in (c). A sketch of the cell block boundaries and cell walls, colored blue and gray, respectively, around this void is provided in (d). Dashed lines in (d) mark the traces of crystallographic planes. The small volume element at the lower left end of the void, indicated with an arrow in (a), is highlighted red in (d). All images are at the same scale.**

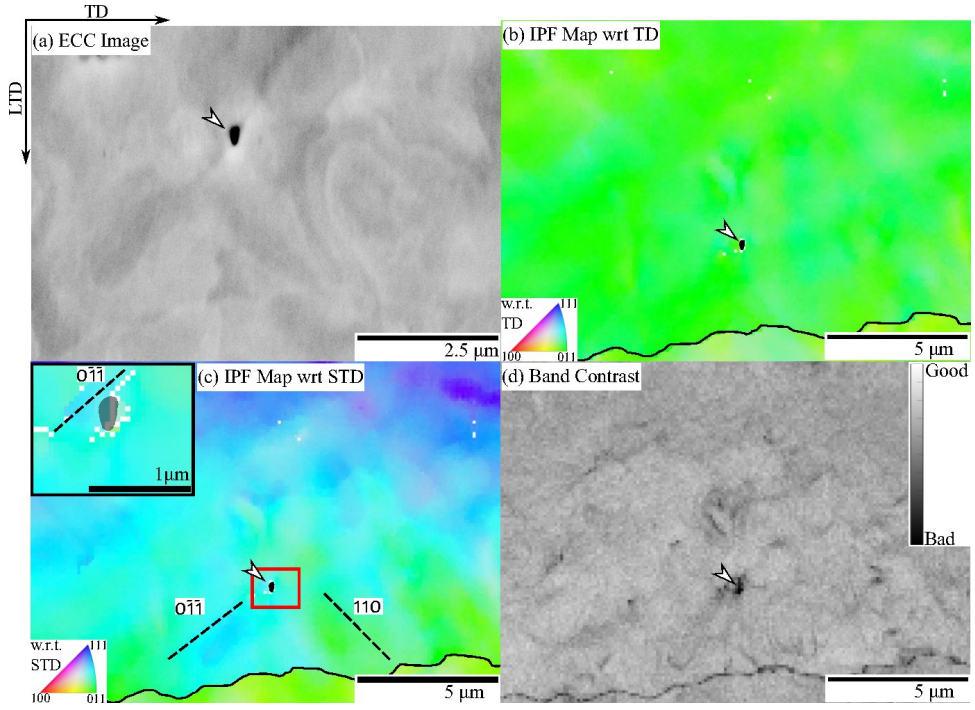


**Figure 44: TKD An electron contrast channeling (ECC) image of a void is shown in (a). IPF maps plotted with respect to the TD and STD of the microstructure around this voids are plotted in (b) and (c). The shape of each void, measured from the ECC image shown in (a), is overlaid on these IPF maps. All other unindexed pixels are colored white. Dashed lines in (c) mark the traces of crystallographic planes. A band contrast map of the EBSD data used to create (b) and (c) is plotted in (d)**

## 3.5. Discussion

### *3.5.1. Void Initiation*

This study presents EBSD observations of multiple incipient voids in a single-phase, bulk, polycrystalline metal for the first time. These data allow us to test the commonly held hypothesis that voids in pure metals nucleate at grain boundaries [100, 211]. Consider the two voids shown in Figure 40. Both of these voids nucleated near a grain boundary in the so-called mantle region [246] but are clearly not directly associated with the boundary. In addition to these two voids, seven other voids were observed within 5 $\mu$m of the closest grain boundary. In each case, though, the void did not intersect a grain boundary. Even though EBSD only provides data on a two-dimensional slice of the void, it is important to remember that all of these voids were 1 $\mu$m or less in diameter. Hence, it is highly improbable that each of these voids intersected a grain boundary just above or just below the polished surface. The likeliest explanation is that voids in pure tantalum initiate at some other microstructural feature.

The possibility that dislocation cell walls, cell block boundaries or both are the primary microstructural features where voids initiate is now considered. The EBSD data in Figure 40 provide evidence that voids nucleate at deformation-induced boundaries similar to those presented in Figure 37. Based on observations of similar microstructures around 14 other voids, it is clear that incipient voids in polycrystalline tantalum generally nucleate near a high-angle cell block boundary. The utility of these EBSD data are, unfortunately, limited by poor indexing near the voids and the approximately 50 nm spatial resolution of EBSD. While it is impossible to use these data to determine if a void initiated at a cell block boundary, a cell wall, or elsewhere, they allow us to make one important conclusion: voids are generally associated with a high density of deformation-induced boundaries. This is demonstrated in Figure 40(d) and (e), which show that each of these voids is surrounded by a network of highly misoriented dislocation cells less than 1 $\mu$m in diameter. In addition, most voids nucleated in a region where distinct cell block boundaries and cell walls could be easily distinguished in the EBSD data (see Figure 40(b) and (c)), suggesting a high density of dislocations within each boundary. A high density of dislocations and deformation-induced boundaries thus appears to generally be necessary for void initiation.

EBSD data allowed representative voids to be identified. Subsequent TEM and TKD analysis of three of these voids showed that they nucleated at cell block boundaries. It is reasonable to conclude from this that cell block boundaries are the primary site for void initiation in tantalum. This conclusion allows us to reinterpret the observations of Wilsdorf and coworkers [97] using modern terminology. Consider the voids shown in Figure 53, which initiated at what Gardner *et al.* [13] termed a "dislocation cell boundary". This boundary is clearly lamellar, extends for several microns and runs parallel to similar neighboring boundaries. Emphasizing the distinction between cell walls and cell block boundaries illustrated in Figure 37, it is more appropriate to term this boundary a cell block boundary rather than a dislocation cell boundary. Based on the results of the present study, only a subset of deformation-induced boundaries, the cell block boundaries, are of primary importance for void initiation in pure metals. A mechanistic description of void nucleation in pure metals clearly must involve a description of the evolving cell block structure. This cannot be done with current modeling capabilities; crystal plasticity models do not capture the details of cell block formation and dislocation dynamics cannot yet handle the very large strains associated with cell block formation [253]. Work in both of these areas to bridge this gap is necessary before a mechanistic model for void nucleation in pure metals can be created.

The results of the present study indicate that, contrary to the hypothesis of Jagannadham *et al.* and others [81, 161], voids do not nucleate at deformation-induced boundaries to relieve the stored energy of the boundary. The area density of dislocations which must be stored in a deformation-induced boundary to create a lattice misorientation angle $\theta$is on the order of $\theta/b$ [254]. As a first order approximation, void initiation becomes energetically favorable for a particular boundary once a critical misorientation angle is reached. Figure 41 and Figure 42 show that the misorientation across the cell block boundary separating voids 3 and 4 is 15°. If a minimum misorientation angle across a deformation-induced boundary is sufficient for void nucleation, we would expect voids to have initiated at the neighboring portion of the cell block boundary which has a 50° misorientation across it. No other voids were observed in near voids 3 and 4. In addition, although most of the voids observed in these tantalum materials are associated with cell block boundaries, four incipient voids were observed in areas of the microstructure that had no distinct cell block boundaries. As Figure 44 illustrates, the dislocation structure around these voids was diffuse, though each void was associated with a dislocation cell wall with a 10° or more misorientation angle across it. If voids nucleate to relieve the stored energy of deformation-induced boundaries, we would not expect to see voids initiating in areas of the microstructure with no discernible high-angle deformation-induced boundaries. It is possible that these four voids may have nucleated at a cell block boundary that is above or below the plane of view. Additionally, the wavy, diffuse lines following the traces of the $(110)$ and $(0\bar{1}\bar{1})$ planes faintly visible in the band contrast data plotted in Figure 44(d) suggest that deformation-induced boundaries similar to that shown in Figure 37 exist in this microstructure but were not resolved by EBSD. However, a likelier explanation for the occurrence of these voids and the results presented in Figure 41 and Figure 42 is that void initiation is a product of vacancy condensation. This hypothesis will now be discussed in further detail.

The concentration of stored vacancies increases rapidly during cold-deformation and can reach a maximum value of $10^{-4}$, the thermal equilibrium void concentration near the melting temperature, after only moderate strains $\varepsilon \approx 0.5$ [173, 255, 256, 257]. General agreement has been found between experimental results and Saada's model [7, 175, 176], according to which the concentration of vacancies produced by cold-work is proportional to the work done as

$$c_v = A \cdot \frac{1}{G} \int_0^{\varepsilon} \sigma \, \mathrm{d}\varepsilon \qquad 9$$

where $G$ is the shear modulus, $\sigma$ and $\epsilon$ are the applied stress and strain, and $A$ is a constant on the order of 0.1[174, 218, 258]. According to this model, the stored vacancy concentration in the deformed gauge region is on the order of $10^{-5}$. Vacancy formation during cold-deformation is attributed to the motion of jogged screw segments and the mutual annihilation of dislocation branches of opposite signs [175, 176, 179, 259, 260]. Because cell block boundaries are made up of many intersecting dislocations, it is conjectured that cell block boundaries will have a higher vacancy concentration than the surrounding material. By the same argument, the vacancy concentration at a cell block boundary will increase with increasing dislocation density. Cell block boundaries also present a ready path for vacancy movement by dislocation pipe diffusion. For vacancy concentrations significantly larger than the equilibrium level, vacancy condensation can lower the free energy of the system [179]. Based on this assumption, Cuitino *et al.* [179] demonstrated the feasibility of void nucleation ahead of a growing crack by vacancy condensation during quasistatic deformation of pure, single crystalline copper. During high-temperature creep deformation, a similar mechanism is thought to result in void nucleation at grain boundaries [189]. It is thus hypothesized that void initiation in tantalum was the result of vacancy condensation at deformation-induced boundaries. This hypothesis implies that void

nucleation is a stochastic process whose likelihood increases with increasing dislocation density. It is then to be expected that most voids would be associated with cell block boundaries but that a few would initiate elsewhere.

A mechanism of vacancy condensation also explains why voids initiated at deformation-induced boundaries rather than grain boundaries. Vacancies are more likely to condense into a void at deformation-induced boundaries than at grain boundaries for at least two reasons. First, because deformation-induced boundaries have longer range stress fields around them than do grain boundaries [261, 262] more vacancies are attracted to cell block boundaries and cell walls than to grain boundaries. The network of dislocations running to these cell walls and cell block boundaries provides a ready path for vacancies to diffuse to them. Second, dislocation glide will generally sweep vacancies into deformation-induced boundaries rather than grain boundaries. The experimental observation that voids initiate at deformation-induced boundaries rather than grain boundaries is thus reasonable if vacancy condensation is responsible for void nucleation.

It is important to note that the results of the present study, namely that voids nucleate at cell block boundaries in pure tantalum, are not necessarily restricted to pure metals. Cell block boundaries may also be important sites for void nucleation in materials that contain fine second-phase particles that are strongly bonded to the matrix. For example, Chan *et al.* noted that the density of voids in precipitation-hardened Al-Cu alloys was many times larger than the particle density [91, 92]. They concluded from this that voids nucleated at microstructural features other than particles. It may thus be useful to investigate where voids nucleate in such materials. In addition, there is no reason to expect significant differences between void initiation in tantalum and other single-phase BCC and FCC metals of high-stacking fault energy. Indeed, by exploring how different slip conditions influence void initiation, important insights into void nucleation may be gained.

## 3.6. The Early Stages of Void Growth

During its early stages, void growth is almost entirely restricted to cell block boundaries. This is clearly seen in the TEM and TKD data presented in Figure 42 and Figure 43. Instead of being spheres, as typically assumed by models of void growth [31, 32], voids in tantalum appeared ellipsoidal in ECC images (see Figure 40 and Figure 41). No spherical voids were observed. Inspection with TEM demonstrated that the apparently ellipsoidal voids shown in Figure 41 had aspect ratios of approximately 5:1. The morphology of these voids indicates that the microstructure, rather than the global triaxial stress state, controls the morphology of incipient voids in tantalum.

It is widely assumed that incipient voids grow by emitting dislocations [211, 263]. Several features of these incipient voids suggest that they instead grew by consuming dislocations from the bulk. First, consider the microstructure around void 1 shown in Figure 40. Unlike the neighboring cell block boundaries, which are lamellar and run roughly parallel to a single crystallographic trace, the cell block boundary to the right of void 1 curves around this void along a radius of approximately 1 $\mu$m. In addition, much of the microstructure around void 1 has an approximately $\langle 331 \rangle$ orientation, the average orientation of most of the surrounding microstructure. This suggests that void 1 provided a sink for dislocations and allowed the neighboring microstructure to relax back to its original orientation. Second, if voids grow by consuming dislocations, we would expect a lower density of deformation-induced dislocation boundaries around void 1 than around void 2 since void 1 is about twice as large as void 1. This is indeed seen in Figure 40. Finally, as discussed in the previous paragraph, the early stages of void growth are restricted primarily to the cell block boundary. Cell block boundaries are made up of dense tangles of dislocations and contain significantly larger densities of dislocations than the surrounding microstructure. Void growth appears to be restricted to these areas

of high dislocation density, suggesting that voids grow by consuming dislocations. Recently, Nguyen *et al.* showed the improbability of dislocation emission from a growing void during quasistatic tensile deformation [212]. Void growth by consuming dislocations is thus a reasonable alternative to the widely held premise that voids grow by emitting dislocations.

## 3.7. Conclusions

Void initiation in pure tantalum was studied *ex-situ* using SEM, EBSD, TKD and TEM. Dozens of deformation-induced, incipient voids were observed with the SEM in the necked gauge regions of tested tantalum tensile specimens. To determine where these voids initiated, twenty voids were characterized with EBSD. Although it is commonly assumed that voids in pure metals initiate at grain boundaries or twin intersections, none of the voids observed in tantalum were associated with these features. Instead, most (16 of 20) of them initiated at and grew along well-defined, lamellar cell block boundaries. These voids shared the following characteristics:

- they were associated with well-defined, lamellar cell block boundaries that ran parallel to the trace of a {110} or {112} plane from a slip system with a high Schmid factor,
- the misorientation angle across the cell block boundary associated with the void was always larger than 10° and, in 14 of 16 cases, greater than 20° and
- they were surrounded by a network of small, highly misoriented dislocation cells.

Subsequent TEM and TKD analysis of three incipient voids revealed the complex dislocation structure around each void. In all cases, the voids clearly initiated at and grew along a cell block boundary. Cell block boundaries are thus of primary importance for void initiation in pure metals.

In addition to these voids, four other voids which did not share these characteristics were observed. Each of these voids nucleated at a low-angle dislocation cell wall. A large misorientation angle across a deformation-induced boundary is thus not necessary for a void to initiate at that boundary. This suggests that voids do not initiate to relieve the stored energy associated with a deformation-induced boundary. Instead, it is hypothesized that that vacancy condensation is the primary mechanism for void nucleation. Since vacancy condensation is a stochastic process whose likelihood depends on many factors and generally increases with increasing dislocation density, it is expected that a small percentage of voids will nucleate in areas of low dislocation density. Void nucleation by vacancy condensation also explains why voids initiated at deformation-induced boundaries rather than grain boundaries. The present investigation thus suggests that voids in pure materials nucleate by vacancy condensation.

Several features of the incipient voids observed in tantalum suggest that they grew by consuming dislocations from the bulk rather than emitting dislocations. This mechanism of void growth provides a reasonable alternative to the widely held premise that voids grow by emitting dislocations.

# 4. VOID GROWTH BY DISLOCATION ADSORPTION

We propose a dislocation adsorption-based mechanism for void growth in metals, wherein a void grows as dislocations from the bulk annihilate at its surface. The basic process is governed by glide and cross-slip of dislocations at the surface of a void. Using molecular dynamics simulations we show that when dislocations are present around a void, growth occurs more quickly and at much lower stresses than when the crystal is initially dislocation-free. Finally, we show that adsorption-mediated growth predicts an exponential dependence on the hydrostatic stress, consistent with the well-known Rice-Tracey equation.

## 4.1. Introduction

The ductile fracture process in metals is relevant to a number of failure scenarios including quasi-static tearing [2, 90], dynamic spall [264], creep rupture [231], irradiation creep [265], and wear debris generation [266]. Typically, the fracture surfaces of these metals exhibit a characteristic pitted "ductile dimple" appearance indicative of the microvoid coalescence rupture process [55]. Often ductile fracture is due to the nucleation, growth, and coalescence of microscale voids [55]. It is usually assumed that the material contains a pre-existing population of hard particles or inclusions made from secondary phases. Void nucleation then occurs when these particles crack or the interface between the particles and matrix delaminates [46, 98, 267]. The voids grow under the action of plastic deformation around the voids, driven by hydrostatic stresses [31, 268]. Final rupture occurs when the voids coalesce, which typically occurs when ligaments between adjacent voids reach some critical thickness leading to shear banding or ligament fracture.

This basic picture for rupture in ductile solids has been around for nearly 50 years. Despite this fact, many of the details surrounding it are poorly understood, including the micromechanics of void nucleation and growth. For example, ductile rupture is still observed in materials that do not contain hard particles or pre-existing voids, making it unclear how the voids nucleate in the first place [13,14]. There are numerous competing continuum-scale phenomenological models for the ductile rupture process [15] including the Gurson model [16], an adaptation by Tvergaard and Needleman [17], modifications to account for shear localization [18], and stress triaxiality models [19]. The Sandia Fracture Challenge has illustrated the ongoing disagreement with regard to the most appropriate failure models and their difficulties in blindly predicting rupture scenarios [20,21]. Many of these difficulties arise from assumptions made about the underlying micromechanical mechanisms that drive void nucleation and growth; for example, many models assume a pre-existing void density and hence neglect void nucleation altogether. At lower length scales such as the scale of individual grains, there is even broader disagreement as to the proper models to describe the rupture process. These discrepancies are due in part to a lack of clear fundamental understanding of the detailed unit mechanisms governing nucleation, growth, and coalescence.

In this work, we focus on obtaining a detailed micromechanical understanding of the void growth process. Much of the literature on void growth focuses on continuum theories which characterize the void growth rate as a function of the stress state [268, 269]. Of these, perhaps the most famous is the work by Rice and Tracey [31], later corrected by Huang [270], who solved for the growth rate of an isolated void in a rigid-perfectly plastic solid loaded with applied strain rate tensor $\dot{\epsilon}_{ij}$ and hydrostatic stress $\sigma^H$. They obtained the simple result for the void growth rate that

$$\frac{\dot{R}}{R} = \alpha \exp\left(\frac{3\sigma^H}{2\sigma_Y}\right)\dot{\epsilon}^{eq} \quad (10)$$

where R is the void radius, $\sigma_Y$ is the yield strength, $\dot{\epsilon}^{eq} = \sqrt{\frac{2}{3}\dot{\epsilon}_{ij}\dot{\epsilon}_{ij}}$ is the equivalent plastic strain rate (using Einstein notation), and $\alpha = 0.427$ is a numerically obtained constant [270]. Hence, the continuum theory predicts an exponential dependence on the hydrostatic stress. The Rice-Tracey equation was recently validated against detailed X-ray tomographic measurements of void growth [78]. According to Rice-Tracey, voids grow as plastic strain accumulates around them, but the detailed micromechanics are unclear.

In an effort to fill this micromechanical knowledge gap, numerous atomistic studies of void growth have been performed in the last decade [209, 210, 211, 263, 271, 272]. The key finding in all of these studies is that voids grow by nucleating dislocations at the surface of the void. However, such a mechanism poses a fundamental dilemma. In particular, Nguyen and Warner [212] showed using molecular dynamics and transition state theory calculations, that dislocation nucleation from the surface of a void in pure aluminum is a tremendously slow process. For example, the nucleation rate under 0.78 GPa of shear stress is one dislocation per year! In order to obtain nucleation rates on the order of 1 $s^{-1}$, applied stresses need to exceed 1 GPa. While stresses of this magnitude may be relevant to high loading rates (e.g., shock loading [208]), they are well beyond the strengths of many structural metals under quasi-static loading.

In this work, we resolve this problem by proposing that void growth via adsorption of dislocations from the surrounding bulk is the primary mechanism of growth. Adsorption-mediated growth was recently shown to be a viable mechanism for small amounts of void growth (< 0.1% by radius) by Chang et al. [213]. While Chang et al.'s prior work opens the possibility that dislocation adsportion may supplant emission as the dominant deformation mechanism, their use of dislocation dynamics was limited to low dislocation densities below those experimentally observed at relevant cell wall boundaries [166], and suggested that the adsorption mechanism may be limited to only the very early stages of void growth. Many important questions remain to be answered before the importance of adsorption-mediated growth can be understood, however. Namely: what are the key dislocation processes underlying the mechanism?; what is the connection, if any, between nucleation-mediated and adsorption-mediated growth?; and, what growth rates are predicted by adsorption-mediated growth and how do they compare with experiments? In this work, we address these questions, demonstrating that 1) the dislocation processes enabling adsorption-mediated growth (glide and cross-slip) occur rapidly, 2) even in a scenario where nucleation-mediated growth occurs (no dislocations present initially), adsorption-mediated growth quickly takes over as the mechanism of growth, and 3) growth rates predicted by adsorption-mediated growth are consistent with the experimentally validated Rice-Tracey equation. Lastly, we argue that our results elucidate recent experimental observations of void growth at regions with elevated dislocation density (cell block boundaries) [166, 273]. Combined together, we believe our results demonstrate that adsorption-mediated growth is dominant among the possible growth mechanisms.

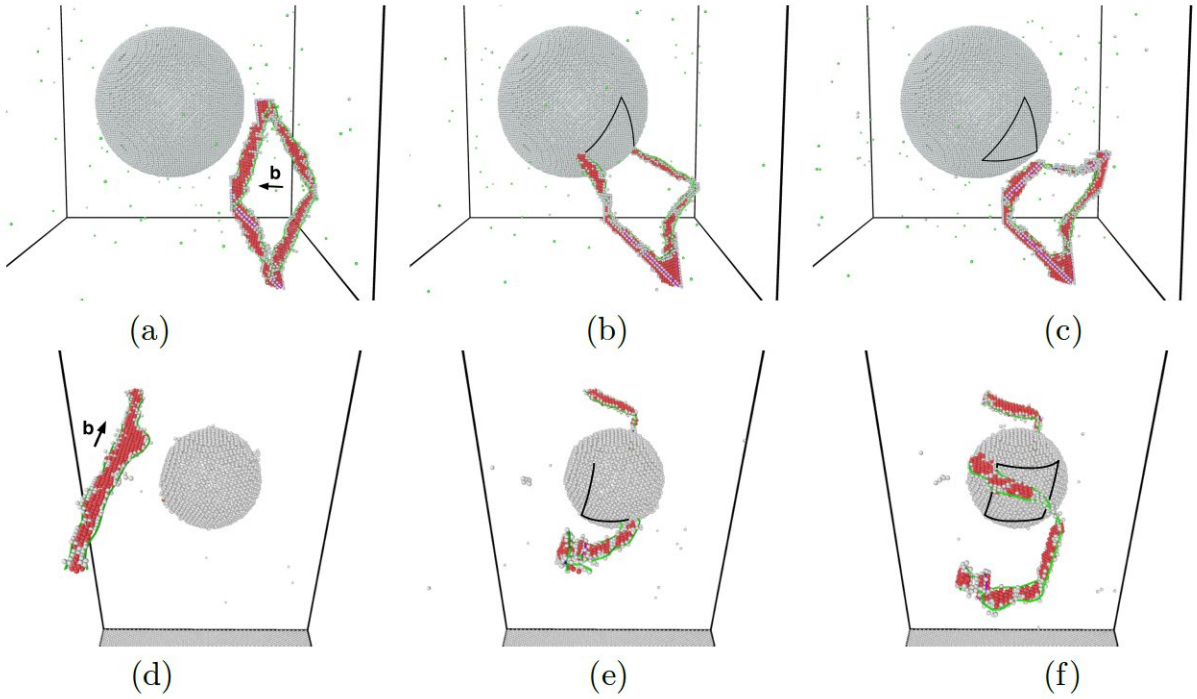


**Figure 45. Dislocation-void interactions under an applied hydrostatic stress. Black lines denote approximate dislocation trajectories on the surface of the void. (a-c) Prismatic dislocation loop loaded at $\sigma^H$ = 2 GPa with void of radius $R_0$ = 7.5 nm. (a) Initial configuration. (b) Configuration after loop glides into the void. (c) After the loop cross-slips and forms a closed-path on the void's surface. (d-f) Screw dislocation loaded at $\sigma^H$ = 3.7 GPa with void of radius $R_0$ = 3 nm. (d) Initial configuration. (e) Configuration after the dislocation cross-slips and glides across the face twice. (f) After the dislocation cross-slips and glides two more times tracing out a prismatic dislocation loop. Atoms at the void surface and in dislocation cores are colored white, and inside stacking fault ribbons are colored red. Shockley partial dislocation lines are shown in green. Image made using OVITO [25].**

## 4.2. Methods and Results

We study void growth at a temperature of 300 K in face-centered cubic aluminum using the embedded atom method potential of Mishin et al. [274] and the molecular dynamics code LAMMPS [275].

To begin our studies, we focus on the interaction of isolated dislocations with a single void in order to elucidate underlying mechanisms. We introduce a void of radius $R_0$ and impose a constant hydrostatic tensile stress on the simulation cell. Treating the void as a spherical cavity in an isotropically elastic matrix under a pure hydrostatic load, we can compute the equivalent Eshelby eigenstrain [276] to obtain a stress field around the void of

$$\sigma_{ij} = \frac{1}{2}\sigma^H \left(\frac{R}{r}\right)^3 \left(\delta_{ij} - \frac{3x_i x_j}{r^2}\right) \quad \textbf{(11)}$$

where $\delta_{ij}$ is the Kronecker delta and $r = \sqrt{x_i x_i}$. The resulting maximum shear stress at the surface of the void is $\frac{3}{4}\sigma^H$. We study two dislocation geometries: a prismatic (meaning the initial plane of the loop is orthogonal to the Burgers vector) dislocation loop and a straight screw dislocation. Note that

if a void were not present, there would be no driving forces acting on the dislocation lines since the system is under a pure hydrostatic stress state. Figure 45 depicts the response of the dislocation lines. In both cases, the dislocation lines are attracted to the void. After initially colliding with the void, the dislocations quickly glide across its face, and then cross-slip onto another glide plane where they are able to glide again. After this process repeats several times, the end result is that closed dislocation loops are traced out on the void's surface. The volume change of the void after the dislocation loops are traced out is [277, 278]

$$\delta V = \int_S \mathbf{b} \cdot d\mathbf{A} = \int_S (\mathbf{b} \cdot \mathbf{n})\, dA \quad \textbf{(12)}$$

where **b** is the Burgers vector, **n** is the outward normal of the void surface, and ***S*** is the area traced out by the dislocation line. Note that the exact same volume change would occur if instead a loop with an oppositely signed Burgers vector and the same shape were nucleated from the surface of the void [43]. Hence the underlying mechanics is exactly the same between adsorption-mediated and nucleation-mediated growth. The key point is that adsorption-mediated growth can occur much more rapidly since it relies on cross-slip and glide, which are known to occur readily over typical experimental timescales. Furthermore, the externally-sourced dislocations can be produced much more quickly (via conventional multiplication processes) than surface-based nucleation. Since we are constrained to atomistic timescales in these simulations, the stresses need to be large (> 2 GPa), however, to accelerate the processes. Demonstration of the basic unit-mechanisms underlying adsorption-mediated growth is the first major contribution in this work.

Next, we demonstrate the behavior of a crystal containing voids under an applied hydrostatic tensile strain rate, a case that has been considered by several researchers [210, 271, 272]. We focus on two cases: a) no dislocations initially present and b) $n$ prismatic dislocation loops with edges of length 20 nm and 21.2 nm (same shape as shown in Figure 45(a)) initially present. A comparison between these two cases has not been made before. For reference, when $n = 18$ the initial dislocation density is about $4.3 \times 10^{16}$ m$^{-2}$. This high initial dislocation density may be representative of a dislocation cell wall given the experimental observations of densities in excess of $10^{15}$ m$^{-2}$ locally in highly deformed aluminum [273, 279]. Figure 46 presents resulting stress-strain curves under a strain rate of $3 \times 10^{8}$ s$^{-1}$ with voids of initial radii $R_0 = 2.5$ and 10 nm, and a simulation box that is $L = 32.5$ nm on each edge. Figure 46(a) reproduces the same behavior as previous studies when dislocations are not initially present, with a large spike at yield, followed by a rapid drop in stress and subsequent softening. This initial spike corresponds to the nucleation of one or more dislocations from the surface of the void, which then enables plastic growth of the void. The new result shown here is the influence of pre-seeding the system with dislocations. We show that as the number of initial dislocation loops increases, the stress spike at yield is greatly reduced. This indicates that void growth occurs much more readily when dislocations are present, since void growth initiates at much lower stresses. Beyond initial yield, however, the stress-strain curves are independent of the number of dislocation loops.

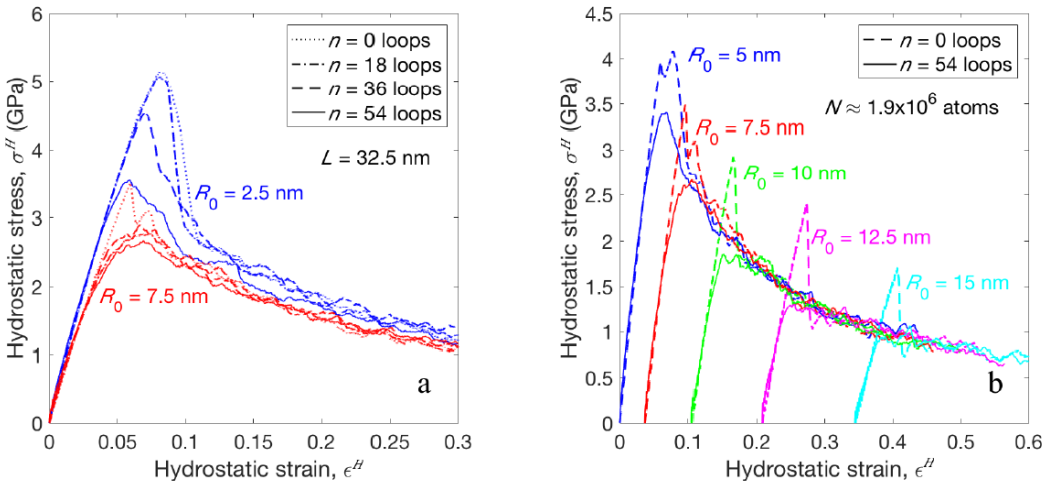


**Figure 46. Hydrostatic stress-strain curves under a constant hydrostatic strain rate of $3\times10^8$ $s^{-1}$. (a) Fixed box size of L = 32.5 nm, two different initial void radii, and different numbers of dislocation loops. (b) Box dimension varied to keep number of atoms approximately constant at 1.9 million with different initial void radii. Curves are shifted so that the void radius is approximately the same at the same strain.**

The observation that the post-yield behavior is insensitive to the initial dislocation content motivated additional simulations, where we increased the void radius while concurrently increasing the box dimensions so that the number of atoms was kept approximately constant at 1.9 million. In this way, all of the initial conditions can be related to each other and the influence of dislocations nucleated or initially introduced can be evaluated. For instance, at 10.5% strain the simulation with an initial void radius 5 nm has grown to an effective void radius of $R_{\text{eff}} = \left(\frac{3}{4\pi}\Delta V + R_0^3\right)^{1/3} = 10$ nm, where $\Delta V$ is the volume change of the cell. Hence, the simulation with initial void radius of 10 nm emulates the $R_0 = 5$ nm void case at 10.5% strain. We can then directly determine the influence that dislocations have at that strain by starting the simulation with and without dislocation loops introduced. Figure 46(b) presents the resulting stress-strain curves with and without dislocation loops, all translated along the x-axis so that the instantaneous void sizes match. Interestingly, beyond initial yield where a stress spike is observed in dislocation-free systems, all simulations collapse onto a single universal stress-strain curve. This fact indicates that post-yield, where the bulk of the void growth occurs, voids in simulations with and without dislocation loops grow by the same mechanism: dislocation adsorption. Specifically, under the influence of the void's stress field, dislocations multiply and adsorb at its surface. These results indicate that void growth does not occur by dislocation nucleation alone; void growth may be initiated by nucleation, but the growth itself occurs when the nucleated dislocations multiply and interact with the void's stress field. The finding that adsorption-mediated growth dominates even in dislocation-free systems is the second major contribution of this work.

These results provide details about the adsorption-mediated growth process, but do not provide a means for computing void growth rates akin to Eq. 10. To this end, we have computed void growth rates under a fixed tensile hydrostatic stress. By examining the volume history of the system we can estimate the void growth rate. Figure 47(a) shows the volume history expressed in terms of the effective void radius with a void of initial radius 5 nm under a stress of 2.8 GPa. Curves are shown for n = 0; 18, 36 and 54 dislocation loops. When no dislocation loops are present, no void growth is observed because the stress is insufficient to drive nucleation. As the number of loops increases, the

void growth rate increases. We can approximate the effective void growth rate $\dot{R}_{\text{eff}}$ using linear fits to these time histories. Figure 47(b) summarizes the results from 360 MD simulations; 20 random loop configurations for each value of n with hydrostatic stresses ranging from 2.3 to 2.8 GPa. Since void growth is highly sensitive to the specific dislocation configuration around the void, growth rates vary significantly for the same stress and number of loops (see Supplementary online material). Hence, in Figure 47(b) we plot the median growth rate among the 20 replicates at each set of conditions. To demonstrate that our results are not biased by the use of prismatic dislocation loops, we have also performed simulations using 12 shear loops, giving an initial dislocation density of $5.2\text{x}10^{16}$ $\text{m}^{-2}$ (see Supplementary online material). These results are also presented in Figure 47(b), showing more scatter but the same overall trend. Figure 47(b) demonstrates that the void growth rate increases with dislocation density and that the adsorption-mediated void growth rate is exponentially dependent on the hydrostatic stress. The latter result is significant because it is consistent with the experimentally validated Rice-Tracey relation. The fact that adsorption-mediated growth follows the same stress dependence as is observed in quasi-static experiments is the third major contribution of this work. Note that the same statement cannot be made about nucleation mediated growth. Analyzing the exponential curve fits further, we find that the growth rates with prismatic loops at all dislocation densities exhibit an exponent of about $4.4\sigma^H$, which according to Eq. 10 implies a "yield strength" of about 341 MPa; this is not an unreasonable order of magnitude for local stresses in highly work hardened aluminum which has been shown to exhibit a macroscopic ultimate strength as high as 250 MPa [280]. Hence, our results predict a growth rate of the form

$$\frac{\dot{R}}{R} = A(\rho)\exp\left(4.4\sigma^H\right) \tag{13}$$

where $A(\rho)$ is a dislocation-density-dependent prefactor.

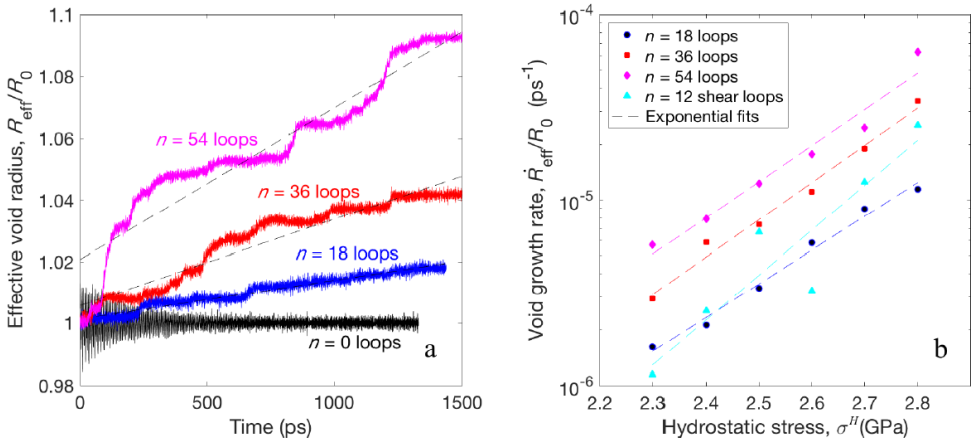


**Figure 47. Void growth rates under a constant hydrostatic stress $\sigma^H$ when $R_0$ = 5 nm and L = 32:5 nm. (a) Effective void radius as a function of time with $\sigma^H$ = 2.8 GPa. (b) Void growth rate as a function of hydrostatic stress. Dashed lines are exponential fits (Eq. 13).**

## 4.3. Discussion

The current work suggests that the dislocation-adsorption mechanism proposed by Chang et al. [213] can continue to operate at much higher dislocation densities, relevant to dislocation cell walls where voids are now understood to proliferate. Moreover, the current results suggest that the adsorption mechanism can account for extensive void growth, well beyond 0.1% indicated in the previous studies [213]. These current results, and the observed consistency with Rice-Tracey scaling, suggest that the adsorption mechanism is a more comprehensive explanation for void growth than previously indicated, strengthening the argument that dislocation emission is not a controlling factor. The fundamental dislocation processes involved in adsorption-mediated growth, glide and cross-slip of dislocations occur readily in experiments. Cross-slip is the slower of the two processes, however it has been shown that the energy barrier for cross-slip at free surfaces is extremely low (< 0.1 eV), making the cross-slip rate high [281]. While the dislocation densities considered here are necessarily on the upper end of the experimental range to enable void growth over atomistic timescales, lower densities would be sufficient to predict quasi-static growth rates. For example, if we extrapolate the void growth rate for n = 18 loops down to the ultimate strength of annealed aluminum, 108 MPa [280], we obtain a growth rate of $\dot{R}/R \approx 100\ \mathrm{s}^{-1}$, which leads to the void radius doubling in about 10 ms. Such a growth rate is much higher than is necessary for quasi-static conditions, where loading occurs over thousands of seconds. Finally, we note that recent experimental evidence showing that voids in pure Ta tend to nucleate at and grow along cell block boundaries formed by dense dislocation tangles [166] supports an adsorption-mediated mechanism. Combined together, the evidence presented here suggests an intimate, mechanistic linkage between void growth and strain-induced dislocation networks which may be influential to theories of ductile fracture

# 5. X-RAY COMPUTED TOMOGRAPHY ELUCIDATES COLLABORATIVE FAILURE MECHANISMS IN COPPER

The competition between ductile rupture mechanisms in high-purity Cu and other metals is sensitive to the material composition and loading conditions, and subtle changes in the metal purity can lead to failure either by void coalescence or Orowan Alternating Slip (OAS). In situ X-ray computed tomography tensile tests on 99.999% purity Cu wires have revealed that the rupture process involves a sequence of damage events including shear localization; growth of micron-sized voids; and coalescence of microvoids into a central cavity prior to the catastrophic enlargement of the coalesced void via OAS. This analysis has shown that failure occurs in a collaborative rather than strictly competitive manner. In particular, strain localization along the shear band enhanced void nucleation and drove the primary coalescence event, and the size of the resulting cavity and consumption of voids ensured a transition to the OAS mechanism rather than continued void coalescence. Additionally, the tomograms identified examples of void coalescence and OAS growth of individual voids at all stages of the failure process, suggesting that the transition between the different mechanisms was sensitive to local damage features, and could be swayed by collaboration with other damage mechanisms. The competition between the different damage mechanisms is discussed in context of the material composition, the local damage history, and collaboration between the mechanisms.

Keywords: Ductile fracture; Damage initiation; Void coalescence; Synchrotron radiation computed tomography

## 5.1. Introduction

The ductile fracture of engineering metals and their alloys involves the competition between several damage mechanisms, including void nucleation, growth and coalescence into a crack; catastrophic shear along one or more planes; necking to a point; or growth of a central prismatic void by Orowan alternating slip (OAS)[32, 33, 56, 65, 282, 283]. The competition between these different mechanisms is poorly understood, and small variation in the material microstructure or stress state can lead to very different failure processes (Figure 48a). For instance, tensile testing of Cu wires (Figure 48b-c) produced a fully-dimpled fracture surface indicative of failure by void coalescence in 99.9% purity Cu, but a largely void-free failure surface formed by OAS in 99.999% purity Cu [165]; on the other hand, plane-strain tension of both 99.9% and 99.94% Cu sheets resulted in failure by OAS [63, 165]. In this manuscript, we seek to elucidate the divergence in failure mechanisms between OAS and void coalescence using in situ X-ray Computed Tomography (XCT). Currently, very little is known about the mechanics of OAS, how it interacts with other damage mechanisms, and the circumstances when it is favored over failure by void coalescence. An exhaustive literature search has identified only three systematic ex situ studies of the OAS mechanisms for oxygen-free high-conductivity Cu (99.94%) [63], AA 5754 [17], and 99.9% Ni and 99.999% Cu [165], as well as possible instances of OAS-dominated failure in Al (99.5%) [284] and brass [285].

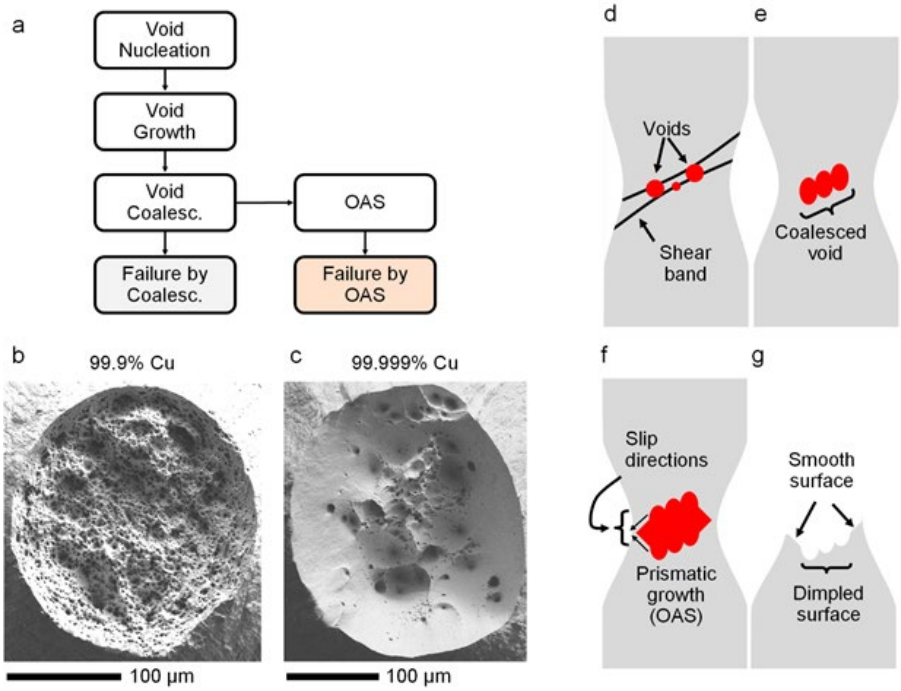


**Figure 48. Active damage mechanisms in high-purity Cu. (a) Composition-regulated divergence in damage mechanisms from failure by void coalescence to failure by OAS. (b) Secondary electron image of fracture surface of 99.9% Cu wire (unpublished). (d) Secondary electron fracture surface of 99.999% Cu wire. (d-g) Postulated sequence of damage mechanisms in 99.999% Cu involving (d) Void nucleation and shear band formation, (e) Void coalescence into a central cavity, (f) Prismatic cavity growth by OAS, and (g) Fracture surface.**

In the absence of *in* situ damage measurements, there remains considerable ambiguity regarding the fundamental relationship between OAS and void coalescence, which is essential to explaining the divergence in failure mechanisms observed in Figure 48b-c. The experiments in Ref. [165] suggested

that failure by OAS was actually preceded by extensive void coalescence, and OAS may have been facilitated by the preceding damage mechanisms. For example, OAS void growth in AA 5754, AA 1100, and >99.9% pure Cu was preceded by the propagation of one or more shear bands through the center of the neck, and also the coalescence of voids to form an adequately large cavity to enable OAS growth [17, 63, 165, 284, 285]. We hypothesize that the collaborative interaction between these damage mechanisms can promote the transition to failure by OAS rather than continued void coalescence.

The unique capabilities of *in situ* synchrotron XCT enables systematic study of these interactions by tracking the appearance, growth, motion and arrangement of micron-sized voids throughout the deformation history. In contrast, conclusions drawn from the previously reported interrupted mechanical testing experiments are convoluted by differences in microstructure and damage between specimens, and may not capture rare damage events. In similar studies on alloyed materials, *in situ* XCT experiments have provided essential insight into the ductile failure of aluminum [54, 286], steel [287], titanium [288] and cast iron [289], as well as model systems containing brittle secondary particles [290] or pre-fabricated holes [78, 79, 286, 291]. There exist limited 3D studies on the damage behavior in pure metals (for instance, on commercially-pure Mg [148] and Ti [292]), and consequently the damage mechanisms other than void growth and coalescence are poorly studied.

With *in situ* XCT measurements, we seek to answer several key questions about the competition between failure by coalescence and failure by OAS. First, what is the relationship between OAS and the preceding damage mechanisms, including shear localization, void growth and coalescence? Second, under what conditions is OAS favored over continued void coalescence? In particular, it is unknown if there exists a well-defined transition between these mechanisms, or if certain damage configurations locally favor OAS over coalescence. The fracture surfaces of OAS-susceptible materials all exhibit dimpled morphology near the center of the sample, indicating that widespread void growth and coalescence occurs prior to the transition to the OAS mechanism, but ceases in later stages of failure [17, 63, 165, 284, 285]. On the other hand, why does OAS growth not commence after the initiation of the first void?

Answers to these questions are pursued through *in situ* XCT tensile testing of Cu wires, which are described in the next section. The key damage mechanisms and their interactions are revealed in the tomograms, which are qualitatively analyzed in Section 3. Section 4 presents quantitative measurements of the voids, which are used to demarcate and understand the transitions in damage mechanisms. Finally, the origins of the OAS failure process are discussed in Section 5.

## 5.2. Materials and Methods

High-purity Cu wires were tested in tension using *in situ* XCT to study the internal damage mechanisms prior to ductile rupture. All experiments used 99.999% high-purity Cu wires (ESPI Metals) with nominal diameters of 0.75 mm or 1.00 mm. Both types of wires were fully dense, but contained tightly-bound inclusions of diameter 500 nm [165]; inspection by energy-dispersive X-ray spectroscopy (EDS) found that these particles to have a composition of CuO2.

This paper primarily reports on interrupted *in situ* XCT tensile testing experiments performed at Beamline 2-BM-A at the Advanced Photon Source at Argonne National Laboratory. The wires were tested under quasistatic conditions to failure in a Deben CT5000 load frame which recorded both load and displacement of the specimen; deformation was applied at a nominal strain rate of $1 \times 10^{-3}\ s^{-1}$ based on the grip displacement and a gage length section of 10 mm. During the *in situ* experiments, the deformation of the specimen was paused for tomographic acquisition at prescribed levels of

remaining strength. The load relaxed during imaging by about 10% in this time, but recovered fully upon subsequent loading (Figure 49a). Each tomogram was reconstructed from 1500 equally-spaced radiographs with 50 ms exposure over 180° rotation using 35 keV beam energy, resulting of reconstructions of size 2560 × 2560 × 2130 voxels and a voxel size of 0.65 µm. All tomograms were reconstructed with TomoPy using the gridrec algorithm [293]. Three specimens of each wire diameter were tested using the interrupted in situ XCT technique, which were labeled as 0.75mm-A, B & C, and 1mm-A, B & C.

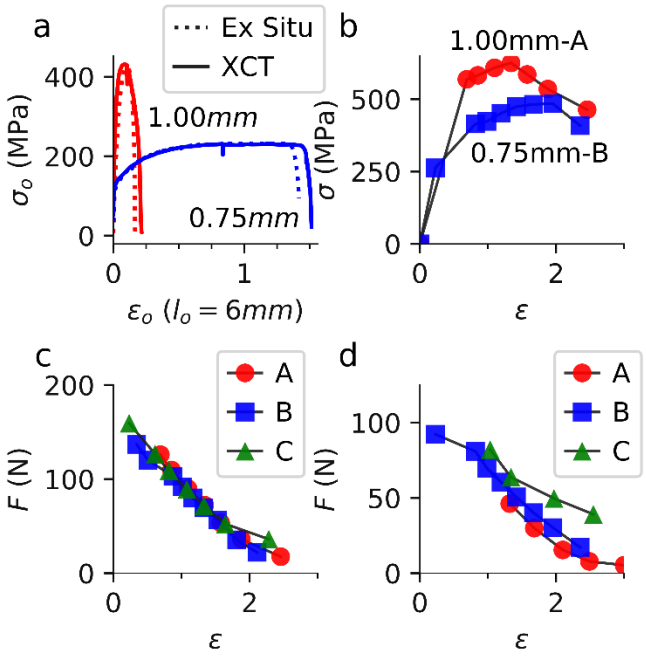


**Figure 49. Mechanical behavior of high-purity Cu wires. (a) Representative in situ and ex situ engineering stress-strain curve for the two sizes of Cu wires, showing differences in strength and ductility. (b) True stress-strain curves for the same in situ experiments. (c-d) In situ load vs. true strain relationships after necking in the (c) 1 mm and (d) 0.75 mm wires. True strain in (b-d) is derived from the XCT-measured cross-sectional area.**

Due to limited resolution, the tomograms only captured voids larger than $\sim 2\ \mu m^3$, such that this experiment focused on the later stages of void growth and subsequent damage mechanisms. Early stages of damage associated with void nucleation and initial void growth were inaccessible.

Additional interrupted, ex situ tensile tests were performed on additional 1 mm diameter wires to investigate the effects of intermittent deformation on the damage mechanisms [294], which showed similar engineering stress-strain response to the *in situ* experiments (Figure 49a). These specimens were deformed continuously until the load dropped to 70%, 60%, 50%, and 40% of UTS as well as after fracture (0% UTS), where % of UTS is defined as the remaining fraction of ultimate tensile strength after necking. These specimens were subsequently scanned using a laboratory micro-XCT machine (XRadia microXCT-200) with 1.48 µm voxel size. The source voltage and current were 80 keV and 100 µA, respectively, and imaging was performed using a 10x magnification detector. As will be shown later, damage in these specimens initiated at identical strain and exhibited similar void quantity, spacing and growth characteristics, suggesting that the interrupted *in situ* loading scheme did not affect the damage mechanisms.

Finally, all tomograms were cropped, denoised using Gaussian filters, and thresholded using custom Python scripts, producing binary images that identified the location and geometry of voids formed within the Cu wires. The individual voids were subsequently labeled, analyzed and rendered using Avizo 9.0 software (FEI Visualization Sciences Group). After segmentation, the position and geometry of all voids were measured using Avizo. The data were analyzed to measure the void quantity, median void size (as defined by the equivalent spherical radius), and the median void spacing (as defined by the distance from each void centroid to the closest neighboring void centroid).

All quantitative void measurements are presented as a function of true strain, which was determined from the instantaneous reduction in area at the center of the neck, $\varepsilon = \ln(A_0/A)$. The instantaneous area was determined from the area enclosed by the necked wire surface; that is, internal porosity did not contribute to the area calculation. The true stress was calculating by dividing the instantaneous load by the minimum cross-sectional area (Figure 49b). The 1 mm and 0.75 mm wires showed ultimate strengths of ~625 and 475 MPa, respectively, although the accuracy of the stress measurement was hindered by the low loads after necking and small cross-sectional areas at large deformations. However, the load vs. true strain curves after necking showed exceptional consistency between samples (Figure 49c-d), indicating that the failure of the wires was not affected by defects or geometrical imperfections.

To aid in the identification of the damage mechanisms, fracture surfaces of the wire specimens were imaged using scanning electron microscopy (FEI Quanta 650) in secondary electron imaging mode.

## 5.3. Overview of damage and deformation mechanisms

As identified in Figure 50, the copper specimens exhibited complex deformation and damage behavior prior to final fracture. In the 1 mm specimens (Figure 50a-d), micron-sized voids were detected exclusively near the center of the neck and began to grow. Near simultaneously, a visible shear band appeared in the sample, which formed step-like features on the surface where the plane of localization intersected the exterior surface (marked by arrows in Figure 50) and caused prominent shearing between the top and bottom halves of the specimens. The development of a shear band in the axisymmetric wire samples was remarkable [295], and could be related to the nucleation of submicron voids in pure metals that were not visible via XCT [166] or plasticity-induced anisotropy [296]. Similar shear bands were observed in 99.94% Cu and AA 5754 sheet specimens [17, 63], as confirmed by measurements of the distortion of the grain structure. The appearance of the shear band had significant implications for the damage evolution of Cu, as discussed later in this section.

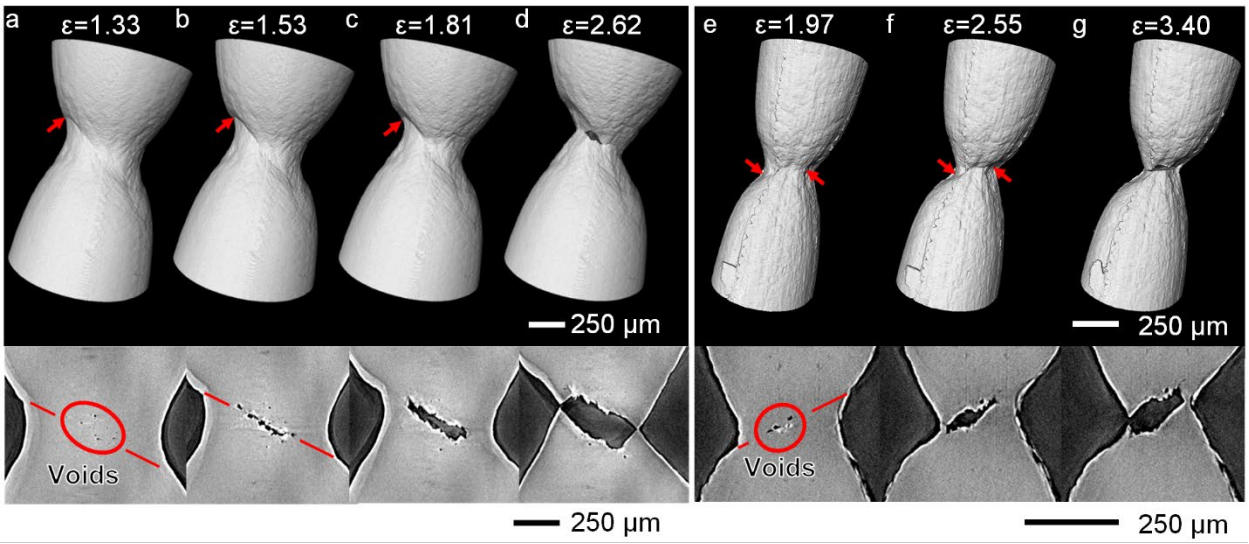


**Figure 50. Deformation and damage mechanisms in Cu wires for (a-d) large Cu specimen 1mm-B, and (e-g) small Cu specimen 0.75mm-C. Top panel shows 3D view of wires during *in situ* testing, while bottom panels show representative XCT cross-sections. The plane of shear localization is marked by arrows in 3D renderings, and by lines in 2D slices. OAS growth of the central cavity is evident in panels (c), (d), (f) and (g).**

After continued deformation and void growth, void coalescence occurred along this shear plane, resulting in a large cavity that grew by the OAS mechanism. This cavity enlarged until it breached the exterior surface, resulting in failure. No voids were observed near the wire's exterior surface ahead of the growing OAS void, suggesting that this cavity grew without creating adjacent voids. This observation was consistent with the nature of the OAS mechanism as described by Orowan and other experiments [17, 56, 63, 165].

Similar deformation mechanisms were also observed in the 0.75 mm copper wires (Figure 50e-g), although the void coalescence and OAS mechanisms appeared to activate at larger strain and after the initiation of fewer voids. For instance, void coalescence along the shear band in this specimen began at $\varepsilon = 1.97$ in the smaller specimen in Figure 50e, compared to $\varepsilon = 1.53$ in the larger specimen in Figure 50a. Thus, both specimen types displayed similar damage sequences despite their different strength and ductility.

It was clear that the void growth, coalescence and OAS damage mechanisms were intimately affected by the shear localization. First, the first micron-sized voids appeared exclusively in material near the shear band (marked by red lines in Figure 50a,b,e). Inspection of the tomograms showed that the maximum distance between voids and the shear plane was $150\ \mu m$. Second, the main coalescence event occurred along the shear band. Subsequent growth of the cavity by OAS continued to utilize the shear band after coalescence, which formed one set of the facets on the enlarged void.

Analysis of the fracture surfaces via XCT and SEM confirmed the complex sequence of damage mechanisms in the Cu wires (Figure 51). The damage evolution in the smaller specimens was qualitatively similar (albeit with fewer voids), and is not discussed further in this section; quantitative damage metrics are presented for both types of specimens later in Section 5.4. Both the XCT tomograms and SEM images identified an internal region on the fracture surface that was marked by a rough, dimpled surface, as well as an external region marked by a smooth, largely dimple-free surface

(Figure 51a,b). This morphology closely matched the fracture surfaces observed in other materials that failed by OAS [17, 63, 165].

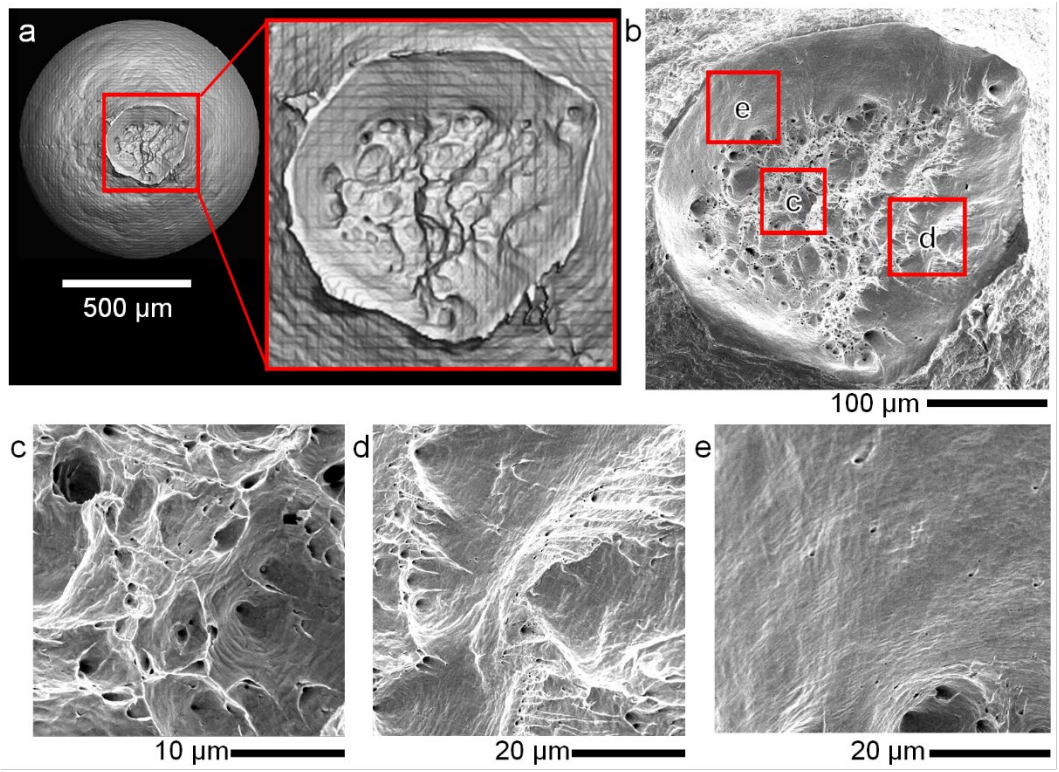


**Figure 51. Comparison of fracture surfaces via XCT and SEM for specimen 1mm-A. (a) XCT rendering of fracture surface, (b) secondary electron image of fracture surface, and (c-e) detailed images of (c) central region showing intervoid necking, (d) transition region showing intervoid shearing, and (e) external region showing smooth, void-free surface.**

However, closer investigation by SEM revealed several key features that were not captured by XCT. First, the interior region contained a range of void sizes, including several larger ~10 µm dimples as well as many smaller ~1 µm dimples (Figure 51c). The origin of the voids that formed these dimples is beyond the scope of this work, but it has recently reported that many voids can nucleate at dislocation cell and cell block boundaries in the absence of secondary phases in pure metals such as tantalum [166]. CuO2 particles were observed in a small fraction of the larger dimples.

The surfaces of the larger dimples showed a rough, orange-peel texture; these features have previously been attributed to the alternating slip behavior in OAS [63] and imply a degree of self-similarity between void growth and the OAS mechanism. The fracture surfaces also contained many shear-type dimples in the transitory zone between the internal, dimpled region and the external, smooth region (Figure 51d). The XCT resolution was inadequate to detect the smaller voids as well as the dimples formed by intervoid shearing. Very few voids were observed in the exterior region of the fracture surface (Figure 51e), suggesting void-free damage in the final phases of rupture.

The formation of these fracture surfaces can be related to the 3D damage history, which is presented in Figure 49 for two of the 1 mm diameter wires. In the earliest stages of damage, voids appeared and grew uniformly near the neck center (visible in Figure 49a,e). While this cluster of voids initially showed no preferred orientation, subsequent load steps revealed an ellipsoidal void-containing region

that was elongated along the primary shear plane. In subsequent load steps, void coalescence near the shear plane led to the development of a primary cavity that grew by the OAS mechanism. The resulting cavity bisected the cluster of voids, with roughly equal numbers of voids above and below the plane of coalescence (Figure 49b,f).

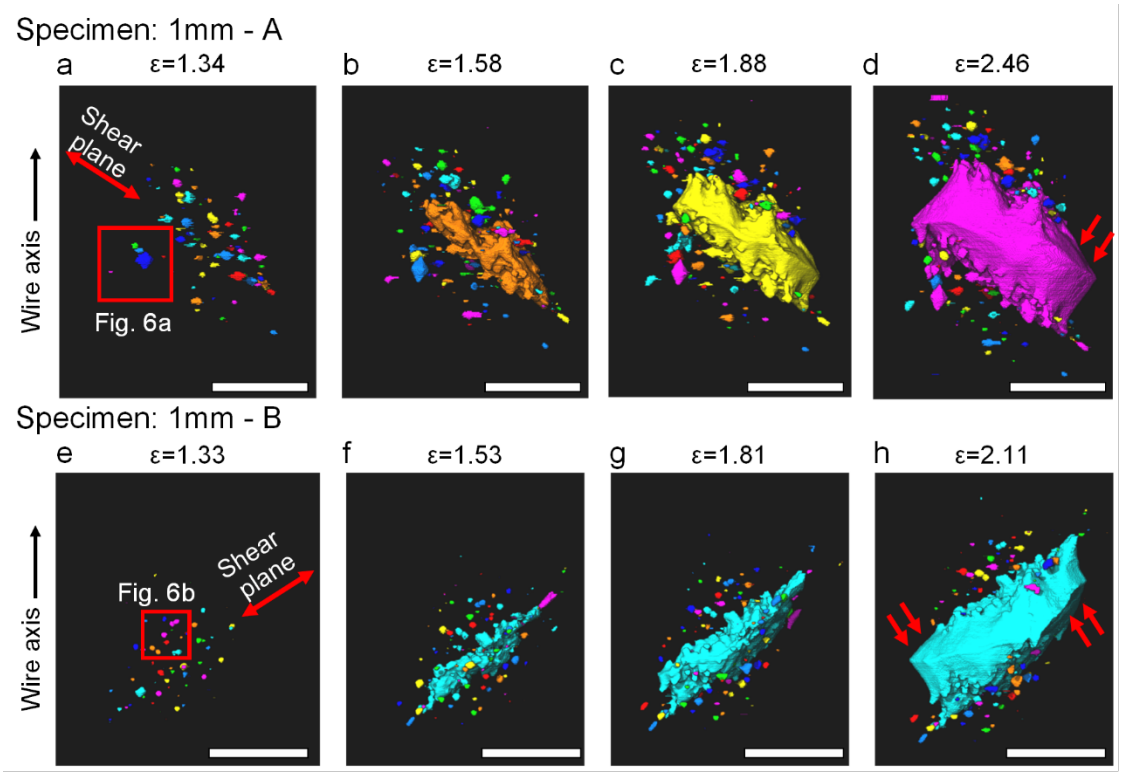


**Figure 52. 3D overview of damage in two separate large-diameter specimens. Smooth, dimple-free surfaces that are parallel to the shear plane are marked in (d, h). Void coloring for each image is arbitrary. Scale bar: 125 μm.**

After coalescence, almost all damage was associated with OAS growth of the main cavity, which marked a transition from the previously dominant damage mechanisms of void growth and coalescence. Growth of the primary cavity along shear planes that intersected the equatorial vertex of the coalesced void (*i.e.,* the OAS mechanism) formed a characteristic prismatic void with smooth, faceted surfaces. These smooth surfaces stood in contrast to the rough, dimpled features that formed initially during void coalescence, and some of these surfaces were parallel to the original shear plane (arrows in Figure 49d,h). The self-similar growth of the OAS cavity contrasted with the void shape that would be formed by an internal necking process, which would create a rounded void profile.

Qualitatively, the shape, size and number of the secondary voids on either side of the coalesced cavity remained approximately unchanged in the final loading increments; quantitative analysis to this effect is presented later in Section 5.4. This could be explained by elastic unloading around the main cavity, as identified in numerical models of the OAS process in Ref. [63].

Close analysis of the tomograms revealed a nuanced competition between the damage mechanisms, such that the behavior of individual voids sometimes contradicted the globally prevailing damage mode (Figure 53). First, several isolated voids enlarged by the OAS mechanism prior to the main

coalescence event (Figure 53a), which was notable because OAS growth of the primary cavity did not occur until after coalescence. The activity of OAS in these voids was confirmed by the 3D prismatic shape of the void without any interaction with adjacent voids; similar void shapes have previously been observed in axisymmetric metal matrix composites [77]. An initially spherical void grew and acquired faceted surfaces by $\varepsilon = 1.58$; the void size and shape remained approximately constant thereafter. Several other faceted voids can be identified in the other two large specimens, which also did not link up with the final void.

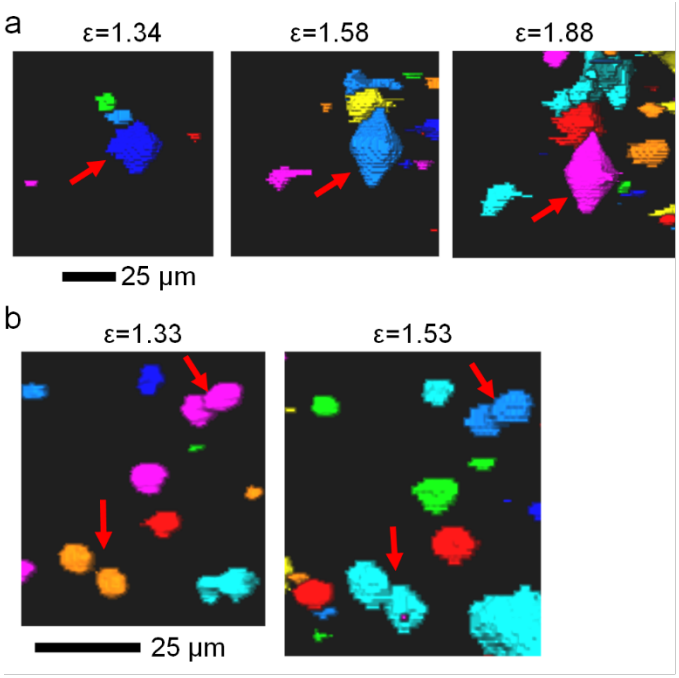


**Figure 53. 3D overview of damage in two separate large-diameter specimens. Smooth, dimple-free surfaces that are parallel to the shear plane are marked in (d, h). Void coloring for each image is arbitrary. Scale bar: 125 µm.**

Second, several pairs of voids grew and coalesced independent of the main coalescence event (Figure 53b). These voids were located approximately 50-75 µm from the plane of shear localization, and thus experienced a slightly different stress triaxiality compared to voids closer to the shear plane. Compared to the general void population, the pairs of voids that coalesced were located particularly close to each other, thus facilitating coalescence.

## 5.4. Quantitative damage measurements

The count, spacing and size of voids in the three 1 mm diameter wire specimens are quantified in Figure 54, and also for the three 0.75 mm specimens in Figure 55. By highlighting a limited window in which void nucleation and growth occurred, these measurements showed that damage occurred by a different mechanism in 99.999% Cu than in a lower-purity material that would fail by void coalescence. We emphasize that the smallest detectable void was limited by the spatial resolution of $0.65\ \mu m$, such that the minimum measured size was approximately $2\ \mu m^3$. Accordingly, the XCT measurements captured the smallest voids after an extensive period of void growth, rather than immediately after nucleation.

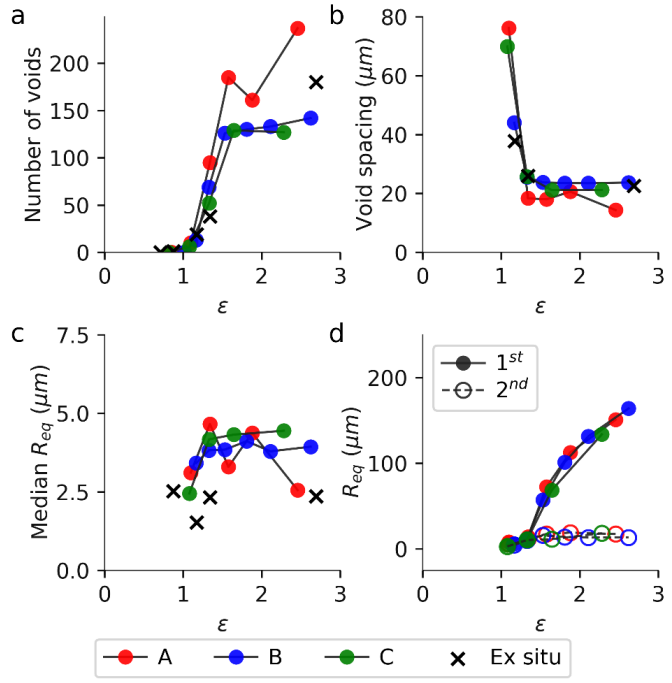


**Figure 54. Quantitative void measurements for the 1 mm diameter specimens. (a) Void count, (b) Median void spacing, (c) Median equivalent spherical radius, and (d) size of two largest voids at each load increment. Specimens A, B and C were tested in situ, while "×" denotes data from separate ex situ specimens.**

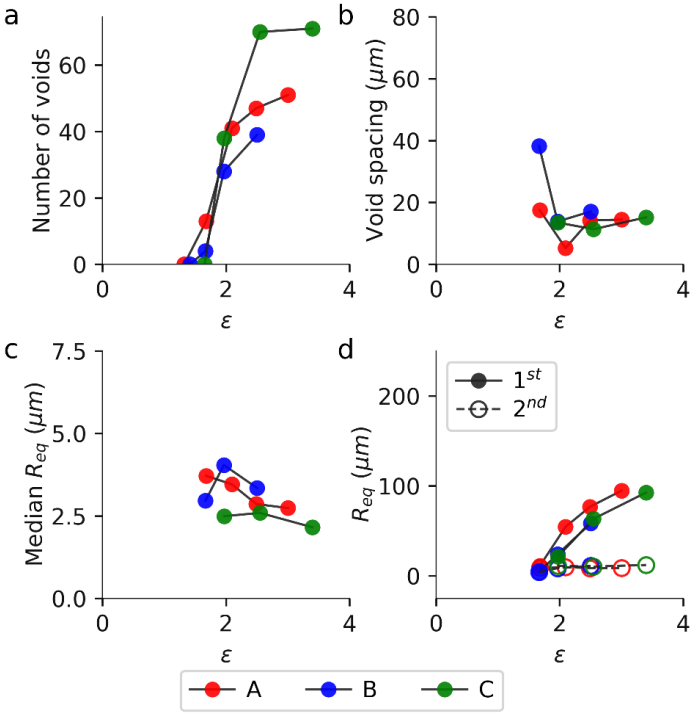


**Figure 55. Quantitative void measurements for the 0.75 mm diameter specimens. (a) Void count, (b) Median void spacing, (c) Median equivalent spherical radius, and (d) size of two largest voids at each load increment.**

The Cu wires exhibited unusual void growth characteristics, as indicated by the number of micron-sized voids observed in the wire as a function of deformation (Figure 54a and Figure 55a). Within the large-diameter specimens, the first voids were detected at a true strain $\varepsilon = 1.1$ and the number of voids rapidly increased to between 125 and 180 by $\varepsilon = 1.6$. Similarly, in the small-diameter specimens, the first voids appeared at $\varepsilon = 1.6$, and a maximum void count of 40-70 voids was achieved by $\varepsilon = 2.1$. Beyond this range of deformation, the number of voids remained essentially constant; by comparison to the 3D void renderings in Figure 49Figure 49. 3D overview of damage in two separate large-diameter specimens. Smooth, dimple-free surfaces that are parallel to the shear plane are marked in (d, h). Void coloring for each image is arbitrary. Scale bar: 125 μm., the detection of additional voids ceased with the main void coalescence event. As an approximate measure of the void density, the void counts for the two specimen sizes were reasonably similar after normalizing by the ratio of the two wire diameters ($\left(\frac{1\ mm}{0.75\ mm}\right)^3 = 2.37$); this ratio reflected the different neck sizes as visible in above, as the neck height and diameter scaled with the wire size. Thus, the damage trends in the smaller specimens were similar, even though they occurred at slightly higher strain.

Intriguingly, the median void spacing converged prior to the main coalescence event (Figure 54b and Figure 55b). For the large diameter specimens, void spacing rapidly decreased from an initially large spacing to a median value of $17 - 25\ \mu m$ at $\varepsilon = 1.3$. For the smaller specimens, the void spacing stabilized at $15\ \mu m$ by $\varepsilon = 2.1$. In other words, the size of void-containing material at the center of the neck continued to enlarge prior to coalescence.

The Cu wires exhibited unusual void growth kinetics, as summarized in Figure 54c-d and Figure 55c-d. Despite the visual observations of void growth in Figure 49, the median void size remained approximately constant at $3$ to $4\ \mu m$ throughout the specimen deformation for both sizes of specimens (Figure 54c and Figure 55c). Taken in conjunction with the void quantity measurements in Figure 54a and Figure 55a, this implied that the growth of existing voids was offset by the detection of additional smaller voids. Further analysis of the two largest voids in the specimens (Figure 54d and Figure 55d) indeed showed that the voids grew throughout the experiment, although growth was heterogeneous. Prior to coalescence, the size of the 1st and 2nd largest voids in the large wires were similar, and increased from $R_{eq} \approx 5\ \mu m$ at $\varepsilon = 1.1$ to $R_{eq} \approx 10\ \mu m$ at $\varepsilon = 1.3$. However, growth of the voids diverged after coalescence: the size of the largest void increased to $R_{eq} > 100\ \mu m$ while the second largest void grew only to $R_{eq} \approx 17\ \mu m$ by failure at $\varepsilon = 2.5$. Similar trends were observed in the small wires.

Finally, quantitative void measurements from the ex situ experiments were compared to the results from the in situ measurements. Damage occurred at similar strain in the ex situ measurements, and showed similar trends in the void quantity and spacing. The ex situ void size measurements were characteristically smaller than the in situ measurements. This was attributed to the lower XCT resolution used in the ex situ measurements ($1.48\ \mu m$ vs. $0.65\ \mu m$), which would prevent accurate measurement of the void volumes [297].

## 5.5. Discussion

### *5.5.1. Evolution of damage in Cu wires*

The *in situ* XCT tensile experiments have provided a full history of the deformation and damage in high-purity Cu for the first time, thereby revealing the collaborative nature of damage in this material.

This study has clarified the sequence of deformation and damage events compared to previous studies that relied on *ex situ* microscopy. Both sizes of Cu wires showed necking, void nucleation, and shear band formation prior to the detection of micron-sized voids, then subsequent void growth, void coalescence, and finally prismatic cavity growth by the OAS mechanism. This finding clearly refuted earlier work in Ref. [63] that assumed that the OAS mechanism activated spontaneously upon the appearance of a single void at the center of the necked region.

### 5.5.2. Collaborative interactions between damage mechanisms

The primary finding is that the transition toward OAS is influenced by collaborative interactions with other damage mechanisms. That is, the OAS mechanism did not activate spontaneously but appeared to be enabled by previous damage events.

The first prominent interaction was between the shear band and subsequent void growth and coalescence. The appearance, growth and coalescence of voids appeared to be strongly coupled to the shear band. This shear localization further magnified the strain at the center of the neck, and facilitated the rapid growth of more micron-sized voids. As shown in Figure 49, the cluster of voids immediately prior to void coalescence was not isotropic, but was ellipsoidal with the major axis aligned with the shear band, and all micron-sized voids were confined to this region. Still, many of the voids appeared at a distance up to 150 μm from the shear band, which was significantly larger than the observed shear band width of ~50 μm in previous works [63, 165]: this indicated that the shear band enhanced void growth but was not necessary for their formation. As a consequence of the localized deformation and the spatial distribution of voids, the main coalescence event occurred within the shear band.

The primary coalescence event precipitated the activation of OAS in the damaged Cu wires. This had several favorable effects on the OAS mechanism. First, the coalescence event reduced the distance between the cavity and wire surface, which altered the stress state to approximately plane strain and may have facilitated the conjugate slip necessary for OAS growth. Second, the coalescence event consumed all micron-sized voids on the shear plane, which inhibited subsequent coalescence events.

Finally, the OAS growth of the central cavity utilized the initial shear band to satisfy one of the alternating slip planes (Figure 49d,h). This resulted in faceted surfaces that were parallel to the shear band, and confirmed the interaction between the shear band and OAS mechanism.

### 5.5.3. Local divergence in failure mechanisms

In addition to the clear transitions between isolated void growth, void coalescence, and OAS as the dominant global damage mechanisms, the tomograms also identified instances of void coalescence and OAS that occurred at different stages of the damage process. Together, they provide evidence that the divergence from void coalescence to OAS was local in nature, and was sensitive to the local deformation, stress state and damage history.

What enabled the transition towards OAS growth of the main cavity, rather than continued void nucleation and coalescence in front of the sharp notch? Based on evidence provided by these experiments as well as those in the literature, it is postulated that the relative activity of these mechanisms in high-purity Cu depends locally on the void size and spacing between voids. In this framework, evolution in the geometry and spacing of voids throughout the failure process can trigger the transition in damage modes. This approach also explains the divergent failure behavior of 99.9% Cu and 99.999% Cu (Figure 48).

OAS is favored for larger voids. For example, the prismatic void in Figure 53a was the 1st largest voids observed at $\varepsilon = 1.34$ prior to the development of faceted surfaces. After the main coalescence event, the resulting cavities in the center of each wire had diameters of ~250 μm; these cavities grew rapidly by OAS until they breached the wire surface. SEM fractography identified very few dimples on the fracture surface formed by the OAS process, indicating that the cavity grew without the formation or consumption of additional voids. This also agreed with other examples found in the literature. Similarly, in a metal matrix composite with ~50 μm ceramic particles embedded in 99.9% Al matrix, the cavities produced by delamination of the particles first "tunneled" through the matrix to connect adjacent particles to form a cylindrical cavity with a diameter of ~100 μm, but subsequently grew in a manner resembling OAS [77]. While these findings are based on qualitative judgement of the void geometry, and are biased by the challenge of identifying faceted shapes in smaller cavities, this analysis implies that OAS growth of large cavities occurs much faster than voids can grow and coalesce in adjacent material.

In contrast, intervoid coalescence dominates the failure of materials with closely-spaced voids, which is captured by the dependence of well-known coalescence models on the intervoid spacing [37, 267]. Plausibly, the early coalescence predicted for small intervoid spacing would prevent the growth of voids into the size necessary for OAS to dominate. Experimentally, this manifested in failure by generalized void growth and coalescence in low-purity Cu materials [2, 39, 85, 298] such as 99.9% pure Cu (Figure 48), and also coalescence in the current experiment near the center of the neck where the density of voids was highest. The current experiments also revealed isolated examples of intervoid necking between proximate voids (Figure 53b), showing that the balance between these different mechanisms was local in nature. Similarly, in a study of AA 5754 with different levels of iron content, Spencer found that while both the low-iron and high-iron materials developed prismatic OAS cavities, failure in the high-iron material occurred by coalescence of voids in shear bands that intersected the OAS cavity [17]; this behavior was attributed to the decreased spacing between voids formed at micron-sized $FeAl_6$ intermetallic particles in the metal. Thus, OAS is not the favored failure mechanism in materials with high void density.

## 5.6. Conclusions

*In situ* XCT tensile testing of high-purity Cu wires revealed a complex and collaborative sequence of damage mechanisms that culminated in ductile rupture. In situ XCT testing tracked the evolution of micron-sized voids throughout the deformation process, and showed that the dominant damage mechanism in the Cu wires transitioned from shear localization, to the growth of micron-sized voids, to void coalescence, and finally to prismatic growth of the coalesced cavity by Orowan Alternating Slip (OAS). These measurements provided strong evidence of collaboration between different damage mechanisms. Specifically, localized deformation along the shear band drove the nucleation and growth of voids, and contributed to coalescence along the shear band rather than transverse to the axial load. These interactions must be incorporated into damage models to accurately predict component failure.

Despite these trends, the damage mechanisms in high-purity Cu appeared to be strongly influenced by the local size and arrangement of voids, such that the evolving stress and damage states could activate the transition to a different damage mechanism. This resulted in several isolated instances of OAS and coalescence that were contrary to the globally prevailing damage mode. Analysis of the scenarios in which OAS and intervoid coalescence were active suggested that OAS was favored for large, isolated voids, and that coalescence was favored for smaller, closely-spaced voids. This implied that small variations in local microstructure, loading conditions or damage history could substantially

alter the ductile rupture process, and could explain the different failure modes of high-purity Cu due to changes in composition, stress state and geometry.

# 6. ROLE OF DYNAMIC RECRYSTALLIZATION ON RUPTURE IN ALUMINUM

The process of ductile fracture in metals often begins with void nucleation at second-phase particles and inclusions. Previous studies of rupture in high-purity face-centered-cubic (FCC) metals, primarily aluminum (Al), concluded that 2nd-phase particles are necessary for cavitation. A recent study of Ta, a body-centered-cubic (BCC) metal, demonstrated that voids nucleate readily at deformation-induced dislocation boundaries. These same features form in Al during plastic deformation. This study investigates why void nucleation was not previously observed at these dislocation boundaries in Al. We demonstrate that void nucleation is impeded in Al by room-temperature dynamic recrystallization (DRX), which erases these boundaries before voids can nucleate at them. If dislocation cells reform after DRX and before specimen separation by necking, voids nucleation is observed. These results indicate that defect/defect interactions can create void-nucleation sites in inclusion-free FCC materials that deform by slip.

## 6.1. Introduction

Before 1950, the question of how and where voids nucleate during ductile rupture was hotly debated. Several researchers proposed that voids nucleated at the head of blocked slip bands by a cleavage-like mechanism [3, 140], while others hypothesized that voids formed by dislocation reactions [73, 299, 300]. The invention of the scanning electron microscope enabled the discovery by Tipper and others [2, 72] that voids nucleate at second-phase particles. Based on this discovery, Cottrell hypothesized that "if such particles were not present, the specimen would pull apart entirely by the inward growth of the external neck, giving nearly 100% reduction in area" [73]. Several critical experiments on high-purity face-centered-cubic (FCC) metals, primarily aluminum (Al), strongly supported this conclusion [2, 22, 56, 57, 95, 96]. For example, using aluminum, Chin *et al.* [22] observed that the dimple density on the fracture surface decreased with increasing sample purity. In the extreme case, zone-refined (approximately 99.999% Al) aluminum failed by necking to a chisel point rather than by cavitation [22]. Similar trends were reported in high-purity lead (Pb) [57], though the resolution of the characterization techniques used in both studies was likely insufficient to detect voids smaller than 10 μm. These results led to the conclusion that generalized void nucleation does not occur in bulk, particle-free FCC metals that deform by slip [63, 98, 301] except, perhaps, when supersaturated hydrogen creates micropores during processing [302].

In contrast, Boyce *et al.* [101] observed that high-purity tantalum (Ta), a body-centered-cubic (BCC) metal, failed in a ductile manner by void nucleation, growth, and coalescence. No second-phase particles or inclusions were observed in this material. Subsequent analysis showed that voids in Ta nucleated at deformation-induced dislocation boundaries, *i.e.* dislocation cell walls and cell block boundaries [71]. Similar grain subdivision into groups of dislocation cells, separated from each other by lamellar cell block boundaries, occurs universally in wavy glide materials, including Al, during plastic deformation [16, 76, 102, 106, 107, 111, 303]. In general, dislocation cell walls are primarily formed of statistically stored dislocations [304] and are low angle (<1°) boundaries; cell block boundaries contain many geometrically necessary dislocations [304] and generally accommodate misorientations greater than 2° [16, 76]. The observations that voids nucleate at these boundaries in Ta raises an important question: why is void nucleation at dislocation boundaries suppressed in Al and, by extension, other FCC metals? It is possible that the relative ease of slip in FCC metals compared to BCC metals suppresses void nucleation at dislocation boundaries. However, the recent observation that the dimple-density on the fracture surface of high-purity Al specimens depended on grain size [165] suggests that other factors may also influence void nucleation in FCC metals. Furthermore, TEM

analysis of high-purity, thin-film, single-crystalline samples of beryllium (Be), iron (Fe), and gold (Ag) by Wilsdorf and coworkers [13, 90, 97, 160, 161, 162, 163] suggests that voids in each of these materials nucleate at dislocation boundaries during ductile fracture.

The present study thus reexamines void nucleation in bulk, polycrystalline, particle-free FCC metals. Al was chosen as the model material because of the extensive use of this material in early studies of void nucleation in particle-free materials. The following questions are addressed in this study:

1. Are there conditions under which voids nucleate in particle-free Al? If so, where do these voids nucleate?
2. What are there mechanism(s) that suppress void nucleation in particle-free Al?

The groundwork for a detailed study on void nucleation was laid by first examining the relationship between microstructure, purity, and void nucleation in three Al wire materials of different purities. These experiments informed a subsequent examination of damage progression in a high-purity Al sheet material. Dynamic recrystallization (DRX) was observed in three of these materials, consistent with previous studies of heavily-deformed, high-purity Al [305, 306, 307, 308, 309]. The effects of this on void nucleation were examined in this study, though a detailed study of DRX in these materials was not performed.

## 6.2. Materials and Methods

To observe the relationship between purity and void nucleation, an initial series of tests were performed on Al wire materials having nominal purities between 99.9% and 99.999% Al. Based on the groundwork laid by these experiments, a more detailed investigation was subsequently performed on an Al sheet material having a nominal purity of 99.99% Al. All materials were acquired from ESPI metals (Ashland, Oregon). The composition of each material was assessed independently using inductively coupled plasma mass spectroscopy [310]. The composition of the Al materials in parts per million (ppm) by volume are listed in Table 7. The purity of each material is abbreviated in this study as the number of nines of aluminum in the material, *e.g.* 99.9% aluminum is abbreviated as 3N-Al ("three nines aluminum"). The diameter of all three Al wires was 1.27 mm and the as-received thickness of the Al sheet was 2.07 mm.

**Table 7: A list of the materials tested in this study and the form factor of each specimen is provided. The manufacturer's listed purity of each material is abbreviated as the number of nines of aluminum in the material, e.g. 3N-Al is 99.9% Al. The ppm by volume of trace impurities in each material are also listed. Based on these data, the measured purity of each material is provided as the % of Al.**

| Material | Geometry | Mg | V | Cu | Zn | Ti | Ga | Fe | Si | %Al |
|---|---|---|---|---|---|---|---|---|---|---|
| 3N-Al | Wire | 14 | 3 | 6 | 30 | 182 | 246 | 416 | 146 | 99.9 |
| 4N-Al | Wire | 14 | <1 | 23 | 16 | 5 | 2 | 42 | 21 | 99.99 |
| 5N-Al | Wire | 7 | 3 | 2 | <1 | 4 | 1 | 1 | 1 | 99.999 |
| 4N-Al | Sheet | 5 | 3 | 10 | 10 | 3 | 1 | 40 | 23 | 99.99 |

**Table 8: A summary of the yield strength (YS) and ultimate strength (UTS) of the four materials selected for this study are provided.**

| Material | Geometry | YS (MPa) | UTS (MPa) |
|---|---|---|---|
| 3N-Al | Wire | 49 | 180 |
| 4N-Al | Wire | 42 | 87 |
| 5N-Al | Wire | 9.5 | 13 |
| 4N-Al | Sheet | 48 | 56 |

The as-received microstructures of these four materials were characterized using electron channeling contrast imaging (ECCI) with a Zeiss Supra 55VP field emission scanning electron microscope (SEM). Grain sizes were measured with the lineal intercept method [311]. Grains in all of the wire materials had dimensions of ≈10 μm along the drawing direction and ≈2 μm along the radial direction. Grains in the as-received 4N-Al sheet material were roughly equiaxed, with an average diameter of 110 μm. Second-phase particles ranging from 0.2 to 5 μm were observed in the 3N-Al wire material. Energy dispersive X-ray spectroscopy (EDS) analysis of these particles demonstrated that they were composed of Silicon (Si) and Oxygen (O), which suggests that they were $SiO_2$ particles. These particles will thus be referred to as $SiO_2$ particles in this study. No second-phase particles or inclusions were identified in the 4N-Al and 5N-Al wire materials or in the 4N-Al sheet material.

Specimens of all materials were tested in uniaxial tension with a servohydraulic machine using a constant cross-head displacement rate of 0.127 mm/s, corresponding to pre-necking strain rates of $\sim 10^{-3}$ $s^{-1}$ for wire specimens and $\sim 10^{-2}$ $s^{-1}$ for the sheet specimen. This small difference in strain rate between the wire and sheet specimens is considered negligible and has very little effect on stress-strain behavior [312]. All tests were conducted at room temperature. Due to the quasistatic strain rates combined with the high thermal conductivity of aluminum [313], any temperature rise in specimens during testing was considered negligible. Tensile specimens of the wire materials were cut from the wire spools and clamped in pneumatic grips with a wire length of approximately 100 mm between the grips. The primary axes of wire specimens are defined as the tensile direction (TD), which was parallel to the wire-drawing direction, and perpendicular to the radial direction (RAD). Specimens with hourglass-shaped gauge regions having the same geometry as those used by Noell *et al.* [71] were fabricated from the sheet material using waterjet cutting with a minimum gauge width of 2.79 mm and an overall gauge length of 8.47 mm. Specimens retained the as-rolled sheet thickness of 2.07 mm. The primary axes of sheet specimens are defined as the TD, the long transverse direction (LTD), and the short transverse direction (STD). The TD and LTD are illustrated in Figure 57. The STD was parallel to the sheet thickness. Tensile tests were either conducted until specimen rupture or were interrupted after the specimen reached its ultimate tensile strength (UTS) but before final fracture. In the latter case, the test was interrupted when the load carried by the specimen dropped from the UTS to a predetermined percentage of the UTS. Samples were labelled according to the percent of the UTS at which they were interrupted. For example, a specimen interrupted once the load had dropped from the UTS to 90% of the UTS was labelled 90% of UTS. This convention is illustrated in Figure 57. A total of twelve tensile tests were conducted using the sheet material: three specimens were elongated to failure, and the remainder were interrupted at 90%, 80%, 70%, 60%, 50%, 30%, 25%, 15%, and

10% of the UTS, respectively. Three specimens of each of the three wire materials were elongated to failure.

Strain measurements were performed for the 4N-Al sheet material using stereoscopic (two-camera) digital image correlation (DIC) [314]. An area of approximately 37 × 14 mm was examined using a 11.8 μm/pixel resolution. DIC was carried out using Vic3D (version 7.2.6), a commercially available program for DIC from Correlated Solutions, Inc. Strain measurements were done using a 33 pixel subset size and a 4 pixel step size. As discussed in the results, the specimen necked significantly before fracture. To measure the average strain across the neck rather than across the entire gauge region, strain was measured from DIC data using a 0.7 mm virtual extensometer placed across the neck. A zero-load baseline experiment was used to determine that the noise level of strain measurements was ±0.006%. A plot of engineering stress *versus* engineering strain for a 4N-Al sheet specimen elongated to failure is provided in Figure 57. Strain measurements were not made for the wire materials.

Fracture surfaces were evaluated in the SEM. Fractured specimens were subsequently mounted, ground to the midplane, and polished using 0.05 μm colloidal silica for extended periods to observe the midplane cross-section. Similarly, specimens that were interrupted before final fracture were ground to the midplane and subsequently polished. For sheet specimens, the TD-LTD plane, *i.e.* the plane normal to the STD, was examined. Wire specimens were sectioned along a plane parallel to the TD. In addition to SEM images, EBSD data were collected from polished samples using Oxford HKL AZtec™ [243] software. These data were subsequently processed using MTEX, [244] an extension for MATLAB. As discussed in many previous articles (see for example references [304, 315]), EBSD data can be used to qualitatively assess residual dislocation structure using measurements such as the quality or band contrast of EBSD patterns, kernel average misorientation (KAM), and grain orientation spread (GOS). Band contrast maps were made using a value of 180 as the upper limit for "high-quality" patterns and 25 as the lower limit for "low-quality" patterns. KAM was calculated from these EBSD data using the misorientation between each pixel and its nearest neighbors. GOS was calculated using the average orientation of each grain as the reference orientation for that grain. The lower bound of the geometrically necessary dislocation density [316] in deformed samples was estimated from EBSD data with the method presented by Pantleon [317] as implemented in MTEX [244].

## 6.3. Results

### *6.3.1. Failure in the Al wire materials*

The fracture behavior of high-purity Al was studied in three Al wires having nominal purities between 3N-Al and 5N-Al. ECCI images of the as-received microstructures of these three materials are provided in Figure 53. As described in the previous section, $SiO_2$ particles were identified in the 3N-Al wire. No particles or inclusions were observed in the 4N or 5N-Al wires.

To study the failure process in these materials, three specimens of each of the three wire materials were elongated to failure. Macrofractographs of representative fractured specimens of each material are provided in Figure 54. These results are analogous to those of Chin *et al.* [22]: the number of dimples on the fracture surface decreased with increasing purity until, for the highest purity wire material, specimens necked to a chisel point. However, high-magnification images of the fracture surface of the 5N-Al wire revealed a few, small (≈2 μm) dimples. Several of these are shown in the inset in Figure 54c. These dimples indicate that voids nucleated shortly before final rupture. The approximate density of dimples on the fracture surface of each of these materials is provided in Table 3.

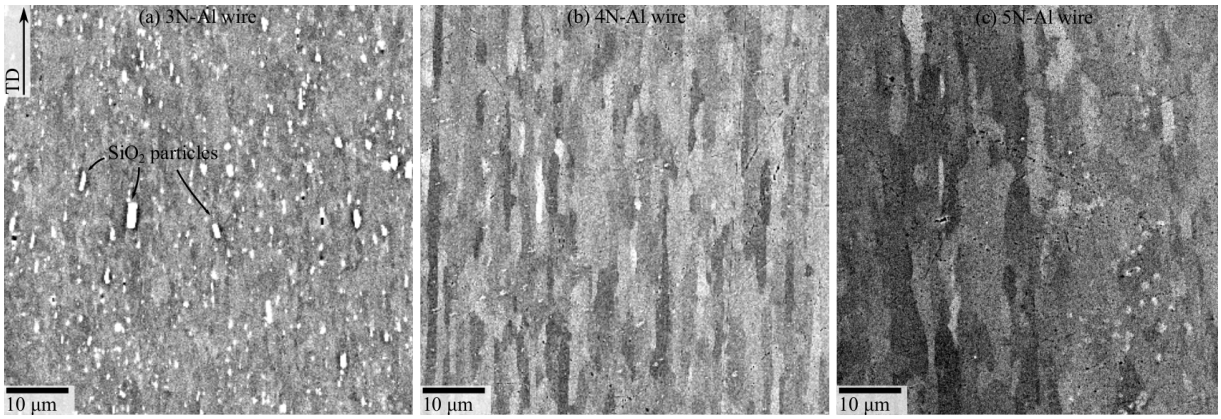


**Figure 56. Representative ECCI images of the as-received microstructures of the (a) 3N-Al wire, (b) 4N-Al wire, and (c) 5N-Al wire are shown. A few of the $SiO_2$ particles in the 3N-Al wire are identified. No particles were observed in the 4N or 5N-Al wires.**

ECCI images of the midplane cross-section of fractured specimens of each of the wire materials are also provided in Figure 54. The cross-section in Figure 54a shows that, in the 3N-Al wire material, voids nucleated throughout the necked gauge region at $SiO_2$ particles. The 3N-Al material thus provides a useful example of void nucleation by conventional particle-based mechanisms. In the 4N-Al material, voids were localized to a narrow band within ≈5 μm of the failure plane. A few such voids are highlighted in the inset in Figure 54b. No voids were identified in a midplane cross section of the fractured 5N-Al wire.

**Table 9: The approximate density of dimples on the fracture surfaces of the 3N, 4N, and 5N-Al wire materials and the 4N-Al sheet material are provided. These measurements were made using 2000 $\mu m^2$ SEM images of the fracture surfaces of these four materials.**

| Material | Geometry | Dimples ($\mu m^{-2}$) |
|---|---|---|
| 3N-Al | Wire | $10^{-1}$ |
| 4N-Al | Wire | $10^{-3}$ |
| 5N-Al | Wire | $10^{-3}$ |
| 4N-Al | Sheet | $10^{-3}$ |

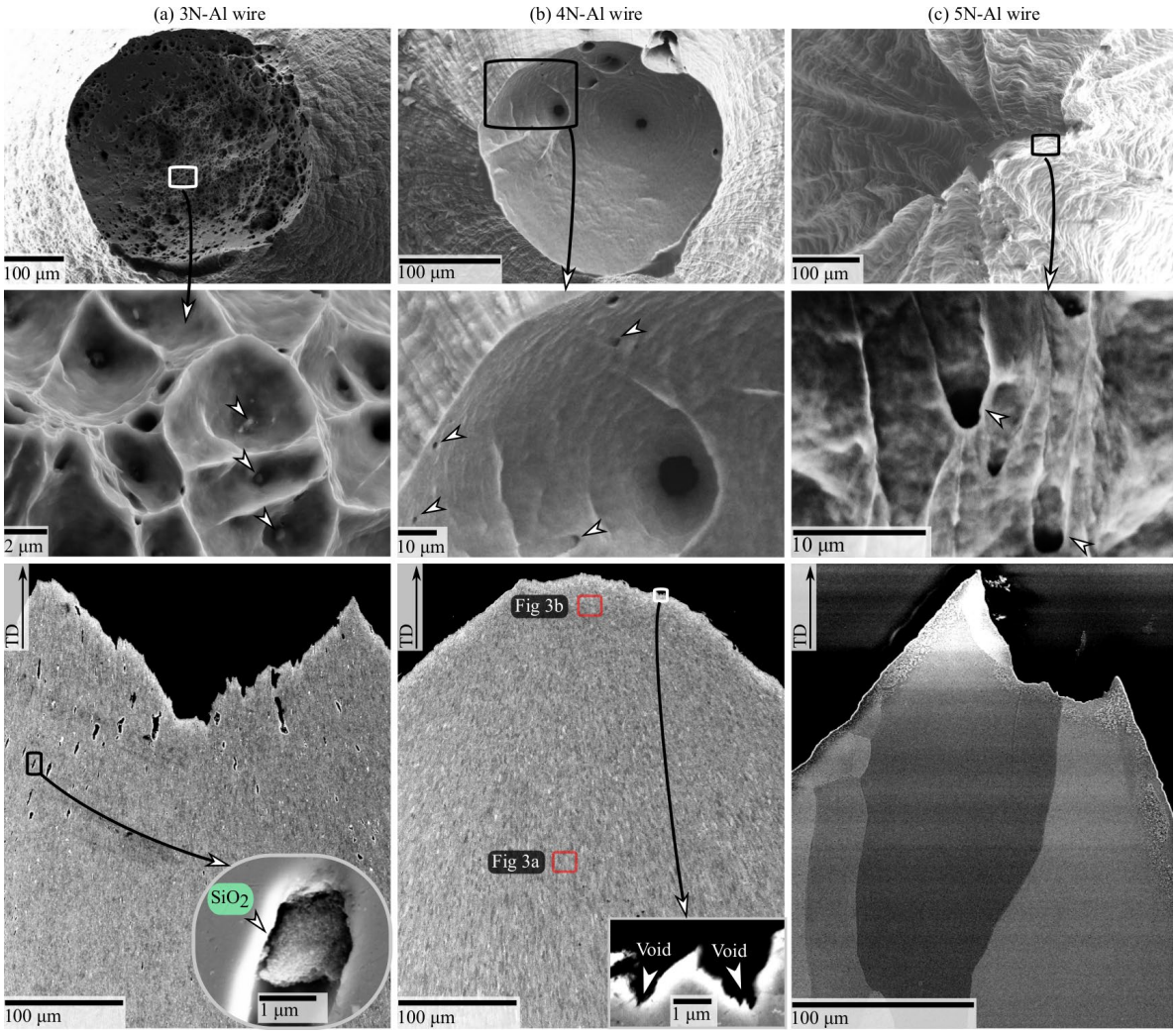


**Figure 57. Images of representative fractured (a) 3N-Al, (b) 4N-Al, and (c) 5N-Al wire specimens are shown. The upper row shows macrofractographs of fractured specimens of each material. The middle row shows high magnification images of the fracture surfaces of each material. Arrows in (a) highlight $SiO_2$ particles at the base of dimples, (b) dimples on the fracture surface, and (c) dimples on the fracture surface. The lower row shows ECCI images of the midplane cross-section of fractured specimens of each material. Insets highlight important microstructural features: (a) shows a void that nucleated at a $SiO_2$ particle in the 3N-Al wire and (b) shows voids at the fracture surface of the 4N-Al wire.**

Qualitatively, the grain structure apparent in the ECCI image of the midplane cross-section of a fractured 5N-Al specimen is significantly different from the as-received grain structure: grains in the fractured specimen are approximately an order of magnitude larger and appear to have a significantly lower dislocation content than those in the as-received material (see Figure 53c). These differences are typical of discontinuous dynamic recrystallization (DRX), a process that is known to occur in high-purity Al during room-temperature deformation [305, 306, 307, 308, 309]. The details of DRX in this material are outside the scope of this study; more details on the factors that control DRX in Al can be found in references [305, 306, 307, 308, 309]. In the present study, we instead focus on how this process affects ductile fracture in Al.

EBSD data from the fractured 4N-Al wire shown in Figure 54b indicate that DRX also occurred during deformation of the 4N-Al wire. EBSD data were collected from the from the microstructure approximately 200 μm from the fracture surface and the microstructure near the fracture surface, as the labels in Figure 54b highlight. Reduction in area measurements at these two locations indicate that they underwent true strains of approximately 1.7 and 3.3, respectively. These EBSD datasets are plotted as inverse pole figure (IPF) maps in Figure 55. Clear differences in texture and grain morphology were observed between these two regions of the microstructure. Grains far from the fracture surface were elongated along the tensile axis and had a strong ⟨111⟩ fiber parallel to the TD typical of heavily deformed FCC metals. In contrast, grains near the fracture surface were equiaxed and had a random texture. The most logical explanation for these differences is that DRX occurred in the local vicinity of the failure surface where the strain levels were largest. No evidence of DRX was observed in the 3N-Al wire material.

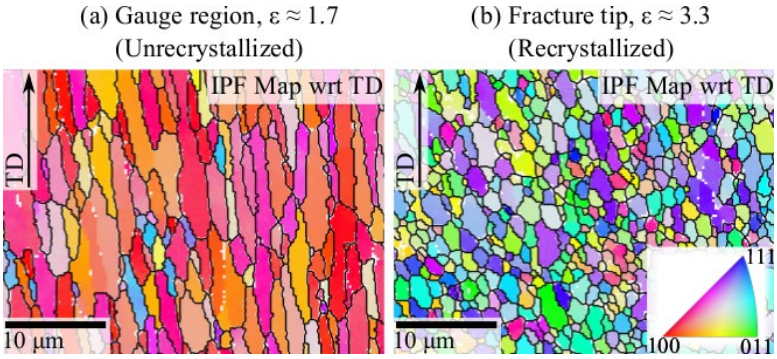


**Figure 58. EBSD data from the microstructure in the 4N-Al wire in the (a) unrecrystallized gauge region ≈200 μm from the fracture surface, and (b) recrystallized gauge region ≈20 μm from the fracture surface are provided. These data are plotted as IPF maps colored with respect to the TD. The areas of the microstructure from which these data were collected are highlighted in Figure 54b. Black lines overlaid on the IPF maps highlight grain boundaries with misorientations of 5° or more across them.**

### *6.3.2. Failure in the Al sheet material*

While the differences in DRX between these wire materials are outside the scope of this study, the results presented in the previous section provide a key insight into failure mechanisms in Al: void nucleation was limited in the Al wire materials that dynamically recrystallized. This observation motivated a detailed investigation of the failure process in high-purity Al. These tests were performed on a 4N-Al sheet material, which is more conducive to interrupted testing and *in-situ* strain measurements than the wire materials. EBSD data from the as-received microstructure of the 4N-Al sheet material are shown in **Figure 56**. These data are plotted as IPF maps colored with respect to the TD and STD, as a band contrast map, and as a KAM map. These data clearly indicate that this material contained significant residual dislocation substructures from cold working. The average GOS measured for grains in the as-received microstructure was 3.96°.

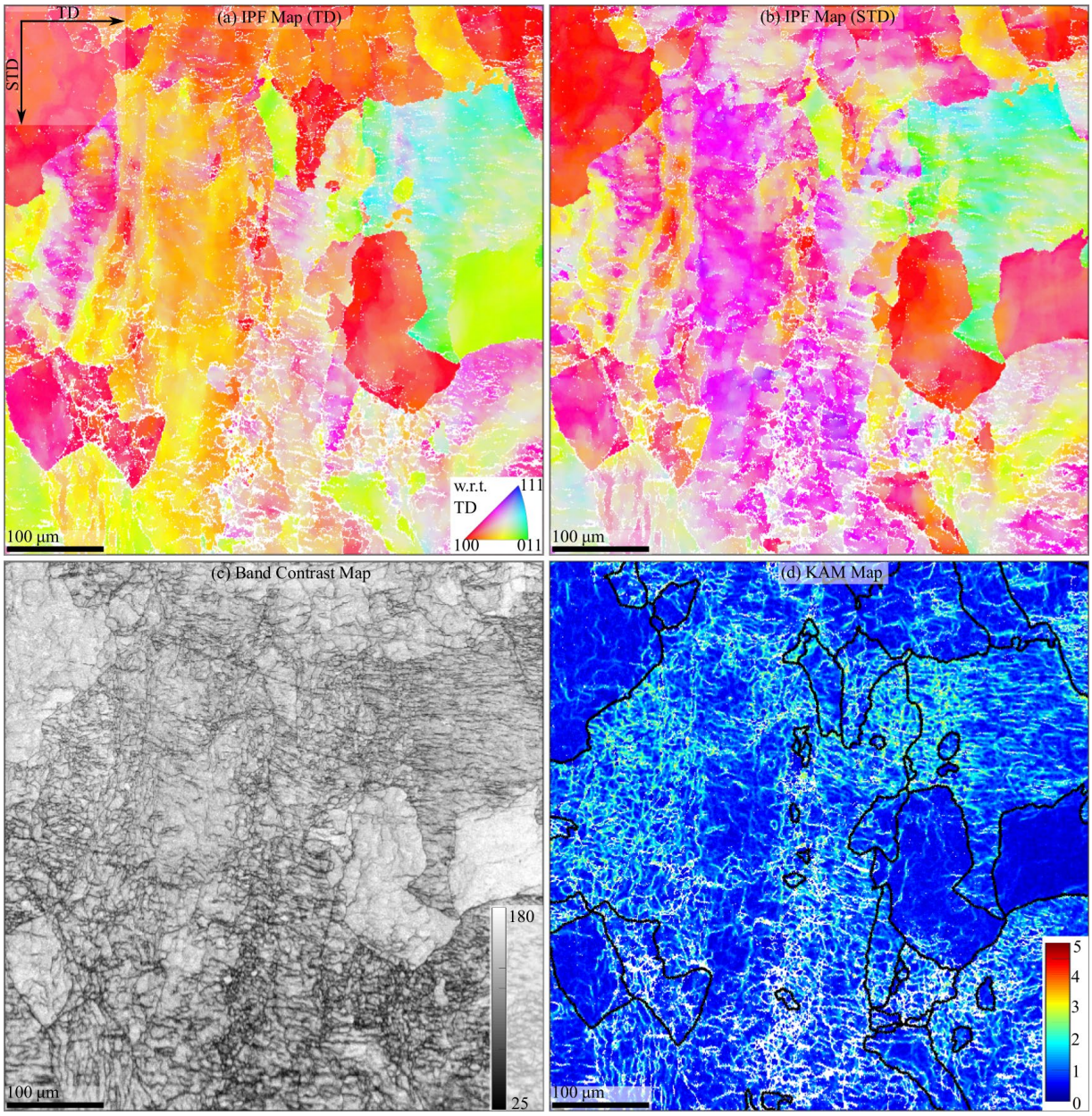


**Figure 59. EBSD data from the as-received 4N-Al sheet material are plotted as inverse pole figure (IPF) maps colored with respect to the (a) TD and (b) STD, a (c) band contrast (image quality) map, and a (d) kernel average misorientation (KAM) map. Black lines overlaid on the KAM map highlight grain boundaries with misorientations of 5° or more across them.**

A plot of engineering stress *versus* engineering strain for this specimen is shown in Figure 57. An image of the fracture surface of a representative fractured specimen is provided in Figure 58a. An ECCI image of the midplane cross-section of this fracture surface is provided in Figure 58b. A high magnification SEM image of part of this fracture surface is shown in Figure 58c.

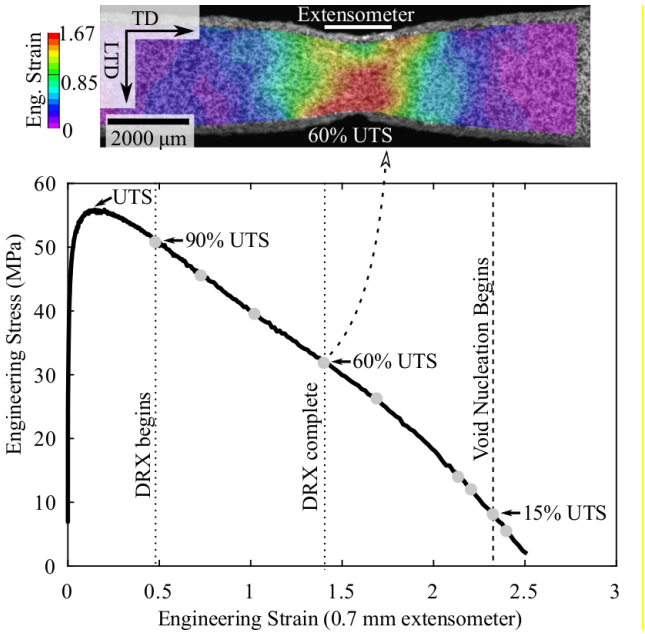


**Figure 60. Engineering stress *versus* engineering strain data from a tensile test of the 4N-Al sheet material are presented. Gray dots on the plot denote where deformation of seven other 4N-Al tensile specimens was interrupted. To illustrate the size of the extensometer relative to the neck, an optical image overlaid with DIC data is shown above this plot. This image was taken at 60% of the UTS.**

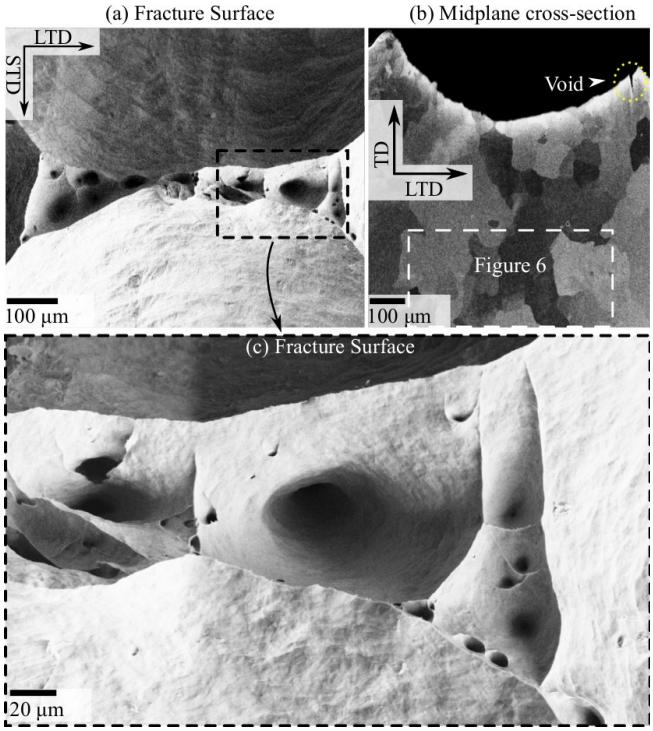


**Figure 61. An image of the fracture surface of a 4N-Al sheet specimen is shown in (a). An ECC image of a midplane cross section of this specimen is shown in (b). For reference, the highlighted area in (b) is also highlighted in Figure 6. A high-magnification SEM image of the fracture surface is shown in (c).**

The fracture surface shown in Figure 58a indicates that this specimen failed by void nucleation, growth, and coalescence. One of these voids can be seen in the ECC image in Figure 58b. The density of dimples on the fracture surface of this material was approximately $10^{-3}$ μm$^{-2}$. This is the same order of magnitude as that on the surfaces of the 4N-Al and 5N-Al wires (see Table 9).

Figure 59 shows an ECCI image of the cross-sectioned midplane of the gauge region of a fractured 4N-Al specimen. The relationship between this area of the microstructure and the fracture surface can be seen by comparing the highlighted regions in Figure 58a and Figure 59. The microstructure in the necked gauge region near the fracture was significantly different from that outside the neck. This can be seen in the ECC image provided in. Qualitatively, grains near the fracture surface appear relatively dislocation-free compared to those outside the necked gauge region.

EBSD data were collected near the area highlighted in Figure 58b. These EBSD are presented in Figure 60 as IPF maps colored with respect to the TD and STD, a band contrast map, and a KAM map. Carbon residue artifacts from specimen preparation appear as black (low band contrast) spots in Figure 60c and in Figure 60d as localized areas of elevated KAM. The average grain size of the material near the fracture surface, measured using these EBSD data, was 102 μm. The average GOS of grains in the map shown in Figure 60 is 0.63°. Recall that the angular resolution of EBSD is approximately ±0.5° [318]. The GOS of grains in the necked gauge region is thus close to the angular resolution limit of EBSD and is significantly smaller than the GOS measured in the as-received 4N-Al material, 3.98°. While GOS only provides qualitative information about differences in dislocation

density, previous studies have demonstrated that similar differences in GOS in Al and other materials are typical of microstructures before and after recrystallization [319, 320, 321, 322, 323]. It is thus concluded that the 4N-Al sheet material recrystallized during deformation.

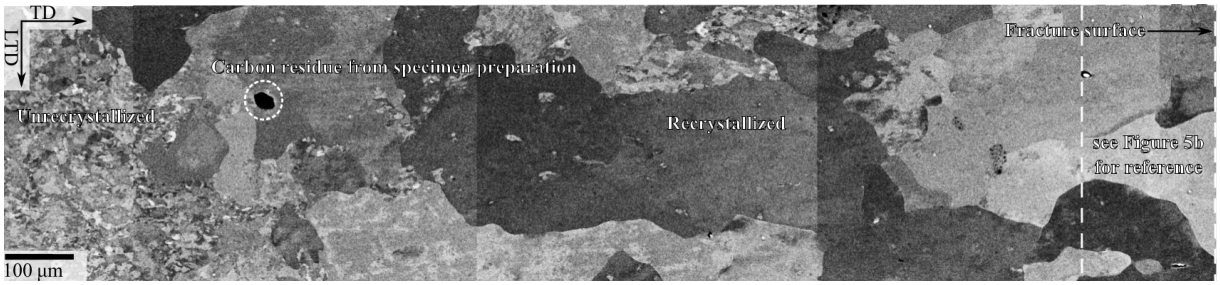


**Figure 62. An ECC image of the material below the fracture surface of the 4N-Al sheet material is shown. The box highlighted in this figure is shown in Figure 58b.**

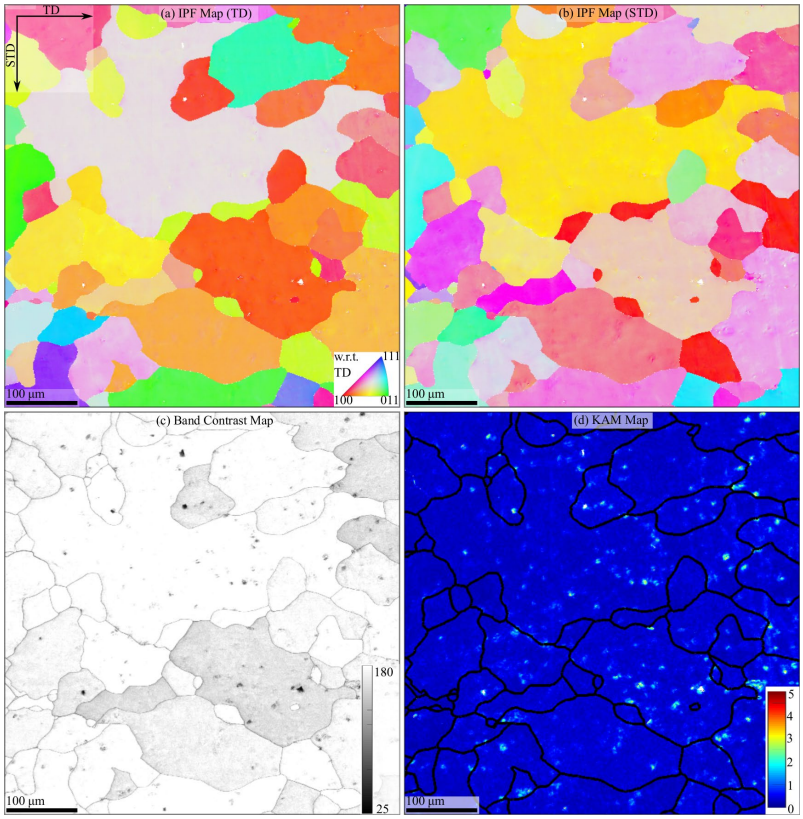


**Figure 63. EBSD data from the microstructure near the fracture surface of a 4N-Al sheet specimen are plotted as IPF maps colored with respect to the (a) TD and (b) STD, as a (c) band contrast (image quality) map, and (d) as a KAM map. Black lines overlaid on the KAM map highlight grain boundaries with misorientations of 5° or more across them. These EBSD data were collected from the area near the box highlighted in shown in Figure 58b.**

To assess how DRX affected ductile fracture in the 4N-Al material, it is necessary to understand when it occurred relative to void nucleation. Most importantly: did DRX occur before, after, or simultaneously with void nucleation? To understand approximately when DRX began and ended in this material, nine specimens were interrupted after the onset of necking, when the forces had dropped from the UTS to 90%, 80%, 70%, 60%, 50%, 30%, 25%, 15%, and 10% of the UTS. Recall that this is in order of increasing strain; the approximate stress and strain at which each of these specimens was interrupted is indicated in Figure 57. Each specimen was cross-sectioned and imaged using ECCI to characterize the underlying microstructure. High-magnification images of the necked gauge regions of specimens interrupted at 90%, 80%, 70%, and 60% of the UTS are provided in Figure 61. A few recrystallized grains were identified in the specimen interrupted at 90% UTS. One of these is observed in Figure 61(a). By 60% of the UTS, almost all of the grains in the diffuse neck appeared to be recrystallized (see Figure 61(d)). Based on these results, the approximate beginning and end of DRX are indicated on the plot in Figure 57.

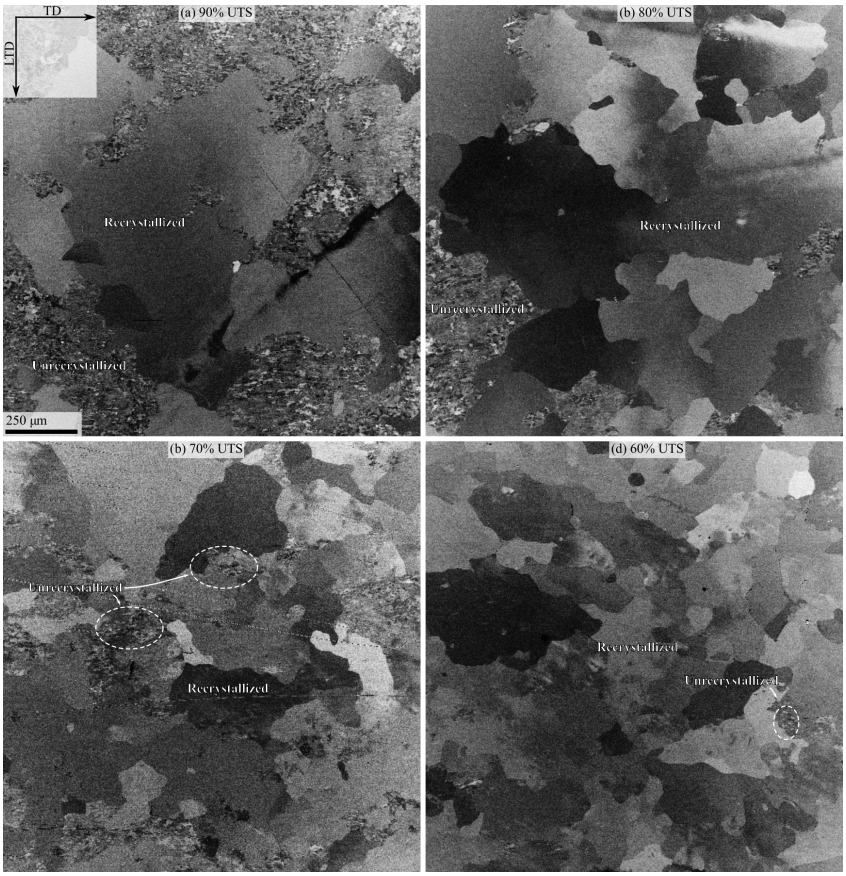


**Figure 64. ECCI images of the midplane cross-sections of specimens interrupted at (a) 90%, (b) 80%, (c) 70%, and (d) 60% UTS are shown. A few of the recrystallized and unrecrystallized grains are identified in each image. Qualitatively, these images suggest that DRX began shortly after necking began (90% UTS) and was nearly complete by 60% UTS. All images are at the same scale.**

ECCI images of specimens interrupted at 50%, 30%, and 10% of the UTS are provided in Figure 62. These images are at a higher magnification than those shown in Figure 61 to enable clearer visualization of residual dislocation structures in the grains. Comparing Figure 62(a) and (b), it appears

that dislocation boundaries reformed within recrystallized grains upon deformation beyond ≈60% UTS, as is generally observed in other materials. No voids were observed in the cross-sectioned midplanes of specimens interrupted at 50%, 30%, or 25% of the UTS. A central void spanning approximately one third of the LTD was observed in a specimen interrupted at 10% of the UTS and can be seen in Figure 62(c). This image suggests that voids nucleated, grew, and coalesced between approximately 25% and 10% of the UTS. Based on the stress *versus* strain data provided in Figure 57, this observation indicates that, once a ductile crack forms in this material at ≈10% of the UTS, specimen separation (fracture) occurs upon a further strain increment of ≈0.15.

Incipient voids (<5 μm) were observed in the cross-sectioned midplane of a specimen interrupted at 15% of the UTS. Thirty voids, ranging in size from ≈1 to 5 μm, were identified in the necked gauge region of this specimen. Several of these are highlighted in Figure 63a, which provides an ECCI image of the necked gauge region of this specimen. The approximate engineering stress and engineering strain when void nucleation began in this material is thus denoted on the plot in Figure 57 to be at 15% of the UTS.

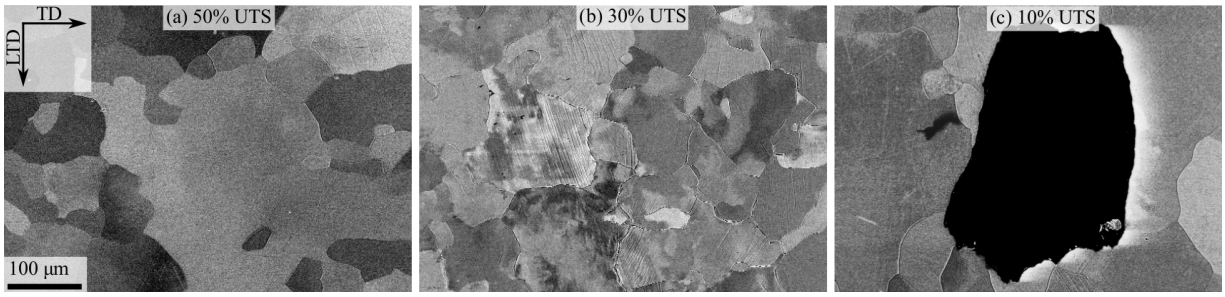


**Figure 65. ECCI images of the midplane cross-sections of specimens interrupted at (a) 50%, (b) 30%, and (c) 10% UTS are shown. All images are at the same scale. A large void can be seen in the center of the specimen interrupted at 10% UTS.**

One of the key questions this study seeks to address was the microstructural features associated with void nucleation. To this end, the microstructural features associated with voids in the specimen interrupted at 15% of the UTS were characterized using EBSD and high-magnification ECCI images. A high-magnification ECCI image of one of these voids is provided in Figure 63b. EBSD data from the microstructure around this void, collected with a step size of 50 nm, are plotted as a band contrast (BC) map in Figure 63c and an IPF map colored with respect to the STD in Figure 63d. These data demonstrate that the void did not intersect a grain boundary within the plane examined. Instead, it was associated with a dislocation boundary. The dislocation boundaries within the grains near this void can be seen both within the ECCI image and the BC map. A sketch of the dislocation boundaries near this void is provided in Figure 63e. The average misorientations across these boundaries and the closest grain boundary are labelled in this sketch. These data show that the void was associated with a low-angle dislocation boundary, likely a dislocation cell wall. Similar analysis of another void in this specimen demonstrated that it was also associated with a low-angle dislocation boundary. Using the method described by Pantleon [317], the EBSD data collected near these incipient voids were used to estimate the lower bound of the geometrically necessary dislocation (GND) density [304, 317] in the vicinity of these voids for the 50 nm stepsize used. GND densities in the microstructure around both voids were $\approx 10^{14}$ $m^{-2}$ (the center of the dislocation cells) and $\approx 10^{15}$ $m^{-2}$ (the dislocation cell walls).

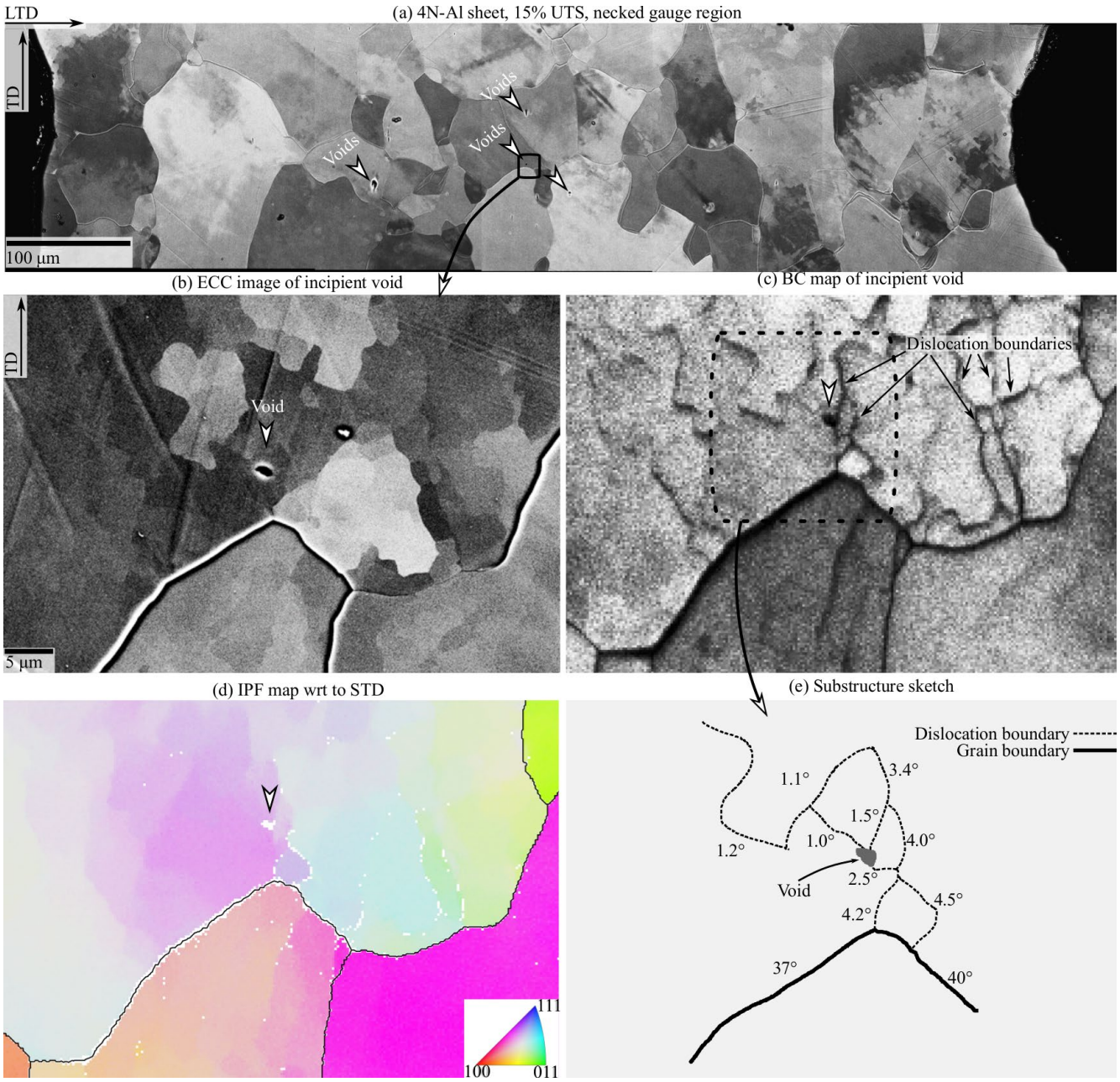


**Figure 66. An ECCI image of the center of the necked gauge region of a 4N-Al sheet specimen interrupted at 15% of the UTS is shown in (a). A high-magnification ECCI image of the microstructure around one of the voids in (a) is shown in (b). EBSD data from the microstructure around this void are presented as (c) a band-contrast (BC) map and (d) an IPF map colored with respect to the STD. Black lines overlaid on the map in (d) delineate grain boundaries. The sketch in (e) illustrates some of the dislocation boundaries and grain boundaries near this void and the misorientations across them.**

## 6.4. Discussion

### *6.4.1. Void nucleation in particle-free Al*

Figure 63 presents a key finding from this study: voids in a particle-free Al material nucleated at dislocation boundaries. This is consistent with prior observations in BCC metals, where it was observed that voids nucleated exclusively at dislocation boundaries [71]. It is thus reasonable to conclude that void nucleation in particle-free, wavy glide metals depends on establishing a dislocation substructure consisting of dislocation boundaries. Once established, these dislocation boundaries appear to be the primary void nucleation sites in both BCC and FCC materials that deform by slip. This key finding indicates that dislocation/dislocation interactions to form boundaries are crucial to void nucleation in particle free materials.

Several prior studies examined DRX in Al and its dependence on microstructure, prior cold work, and other factors [305, 306, 307, 308, 309]. The microscopy presented in Figure 53, Figure 54, Figure 55, Figure 59 and Figure 60 indicates that DRX occurred during deformation of three of the four Al materials examined in this study. Differences in DRX between these three materials are outside the scope of the present study; instead, we examine how DRX influences ductile fracture in Al.

If, as Figure 63 demonstrates, voids in particle-free Al nucleate at dislocation boundaries, it follows that void nucleation will be delayed until such boundaries form. As shown in Figure 61, DRX began in the 4N-Al sheet material shortly after necking began. This process continued until approximately 60% of the UTS. As Figure 62 demonstrates, subsequent deformation was then necessary to reform dislocation boundaries in the necked gauge region. It thus appears that DRX delayed void nucleation in the 4N-Al material by annihilating dislocation boundaries, the primary microstructural feature associated with void nucleation. Furthermore, comparing the fracture behaviors of the three Al wire materials indicates that void nucleation was also limited in the two wire materials that dynamically recrystallized during deformation. DRX thus appears to limit void nucleation in high-purity Al materials by eliminating the dislocation boundaries at which voids nucleate. The differences observed between the fracture surfaces of the 4N-Al and 5N-Al wire may then be related to differences in DRX between these two materials.

These insights show that FCC metals are not uniquely resistant to void nucleation. Rather, void nucleation appears to be controlled by the same microstructural features in BCC and FCC metals that deform by slip. It is likely that the limited void nucleation observed in Pb can also be attributed to the effects of room-temperature DRX, since this is known to occur in Pb [324]. Both the creation and persistence of dislocation boundaries are thus essential to void nucleation in particle-free metals.

This conclusion implies that voids would nucleate readily in high-purity Al if DRX did not occur and dislocation boundaries were correspondingly allowed to form. DRX can be suppressed in this material by testing at temperatures below the recrystallization temperature, which Haessner *et al.* [325] estimated to be between -40° and 10° C. Although such cryogenic tests were not performed in this study, Chin *et al.* observed that the same high-purity Al samples that failed without voids at room temperature failed by void coalescence at -230° C [22]. This result further suggests that void nucleation would occur readily in Al if DRX did not occur.

### *6.4.2. Void nucleation, dislocation density, and the hydrostatic stress*

Perhaps the most surprising aspect of this study was the observation that voids nucleated in the 4N-Al sheet material after DRX rather than before. Two mechanisms for void nucleation in inclusion-free materials, such as the 4N-Al sheet material, have been proposed:

1. voids nucleate to relieve the local elastic stress produced by excess dislocations (*e.g.* dislocation pile-ups and dislocation boundaries) [1, 3, 97, 141], and
2. voids nucleate by vacancy condensation [71, 302].

According to both mechanisms, the likelihood for void nucleation increases with increasing dislocation density [71, 97]. However, in the 4N-Al sheet material, it is clear from comparing **Figure 56** and Figure 60 that the dislocation density in the as-received material was significantly greater in the necked gauge region of fractured specimens. Because DRX depends on attaining a critical dislocation density [326], it is reasonable to conclude that the dislocation density immediately before DRX at ≈90% of the UTS was even larger than that in the as-received material and thus significantly greater than that at void nucleation. Why then did voids appear after DRX rather than before it?

In addition to the dislocation density, another important difference between the conditions at 90% and 15% of the UTS, *i.e.* before DRX and after void nucleation began, is the hydrostatic stress state. This affects void nucleation in several ways (as discussed in the next paragraph). Because the specimen necked significantly after DRX occurred, the hydrostatic stresses became significantly elevated. The hydrostatic stress in the center of the neck can be estimated using the Bridgman [60] equation,

$$\frac{\sigma_m}{Y} = \frac{1}{3} + \ln\left(\frac{a + 2R}{2R}\right) \quad 1$$

where $\frac{\sigma_m}{Y}$ is the stress triaxiality, $a$ is the cross-sectional radius at the neck, and $R$ is the neck radius. $R$ was estimated from DIC images by fitting a cylinder to the necked region using polynomial surface fitting in MATLAB. These data suggest that the stress triaxiality when DRX began, when DRX ended, and when void nucleation began were approximately 0.37, 0.42, and 0.77, respectively. This latter value (0.77) is a conservative estimate for the stress triaxiality at void nucleation; the neck was asymmetrical, with a significantly larger radius $R$ on one side than the other. Neck asymmetry is common in sheet tensile samples and is often due to surface imperfections [327, 328]. The value of 0.77 was calculated using this maximum value of $R$. Using the minimum value of $R$ provides a stress triaxiality of 1.25 at void nucleation.

It is hypothesized that hydrostatic stresses are critical to the early stages of void nucleation in particle-free metals for two reasons. First, hydrostatic stresses provide a driving force that promotes vacancy aggregation into voids [329]. Second, studies of vacancy condensation in quenched aluminum have demonstrated that vacancy clusters collapse into dislocation loops or stacking fault tetrahedra unless they are stabilized [191, 192, 194, 330]. During plastic deformation, the work applied by the hydrostatic stress is the likeliest stabilization mechanism for vacancy clusters [229]. Void nucleation may thus have been delayed until the hydrostatic stress produced by the neck was sufficiently large to stabilize critical void nuclei.

Hydrostatic stresses may also be important to the failure of Al specimens because they control the void growth rate, thereby affecting the ability for voids to grow large enough to coalesce. For example, according to the well-known Rice-Tracey relation [31], the void growth rate varies exponentially with the hydrostatic stress as

$$\frac{\dot{r}}{r} = \alpha \exp\left(\frac{3\sigma_m}{2Y}\right)\dot{\varepsilon}^{eq}. \quad 2$$

where $r$ is the void radius, $\dot{\varepsilon}^{eq}$ is the von Mises equivalent strain rate, and $\alpha$ is a numerical constant. Using the estimated stress triaxialities, the relative void growth rates were $1X$, $1.1X$, and $1.8X$ for the points where DRX began, DRX ended, and void nucleation began. If the maximum stress triaxiality calculated at void nucleation is used, the relative void growth rate when void nucleation began was $3.7X$. Hence, the driving force for void growth was 2 to 4 times as high at 15% UTS, when mesoscale voids were first observed, than before DRX occurred. It is hypothesized that this was another factor that made it possible for voids to affect the rupture process at lower dislocation densities than those present immediately before DRX.

## 6.5. Conclusion

The present study examines the mechanisms of void nucleation in particle-free Al. In conclusion, the present study demonstrated that:

1. 2nd-phase particles are not necessary for void nucleation in high-purity FCC metals that deform by slip. Voids nucleated in the absence of second-phase particles at deformation-induced dislocation boundaries. This result, combined with other recent observations of ductile rupture in high-purity Ta, suggest that the same microstructural features, *i.e.,* dislocation boundaries, control void nucleation in all particle-free metals that deform by slip.

2. Dynamic recrystallization impedes void nucleation in high-purity Al by erasing the dislocation boundaries necessary for void nucleation. For voids to nucleate in Al, these boundaries must reform after DRX.

These observations indicate that dislocation/dislocation interactions to create dislocation cell walls and cell block boundaries are critical to void nucleation in particle-free materials. It is also hypothesized that the elevated hydrostatic stress in the necked gauge region enhances the rate of void nucleation in particle-free materials by stabilizing vacancy clusters.

# 7. REFERENCES


1. Jagannadham K, Wilsdorf HGF. Low energy dislocation structures associated with cracks in ductile fracture. Materials Science and Engineering. 1986;81:273-292.
2. Puttick KE. Ductile fracture in metals. Philosophical magazine. 1959;4(44):964-969.
3. Zener C. The micro-mechanism of fracture. Fracturing of metals. 1948;3.
4. Zhang Y, Millett PC, Tonks M, et al. Deformation-twin-induced grain boundary failure. Scripta Materialia. 2012;66(2):117-120.
5. Wronski A, Fourdeux A. Slip-induced cleavage in polycrystalline tungsten. Journal of the Less Common Metals. 1964;6(6):413-429.
6. Warren M, Beevers O. The interrelationship between deformation and crack nucleation and propagation in zirconium containing hydride precipitates. Journal of Nuclear Materials. 1968;26(3):273-284.
7. Dawson HI. Experimental verification of Saada's relation on the production of point defects in FCC metals by plastic straining at -195 C. Physica. 1965;31(3):342-348.
8. Bieler T, Eisenlohr P, Zhang C, et al. Grain boundaries and interfaces in slip transfer. Current Opinion in Solid State and Materials Science. 2014;18(4):212-226.
9. Teirlinck D, Zok F, Embury J, et al. Fracture mechanism maps in stress space. Acta Metallurgica. 1988;36(5):1213-1228.
10. Benzerga A, Besson J, Pineau A. Anisotropic ductile fracture: Part I: experiments. Acta Materialia. 2004;52(15):4623-4638.
11. Teng X, Wierzbicki T. Evaluation of six fracture models in high velocity perforation. Engineering Fracture Mechanics. 2006;73(12):1653-1678.
12. Bieler TR, Crimp MA, Yang Y, et al. Strain heterogeneity and damage nucleation at grain boundaries during monotonic deformation in commercial purity titanium. Jom. 2009;61(12):45-52.
13. Gardner RN, Pollock TC, Wilsdorf HGF. Crack initiation at dislocation cell boundaries in the ductile fracture of metals. Materials Science and Engineering. 1977;29(2):169-174.
14. Shakoor M, Bernacki M, Bouchard P-O. Ductile fracture of a metal matrix composite studied using 3D numerical modeling of void nucleation and coalescence. Engineering Fracture Mechanics. 2018;189:110-132.
15. Williams J, Flom Z, Amell A, et al. Damage evolution in SiC particle reinforced Al alloy matrix composites by X-ray synchrotron tomography. Acta Materialia. 2010;58(18):6194-6205.
16. Hansen N, Jensen DJ. Development of microstructure in FCC metals during cold work. Philosophical Transactions of the Royal Society of London A: Mathematical, Physical and Engineering Sciences. 1999;357(1756):1447-1469.
17. Spencer K, Corbin S, Lloyd D. The influence of iron content on the plane strain fracture behaviour of AA 5754 Al–Mg sheet alloys. Materials Science and Engineering: A. 2002;325(1-2):394-404.
18. Cui Y, Chen Z. Void initiation from interfacial debonding of spherical silicon particles inside a silicon-copper nanocomposite: a molecular dynamics study. Modelling and Simulation in Materials Science and Engineering. 2016;25(2):025007.
19. Cox T, Low JR. An investigation of the plastic fracture of AISI 4340 and 18 Nickel-200 grade maraging steels. Metallurgical Transactions. 1974;5(6):1457-1470.
20. Barsoum I, Faleskog J. Rupture mechanisms in combined tension and shear—Experiments. International Journal of Solids and Structures. 2007;44(6):1768-1786.
21. Barsoum I, Faleskog J. Rupture mechanisms in combined tension and shear—

Micromechanics. International Journal of Solids and Structures. 2007;44(17):5481-5498.
22. Chin GY, Hosford WF, Backofen WA. Ductile fracture of aluminum. Transactions of the Metallurgical Society of AIME. 1964;230(3):437.
23. Nahshon K, Hutchinson J. Modification of the Gurson model for shear failure. European Journal of Mechanics-A/Solids. 2008;27(1):1-17.
24. Sharon J, Hattar K, Boyce B, et al. Compressive Properties of⟨ 110⟩ Cu Micro-Pillars after High-Dose Self-Ion Irradiation. Materials Research Letters. 2014;2(2):57-62.
25. Boyce BL, Kramer SLB, Bosiljevac TR, et al. The second Sandia Fracture Challenge: predictions of ductile failure under quasi-static and moderate-rate dynamic loading. International Journal of Fracture. 2016;198(1-2):5-100.
26. Weinrich PF, French IE. The influence of hydrostatic pressure on the fracture mechanisms of sheet tensile specimens of copper and brass. Acta Metallurgica. 1976;24(4):317-322.
27. Williams ML. The bending stress distribution at the base of a stationary crack. Journal of applied mechanics. 1961;28(1):78-82.
28. Rice J. Mechanics of crack tip deformation and extension by fatigue. Fatigue crack propagation: ASTM International; 1967.
29. Rice J, Rosengren GF. Plane strain deformation near a crack tip in a power-law hardening material. Journal of the Mechanics and Physics of Solids. 1968;16(1):1-12.
30. Boyce BL, Kramer SLB, Fang HE, et al. The Sandia Fracture Challenge: blind round robin predictions of ductile tearing. International Journal of Fracture. 2014;186(1-2):5-68.
31. Rice JR, Tracey DM. On the ductile enlargement of voids in triaxial stress fields. Journal of the Mechanics and Physics of Solids. 1969;17(3):201-217.
32. Gurson AL. Continuum theory of ductile rupture by void nucleation and growth: Part I—Yield criteria and flow rules for porous ductile media. Journal of engineering materials and technology. 1977;99(1):2-15.
33. Tvergaard V, Needleman A. Analysis of the cup-cone fracture in a round tensile bar. Acta metallurgica. 1984;32(1):157-169.
34. Hutchinson JW, Tvergaard V. Shear band formation in plane strain. International Journal of Solids and Structures. 1981;17(5):451-470.
35. Tvergaard V, Hutchinson JW. Two mechanisms of ductile fracture: void by void growth versus multiple void interaction. International Journal of Solids and Structures. 2002;39(13-14):3581-3597.
36. Bao Y, Wierzbicki T. On fracture locus in the equivalent strain and stress triaxiality space. International Journal of Mechanical Sciences. 2004;46(1):81-98.
37. McClintock FA. A criterion for ductile fracture by the growth of holes. Journal of applied mechanics. 1968;35(2):363-371.
38. Hancock J, Mackenzie A. On the mechanisms of ductile failure in high-strength steels subjected to multi-axial stress-states. Journal of the Mechanics and Physics of Solids. 1976;24(2-3):147-160.
39. Johnson GR, Cook WH. Fracture characteristics of three metals subjected to various strains, strain rates, temperatures and pressures. Engineering fracture mechanics. 1985;21(1):31-48.
40. Beese AM, Luo M, Li Y, et al. Partially coupled anisotropic fracture model for aluminum sheets. Engineering Fracture Mechanics. 2010;77(7):1128-1152.
41. Li H, Fu M, Lu J, et al. Ductile fracture: experiments and computations. International journal of plasticity. 2011;27(2):147-180.
42. Dunand M, Mohr D. On the predictive capabilities of the shear modified Gurson and the modified Mohr–Coulomb fracture models over a wide range of stress triaxialities and Lode

angles. Journal of the Mechanics and Physics of Solids. 2011;59(7):1374-1394.
43. Papasidero J, Doquet V, Mohr D. Ductile fracture of aluminum 2024-T351 under proportional and non-proportional multi-axial loading: Bao–Wierzbicki results revisited. International Journal of Solids and Structures. 2015;69:459-474.
44. Barsoum I, Faleskog J. Micromechanical analysis on the influence of the Lode parameter on void growth and coalescence. International Journal of Solids and Structures. 2011;48(6):925-938.
45. Ambati M, Gerasimov T, De Lorenzis L. A review on phase-field models of brittle fracture and a new fast hybrid formulation. Computational Mechanics. 2015;55(2):383-405.
46. Goods SH, Brown LM. Overview No. 1: The nucleation of cavities by plastic deformation. Acta Metallurgica. 1979;27(1):1-15.
47. Oyane M, Sato T, Okimoto K, et al. Criteria for ductile fracture and their applications. Journal of Mechanical Working Technology. 1980;4(1):65-81.
48. Zhang Z, Thaulow C, Ødegård J. A complete Gurson model approach for ductile fracture. Engineering Fracture Mechanics. 2000;67(2):155-168.
49. Lou Y, Huh H, Lim S, et al. New ductile fracture criterion for prediction of fracture forming limit diagrams of sheet metals. International Journal of Solids and Structures. 2012;49(25):3605-3615.
50. Ghahremaninezhad A, Ravi-Chandar K. Ductile failure behavior of polycrystalline Al 6061-T6. International journal of fracture. 2012;174(2):177-202.
51. Ghahremaninezhad A, Ravi-Chandar K. Ductile failure behavior of polycrystalline Al 6061-T6 under shear dominant loading. International Journal of Fracture. 2013;180(1):23-39.
52. Haltom S, Kyriakides S, Ravi-Chandar K. Ductile failure under combined shear and tension. International Journal of Solids and Structures. 2013;50(10):1507-1522.
53. Scales M, Tardif N, Kyriakides S. Ductile failure of aluminum alloy tubes under combined torsion and tension. International Journal of Solids and Structures. 2016;97:116-128.
54. Morgeneyer TF, Taillandier-Thomas T, Helfen L, et al. In situ 3-D observation of early strain localization during failure of thin Al alloy (2198) sheet. Acta Materialia. 2014;69:78-91.
55. Pineau A, Benzerga AA, Pardoen T. Failure of metals I: Brittle and ductile fracture. Acta Materialia. 2016;107:424-483.
56. Orowan E. Fracture and strength of solids. Reports on progress in physics. 1949;12(1):185.
57. Miller DR, Besag FMC, editors. Metallographic Studies of Ductile Fracture in High Purity Aluminium and Lead. Proceedings 1st International Conference on Fracture, Sendai, 1965, Vol. II, Japan 1965; 1965.
58. French IE, Weinrich PF. The effect of hydrostatic pressure on the tensile fracture of $$-brass. Acta metallurgica. 1973;21(11):1533-1537.
59. Benzerga AA, Leblond J-B. Ductile fracture by void growth to coalescence. Advances in applied mechanics. Vol. 44: Elsevier; 2010. p. 169-305.
60. Bridgman PW. Studies in large plastic flow and fracture. Vol. 177. McGraw-Hill New York; 1952.
61. French IE, Weinrich PF. The effects of hydrostatic pressure on the mechanism of tensile fracture of aluminum. Metallurgical Transactions A. 1975;6(6):1165-1169.
62. French IE, Weinrich PF. The influence of hydrostatic pressure on the tensile deformation and fracture of copper. Metallurgical Transactions A. 1975;6(4):785.
63. Ghahremaninezhad A, Ravi-Chandar K. Ductile failure in polycrystalline OFHC copper. International Journal of Solids and Structures. 2011;48(24):3299-3311.
64. Low Jr JR. The fracture of metals. Progress in materials science. 1963;12:3-96.
65. Tekoğlu C, Hutchinson J, Pardoen T. On localization and void coalescence as a precursor to

ductile fracture. Philosophical Transactions of the Royal Society A: Mathematical, Physical and Engineering Sciences. 2015;373(2038):20140121.
66. Callister Jr WD, Rethwisch DG. Fundamentals of materials science and engineering: an integrated approach. John Wiley & Sons; 2012.
67. Boyer HE. Atlas of Stress--strain Curves. ASM International, Metals Park, Ohio 44073, USA, 1987 630. 1987.
68. Kassner M, McQueen H, Pollard J, et al. Restoration mechanisms in large-strain deformation of high purity aluminum at ambient temperature. Scripta metallurgica et materialia. 1994;31(10):1331-1336.
69. Choi C-H, Jeong J-H, Oh C-S, et al. Room temperature recrystallization of 99.999 pct aluminum. Scripta metallurgica et materialia. 1994;30(3):325-330.
70. Wilsdorf HG. The investigation of the fracture of titanium alloys by in-situ and analytical microstructural techniques. DTIC Document; 1988.
71. Noell P, Carroll J, Hattar K, et al. Do voids nucleate at grain boundaries during ductile rupture? Acta Materialia. 2017;137:103-114.
72. Tipper CF. The fracture of metals. Metallurgia. 1949;39(231):133-137.
73. Cottrell I. AH (1959) Theoretical aspects of fracture. BL Averbach, OK Felbeck, GT Hahn, and OA Thomas (OOs), Fracture MIT press, Cambridge Massachusetts, USA. 1959:20-45.
74. Carroll J, Abuzaid W, Lambros J, et al. An experimental methodology to relate local strain to microstructural texture. Review of Scientific Instruments. 2010;81(8):083703.
75. Buljac A, Taillandier-Thomas T, Morgeneyer TF, et al. Slant strained band development during flat to slant crack transition in AA 2198 T8 sheet: in situ 3D measurements. International Journal of Fracture. 2016;200(1-2):49-62.
76. Hansen N, Mehl RF. New discoveries in deformed metals. Metallurgical and materials transactions A. 2001;32(12):2917-2935.
77. Weck A, Wilkinson D, Maire E. Observation of void nucleation, growth and coalescence in a model metal matrix composite using X-ray tomography. Materials Science and Engineering: A. 2008;488(1-2):435-445.
78. Weck A, Wilkinson D, Maire E, et al. Visualization by X-ray tomography of void growth and coalescence leading to fracture in model materials. Acta Materialia. 2008;56(12):2919-2928.
79. Hosokawa A, Wilkinson DS, Kang J, et al. Onset of void coalescence in uniaxial tension studied by continuous X-ray tomography. Acta Materialia. 2013;61(4):1021-1036.
80. Hosokawa A, Wilkinson DS, Kang J, et al. Void growth and coalescence in model materials investigated by high-resolution X-ray microtomography. International Journal of Fracture. 2013;181(1):51-66.
81. Jagannadham K, Wilsdorf H. Low energy dislocation structures associated with cracks in ductile fracture. Materials Science and Engineering. 1986;81:273-292.
82. Le Roy G, Embury J, Edwards G, et al. A model of ductile fracture based on the nucleation and growth of voids. Acta Metallurgica. 1981;29(8):1509-1522.
83. Bao Y, Wierzbicki T. On the cut-off value of negative triaxiality for fracture. Engineering fracture mechanics. 2005;72(7):1049-1069.
84. Chu C, Needleman A. Void nucleation effects in biaxially stretched sheets. Journal of engineering materials and technology. 1980;102(3):249-256.
85. Pardoen T, Doghri I, Delannay F. Experimental and numerical comparison of void growth models and void coalescence criteria for the prediction of ductile fracture in copper bars. Acta Materialia. 1998;46(2):541-552.
86. Landron C, Bouaziz O, Maire E, et al. Characterization and modeling of void nucleation by interface decohesion in dual phase steels. Scripta Materialia. 2010;63(10):973-976.

87. Zhang Z, édegAard J, Thaulow C, editors. Characterization of material ductility by microvoid nucleation parameters. Proceeding of the 19th Risù International Symposium on material science: Modelling of structure and mechnaics of materials from microscale to product, Risù, Denmark; 1998.
88. Rakin M, Cvijovic Z, Grabulov V, et al. Prediction of ductile fracture initiation using micromechanical analysis. Engineering Fracture Mechanics. 2004;71(4-6):813-827.
89. Caceres C, Griffiths J. Damage by the cracking of silicon particles in an Al-7Si-0.4 Mg casting alloy. Acta materialia. 1996;44(1):25-33.
90. Bauer RW, Wilsdorf HGF, editors. The mechanical behavior in tension and fracture characteristics of stainless steel thin rolled foils. Proceedings of an international conference on Dynamic Crack Propagation; 1973.
91. Chan IYT, Wilsdorf HGF. The ductile fracture of precipitation-hardened Al-1.79 wt.% Cu alloys containing theta' and theta precipitates. Materials Science and Engineering. 1981;49(3):229-240.
92. Chan IY, Wilsdorf HGF. Microstructures at the fracture flank of precipitation hardened Al-1.79 w/o Cu alloys. Acta Metallurgica. 1981;29(7):1221-1235.
93. Fisher J, Gurland J. Void nucleation in spheroidized carbon steels part 1: experimental. Metal Science. 1981;15(5):185-192.
94. Querin J, Schneider J, Horstemeyer M. Analysis of micro void formation at grain boundary triple points in monotonically strained AA6022-T43 sheet metal. Materials Science and Engineering: A. 2007;463(1-2):101-106.
95. Beevers CJ, Honeycombe RWK, editors. Ductile fracture of single crystals. ICF0, Swampscott-MA (USA) 1959; 1959.
96. Beevers CJ, Honeycombe RWK. The initiation of ductile fracture in pure metals. Philosophical Magazine. 1962;7(77):763-773.
97. Wilsdorf HGF. The ductile fracture of metals: a microstructural viewpoint. Materials Science and Engineering. 1983;59(1):1-39.
98. Garrison WM, Moody NR. Ductile fracture. Journal of Physics and Chemistry of Solids. 1987;48(11):1035-1074.
99. Rudd RE, Belak JF. Void nucleation and associated plasticity in dynamic fracture of polycrystalline copper: an atomistic simulation. Computational materials science. 2002;24(1-2):148-153.
100. Rezvanian O, Zikry M, Rajendran A. Statistically stored, geometrically necessary and grain boundary dislocation densities: microstructural representation and modelling. Proceedings of the Royal Society A: Mathematical, Physical and Engineering Sciences. 2007;463(2087):2833-2853.
101. Boyce BL, Clark BG, Lu P, et al. The morphology of tensile failure in tantalum. Metallurgical and Materials Transactions A. 2013;44(10):4567-4580.
102. Kuhlmann-Wilsdorf D, Hansen N. Geometrically necessary, incidental and subgrain boundaries. Scripta metallurgica et materialia. 1991;25(7):1557-1562.
103. Hansen N, Juul Jensen D. Deformed metals–structure, recrystallisation and strength. Materials Science and Technology. 2011;27(8):1229-1240.
104. Humphreys FJ, Hatherly M. Recrystallization and related annealing phenomena. Elsevier; 2012.
105. Li B, Godfrey A, Meng Q, et al. Microstructural evolution of IF-steel during cold rolling. Acta Materialia. 2004;52(4):1069-1081.
106. Bay B, Hansen N, Hughes DA, et al. Overview no. 96 evolution of fcc deformation structures in polyslip. Acta metallurgica et materialia. 1992;40(2):205-219.

107. Kuhlmann-Wilsdorf D. Dislocation cells, redundant dislocations and the LEDS hypothesis. Scripta materialia. 1996;34(4):641-650.
108. Kuhlmann-Wilsdorf D. OVERVIEW No. 131 Regular deformation bands (DBs) and the LEDS hypothesis. Acta materialia. 1999;47(6):1697-1712.
109. Xu W, Ferry M, Cairney J, et al. Three-dimensional investigation of particle-stimulated nucleation in a nickel alloy. Acta Materialia. 2007;55(15):5157-5167.
110. Xu W, Ferry M, Humphreys F. Spatial morphology of interfacial voids and other features generated at coarse silica particles in nickel during cold rolling and annealing. Scripta Materialia. 2009;60(10):862-865.
111. Kuhlmann-Wilsdorf D. The impact of FRN Nabarro on the LEDS theory of workhardening. Progress in Materials Science. 2009;54(6):707-739.
112. Gell M, Worthington P. The plastic deformation and fracture of iron-3% silicon in the temperature range 295° K–473° K. Acta Metallurgica. 1966;14(10):1265-1271.
113. Lindley T, Oates G, Richards C. Fibre-loading Mechanism for the Fracture of Cementite Films in Ferrite. Nature. 1970;226(5241):145.
114. Barnby J. The initiation of ductile failure by fractured carbides in an austenitic stainless steel. Acta Metallurgica. 1967;15(5):903-909.
115. Ashby M. Work hardening of dispersion-hardened crystals. Philosophical Magazine. 1966;14(132):1157-1178.
116. Barlow C, Hansen N. Deformation structures and flow stress in aluminium containing short whiskers. Acta metallurgica et materialia. 1991;39(8):1971-1979.
117. Hughes D, Hansen N. Microstructural evolution in nickel during rolling from intermediate to large strains. Metallurgical Transactions A. 1993;24(9):2022-2037.
118. Huang X-x, Winther G. Dislocation structures. Part I. Grain orientation dependence. Philosophical Magazine. 2007;87(33):5189-5214.
119. Yoo YSJ, Lim H, Emery J, et al. Relating Microstructure to Defect Behavior in AA6061 Using a Combined Computational and Multiscale Electron Microscopy Approach. Available at SSRN 3358892. 2019.
120. León-García O, Petrov R, Kestens LA. Void initiation at TiN precipitates in IF steels during tensile deformation. Materials Science and Engineering: A. 2010;527(16-17):4202-4209.
121. Gurland J, Plateau J. The mechanism of ductile rupture of metals containing inclusions. Brown Univ., Providence; Institut de Recherches de la Siderugie, St.-Germain …; 1963.
122. Tanaka K, Mori T, Nakamura T. Cavity formation at the interface of a spherical inclusion in a plastically deformed matrix. Philosophical Magazine. 1970;21(170):267-279.
123. Parmigiani J, Thouless M. The roles of toughness and cohesive strength on crack deflection at interfaces. Journal of the Mechanics and Physics of Solids. 2006;54(2):266-287.
124. Needleman A. A continuum model for void nucleation by inclusion debonding. Journal of applied mechanics. 1987;54(3):525-531.
125. Xu X-P, Needleman A. Void nucleation by inclusion debonding in a crystal matrix. Modelling and Simulation in Materials Science and Engineering. 1993;1(2):111.
126. Shabrov MN, Needleman A. An analysis of inclusion morphology effects on void nucleation. Modelling and Simulation in Materials Science and Engineering. 2002;10(2):163.
127. Legarth BN. Effects of geometrical anisotropy on failure in a plastically anisotropic metal. Engineering fracture mechanics. 2005;72(18):2792-2807.
128. Charles Y, Estevez R, Bréchet Y, et al. Modelling the competition between interface debonding and particle fracture using a plastic strain dependent cohesive zone. Engineering Fracture Mechanics. 2010;77(4):705-718.
129. Yu Q. Influence of the stress state on void nucleation and subsequent growth around inclusion

in ductile material. International Journal of Fracture. 2015;193(1):43-57.
130. Steglich D, Siegmund T, Brocks W. Micromechanical modeling of damage due to particle cracking in reinforced metals. Computational Materials Science. 1999;16(1-4):404-413.
131. Coffman VR, Sethna JP, Heber G, et al. A comparison of finite element and atomistic modelling of fracture. Modelling and Simulation in Materials Science and Engineering. 2008;16(6):065008.
132. Stroh AN. The formation of cracks as a result of plastic flow. Proc R Soc Lond A. 1954;223(1154):404-414.
133. Beltrán J, Muñoz M. Ab initio study of decohesion properties in oxide/metal systems. Physical Review B. 2008;78(24):245417.
134. Nakamura K, Ohnuma T, Ogata T. First-principles study of structure, vacancy formation, and strength of bcc Fe/V4C3 interface. Journal of materials science. 2011;46(12):4206-4215.
135. Kumar D, Bieler T, Eisenlohr P, et al. On Predicting Nucleation of Microcracks Due to Slip-Twin Interactions at Grain Boundaries in Duplex Near γ-TiAl. Journal of Engineering Materials and Technology. 2008;130(2):021012.
136. Ng BC, Simkin BA, Crimp MA, et al. The role of mechanical twinning on microcrack nucleation and crack propagation in a near-$$ TiAl alloy. Intermetallics. 2004;12(12):1317-1323.
137. Van Stone RH, Low JR, Shannon JL. Investigation of the fracture mechanism of Ti-5AI-2.5 Sn at cryogenic temperatures. Metallurgical Transactions A. 1978;9(4):539-552.
138. Müllner P, Solenthaler C, Uggowitzer P, et al. On the effect of nitrogen on the dislocation structure of austenitic stainless steel. Fundamental Aspects of Dislocation Interactions: Elsevier; 1993. p. 164-169.
139. Müllner P, Solenthaler C, Uggowitzer P, et al. Brittle fracture in austenitic steel. Acta metallurgica et materialia. 1994;42(7):2211-2217.
140. Stroh AN. A theory of the fracture of metals. Advances in Physics. 1957;6(24):418-465.
141. Weertman J. Zener–Stroh crack, Zener–Hollomon parameter, and other topics. Journal of applied physics. 1986;60(6):1877-1887.
142. Butler BG, Paramore JD, Ligda JP, et al. Mechanisms of deformation and ductility in tungsten–A review. International Journal of Refractory Metals and Hard Materials. 2018.
143. Watanabe T, editor Grain boundary design for the control of intergranular fracture. Materials Science Forum; 1989: Trans Tech Publ.
144. Müllner P. On the ductile to brittle transition in austenitic steel. Materials Science and Engineering: A. 1997;234:94-97.
145. Van Stone R, Low J, Shannon J. Investigation of the fracture mechanism of Ti-5AI-2.5 Sn at cryogenic temperatures. Metallurgical Transactions A. 1978;9(4):539-552.
146. Calhoun C, Stoloff N. The effects of particles on fracture processes in magnesium alloys. Metallurgical Transactions. 1970;1(4):997-1006.
147. Lhuissier P, Scheel M, Salvo L, et al. Continuous characterization by X-ray microtomography of damage during high-temperature deformation of magnesium alloy. Scripta Materialia. 2013;69(1):85-88.
148. Nemcko MJ, Wilkinson DS. On the damage and fracture of commercially pure magnesium using x-ray microtomography. Materials Science and Engineering: A. 2016;676:146-155.
149. Garlick R, Probst H. Investigation of room-temperature slip in zone-melted tungsten single crystals. 1964.
150. Argon A, Maloof S. Plastic deformation of tungsten single crystals at low temperatures. Acta metallurgica. 1966;14(11):1449-1462.
151. Rose RM. Yielding and plastic flow in single crystals of tungsten. Trans Met Soc AIME.

1962;224:981-989.
152. Hook RE, Adair AM. On Recrystallization Embrittlement of Chromium. Transactions of the Metallurgical Society of AIME. 1963;227(1):151-&.
153. Cheng Y, Mrovec M, Gumbsch P. Crack nucleation at the∑ 9 (22¯ 1) symmetrical tilt grain boundary in tungsten. Materials Science and Engineering: A. 2008;483:329-332.
154. Eshelby J, Frank F, Nabarro F. XLI. The equilibrium of linear arrays of dislocations. The London, Edinburgh, and Dublin Philosophical Magazine and Journal of Science. 1951;42(327):351-364.
155. Koehler J. The production of large tensile stresses by dislocations. Physical Review. 1952;85(3):480.
156. Friedel J. Dislocations: International Series of Monographs on Solid State Physics. Vol. 3. Elsevier; 2013.
157. Bieler TR, Eisenlohr P, Zhang C, et al. Grain boundaries and interfaces in slip transfer. Current Opinion in Solid State and Materials Science. 2014;18(4):212-226.
158. Stone RV, Cox T, Low J, et al. Microstructural aspects of fracture by dimpled rupture. International Metals Reviews. 1985;30(1):157-180.
159. Kuhlmann-Wilsdorf D. Theory of plastic deformation:-properties of low energy dislocation structures. Materials Science and Engineering: A. 1989;113:1-41.
160. Pollock TC, Wilsdorf HGF. Beryllium fracture observed by in situ high voltage electron microscopy. Materials Science and Engineering. 1983;61(1):7-15.
161. Gardner RN, Wilsdorf HGF. Ductile fracture initiation in pure $$-Fe: Part I. Macroscopic observations of the deformation history and failure of crystals. Metallurgical Transactions A. 1980;11(4):653-658.
162. Gardner RN, Wilsdorf HGF. Ductile fracture initiation in pure $$-Fe: Part II. Microscopic observations of an initiation mechanism. Metallurgical Transactions A. 1980;11(4):659-669.
163. Wilsdorf HGF. The role of glide and twinning in the final separation of ruptured gold crystals. Acta Metallurgica. 1982;30(6):1247-1258.
164. Furukimi O, Kiattisaksri C, Takeda Y, et al. Void nucleation behavior of single-crystal high-purity iron specimens subjected to tensile deformation. Materials Science and Engineering: A. 2017;701:221-225.
165. Noell PJ, Carroll JD, Boyce BL. The mechanisms of ductile rupture. Acta Materialia. 2018;161:83-98.
166. Noell P, Carroll J, Hattar K, et al. Do voids nucleate at grain boundaries during ductile rupture? Acta Materialia. 2017.
167. Noell PJ, Sills RB, Boyce BL. Suppression of ductile rupture in aluminum via dynamic recrystallization. Metallurgical and Materials Transactions A. 2019.
168. Bulatov V, Cai W. Computer simulations of dislocations. Vol. 3. Oxford University Press on Demand; 2006.
169. Rodney D, Ventelon L, Clouet E, et al. Ab initio modeling of dislocation core properties in metals and semiconductors. Acta Materialia. 2017;124:633-659.
170. Zepeda-Ruiz LA, Stukowski A, Oppelstrup T, et al. Probing the limits of metal plasticity with molecular dynamics simulations. Nature. 2017;550(7677):492.
171. Cai W, Nix WD. Imperfections in crystalline solids. Cambridge University Press; 2016.
172. Murty KL, Detemple K, Kanert O, et al. In-situ nuclear magnetic resonance investigation of strain, temperature, and strain-rate variations of deformation-induced vacancy concentration in aluminum. Metallurgical and Materials Transactions A. 1998;29(1):153-159.
173. Ungar T, Schafler E, Hanak P, et al. Vacancy production during plastic deformation in copper determined by in situ X-ray diffraction. Materials Science and Engineering: A.

2007;462(1):398-401.
174. Zehetbauer MJ, editor Effects of non-equilibrium vacancies on strengthening. Key Engineering Materials; 1994.
175. Saada G, editor Interaction of Dislocations and Creation of Point Defects in Workhardening. Acta Crystallographica; 1960.
176. Saada G. Sur la nature des defauts ponctuels crees par le croisement des dislocations. Acta Metallurgica. 1961;9(10):965-966.
177. Saada G. Production de defauts ponctuels par ecrouissage dans un metal cubique a faces centrees. Physica. 1961;27(7):657-660.
178. Zehetbauer MJ, Kohout J, Schafler E, et al. Plastic deformation of nickel under high hydrostatic pressure. Journal of alloys and compounds. 2004;378(1):329-334.
179. Cuitino AM, Ortiz M. Ductile fracture by vacancy condensation in fcc single crystals. Acta materialia. 1996;44(2):427-436.
180. Zhou S, Preston D, Louchet F. Investigation of vacancy formation by a jogged dissociated dislocation with large-scale molecular dynamics and dislocation energetics. Acta materialia. 1999;47(9):2695-2703.
181. Buehler MJ, Hartmaier A, Gao H, et al. The dynamical complexity of work-hardening: a large-scale molecular dynamics simulation. Acta Mechanica Sinica. 2005;21(2):103-111.
182. Siegel R. Positron annihilation spectroscopy. Annual Review of Materials Science. 1980;10(1):393-425.
183. Čížek J, Melikhova O, Barnovská Z, et al., editors. Vacancy clusters in ultra fine grained metals prepared by severe plastic deformation. Journal of Physics: Conference Series; 2013: IOP Publishing.
184. Porter DA, Easterling KE, Sherif M. Phase Transformations in Metals and Alloys, (Revised Reprint). CRC press; 2009.
185. Fang Q, Wang R. Atomistic simulation of the atomic structure and diffusion within the core region of an edge dislocation in aluminum. Physical Review B. 2000;62(14):9317.
186. Pun GP, Mishin Y. A molecular dynamics study of self-diffusion in the cores of screw and edge dislocations in aluminum. Acta Materialia. 2009;57(18):5531-5542.
187. Wiedersich H. On the theory of void formation during irradiation. Radiation Effects. 1972;12(1-2):111-125.
188. Russell K. The theory of void nucleation in metals. Acta Metallurgica. 1978;26(10):1615-1630.
189. Hirth J, Nix W. Analysis of cavity nucleation in solids subjected to external and internal stresses. Acta metallurgica. 1985;33(3):359-368.
190. Epperson JE, Gerstenberg KW, Berner D, et al. Voids formed in quenched and annealed NiAl. Philosophical Magazine A. 1978;38(5):529-541.
191. Hirsch PB, Silcox J, Smallman RE, et al. Dislocation loops in quenched aluminium. Philosophical Magazine. 1958;3(32):897-908.
192. Kiritani M. Formation of voids and dislocation loops in quenched aluminum. Journal of the Physical Society of Japan. 1964;19(5):618-631.
193. Seydel O, Frohberg G, Wever H. Quenching-in of vacancies in pure $$-iron. physica status solidi (a). 1994;144(1):69-79.
194. Shimomura Y, Yoshida S. Heterogeneous nucleation of voids in quenched aluminum. Journal of the Physical Society of Japan. 1967;22(1):319-331.
195. Horsewell A, Singh BN, editors. Influence of grain and subgrain boundaries on void formation and growth in aluminum irradiated with fast neutrons. Radiation-Induced Changes in Microstructure: 13th International Symposium (Part I); 1987.
196. Norris DIR. Voids in irradiated metals (Part I). Radiation Effects. 1972;14(1-2):1-37.

197. Petersen K, Nielsen B, Thrane N. Void formation by annealing of neutron-irradiated plastically deformed molybdenum. Philosophical Magazine. 1976;34(5):693-699.
198. Sundar CS, Bharathi A, Gopinathan KP. Positron annihilation studies of electron-irradiated, cold-worked and hydrogen-charged nickel. Philosophical magazine A Physics of condensed matter Defects and mechanical properties. 1984;50(5):635-651.
199. Zinkle SJ, Singh BN. Microstructure of neutron-irradiated iron before and after tensile deformation. Journal of nuclear materials. 2006;351(1):269-284.
200. Gavini V, Bhattacharya K, Ortiz M. Vacancy clustering and prismatic dislocation loop formation in aluminum. Physical Review B. 2007;76(18):180101.
201. Varvenne C, Mackain O, Clouet E. Vacancy clustering in zirconium: An atomic-scale study. Acta Materialia. 2014;78:65-77.
202. Lounis K, Zenia H, Megchiche EH, et al. Stability of vacancy clusters in nickel: A molecular statics study. Computational Materials Science. 2016;118:279-287.
203. Tehranchi A, Zhang X, Lu G, et al. Hydrogen--vacancy--dislocation interactions in $$-Fe. Modelling and Simulation in Materials Science and Engineering. 2016;25(2):025001.
204. Eyre BL. Transmission electron microscope studies of point defect clusters in fcc and bcc metals. Journal of Physics F: Metal Physics. 1973;3(2):422.
205. Neeraj T, Srinivasan R. Hydrogen Embrittlement of Steels: Vacancy Induced Damage and Nano-Voiding Mechanisms. Corrosion. 2017;73(4):437-447.
206. Krystian M, Setman D, Mingler B, et al. Formation of superabundant vacancies in nano-Pd--H generated by high-pressure torsion. Scripta Materialia. 2010;62(1):49-52.
207. Takai K, Shoda H, Suzuki H, et al. Lattice defects dominating hydrogen-related failure of metals. Acta Materialia. 2008;56(18):5158-5167.
208. Reina C, Marian J, Ortiz M. Nanovoid nucleation by vacancy aggregation and vacancy-cluster coarsening in high-purity metallic single crystals. Physical Review B. 2011;84(10):104117.
209. Marian J, Knap J, Ortiz M. Nanovoid cavitation by dislocation emission in aluminum. Physical review letters. 2004;93(16):165503.
210. Traiviratana S, Bringa EM, Benson DJ, et al. Void growth in metals: atomistic calculations. Acta Materialia. 2008;56(15):3874-3886.
211. Meyers MA, Traiviratana S, Lubarda V, et al. The role of dislocations in the growth of nanosized voids in ductile failure of metals. Jom. 2009;61(2):35.
212. Nguyen L, Warner D. Improbability of void growth in aluminum via dislocation nucleation under typical laboratory conditions. Physical review letters. 2012;108(3):035501.
213. Chang H-J, Segurado J, LLorca J. Three-dimensional dislocation dynamics analysis of size effects on void growth. Scripta Materialia. 2015;95:11-14.
214. Dyson BF, Rodgers MJ. Prestrain, cavitation, and creep ductility. Metal Science. 1974;8(1):261-266.
215. Qi Y, Kosinova A, Kilmametov AR, et al. Generation and healing of porosity in high purity copper by high-pressure torsion. Materials Characterization. 2018;145:1-9.
216. Ribbe J, Baither D, Schmitz G, et al. Network of porosity formed in ultrafine-grained copper produced by equal channel angular pressing. Physical review letters. 2009;102(16):165501.
217. Wegner M, Leuthold J, Peterlechner M, et al. Percolating porosity in ultrafine grained copper processed by high pressure torsion. Journal of Applied Physics. 2013;114(18):183509.
218. Zehetbauer MJ, Steiner G, Schafler E, et al., editors. Deformation induced vacancies with severe plastic deformation: Measurements and modelling. Materials Science Forum; 2006.
219. Kanel G. Spall fracture: methodological aspects, mechanisms and governing factors. International journal of fracture. 2010;163(1-2):173-191.
220. Bronkhorst CA, Gray III GT, Addessio FL, et al. Response and representation of ductile

damage under varying shock loading conditions in tantalum. Journal of Applied Physics. 2016;119(8):085103.
221. Cheng M, Li C, Tang M, et al. Intragranular void formation in shock-spalled tantalum: Mechanisms and governing factors. Acta Materialia. 2018;148:38-48.
222. Curran D, Seaman L, Shockey D. Dynamic failure of solids. Physics reports. 1987;147(5-6):253-388.
223. Meyers MA, Aimone CT. Dynamic fracture (spalling) of metals. Progress in Materials Science. 1983;28(1):1-96.
224. Hahn EN, Fensin SJ, Germann TC. The Role of Grain Boundary Orientation on Void Nucleation in Tantalum. Los Alamos National Lab.(LANL), Los Alamos, NM (United States); 2017.
225. Lieberman EJ, Lebensohn RA, Menasche DB, et al. Microstructural effects on damage evolution in shocked copper polycrystals. Acta Materialia. 2016;116:270-280.
226. Brown A, Krishnan K, Wayne L, et al., editors. 3-D characterization of global and local microstructural effects on spall damage in shock loaded FCC metals: experimental and modeling. ASME 2013 International Mechanical Engineering Congress and Exposition; 2013: American Society of Mechanical Engineers.
227. Fleck RG, Taplin DMR, Beevers CJ. An investigation of the nucleation of creep cavities by 1 MV electron microscopy. Acta Metallurgica. 1975;23(4):415-424.
228. Cane B, Greenwood G. The nucleation and growth of cavities in iron during deformation at elevated temperatures. Metal Science. 1975;9(1):55-60.
229. Riedel H. Fracture at high Temperatures. Springer Verlag; 1987.
230. Greenwood GW. Cavity nucleation in the early stages of creep. Philosophical Magazine. 1969;19(158):423-427.
231. Kassner ME, Hayes TA. Creep cavitation in metals. International Journal of Plasticity. 2003;19(10):1715-1748.
232. Nieh TG, Nix WD. A comparison of the dimple spacing on intergranular creep fracture surfaces with the slip band spacing for copper. Scripta Metallurgica. 1980;14(3):365-368.
233. Wu R, Sandstr\"o m, R. Creep cavity nucleation and growth in 12Cr--Mo--V steel. Materials science and technology. 1995;11(6):579-588.
234. Dyson BF. Continuous cavity nucleation and creep fracture. Scripta Metallurgica. 1983;17(1):31-37.
235. Gandhi C, Raj R. Intergranular fracture in bicrystals—II. Acta Metallurgica. 1982;30(2):505-511.
236. Machlin ES. Creep-rupture by vacancy condensation. JOM. 1956;8(2):106-111.
237. Raj R, Ashby MF. Intergranular fracture at elevated temperature. Acta Metallurgica. 1975;23(6):653-666.
238. Kassner ME. Fundamentals of creep in metals and alloys. Butterworth-Heinemann; 2015.
239. Jiang X-G, Earthman JC, Mohamed FA. Cavitation and cavity-induced fracture during superplastic deformation. Journal of Materials Science. 1994;29(21):5499-5514.
240. Watanabe T, Davies PW. Grain boundary sliding and intergranular fracture behaviour of copper bicrystals. Philosophical Magazine A. 1978;37(5):649-681.
241. Lienert U, Li S, Hefferan C, et al. High-energy diffraction microscopy at the advanced photon source. Jom. 2011;63(7):70-77.
242. Janish MT, Kotula PG, Boyce BL, et al. Observations of fcc and hcp tantalum. Journal of Materials Science. 2015;50(10):3706-3715.
243. HKL Channel 5 OIP, Oxon, United Kingdom.
244. Bachmann F, Hielscher R, Schaeben H, editors. Texture analysis with MTEX--free and open

source software toolbox. Solid State Phenomena; 2010.
245. Keller RR, Geiss RH. Transmission EBSD from 10 nm domains in a scanning electron microscope. Journal of Microscopy. 2012;245(3):245-251.
246. Gifkins RC. Grain-boundary sliding and its accommodation during creep and superplasticity. Metallurgical transactions a. 1976;7(8):1225-1232.
247. Hansen N, Ralph B. The strain and grain size dependence of the flow stress of copper. Acta Metallurgica. 1982;30(2):411-417.
248. Randle V, Hansen N, Jensen DJ. The deformation behaviour of grain boundary regions in polycrystalline aluminium. Philosophical Magazine A. 1996;73(2):265-282.
249. Lim H, Carroll JD, Battaile CC, et al. Quantitative comparison between experimental measurements and CP-FEM predictions of plastic deformation in a tantalum oligocrystal. International Journal of Mechanical Sciences. 2015;92:98-108.
250. Shen Z, Wagoner R, Clark W. Dislocation and grain boundary interactions in metals. Acta metallurgica. 1988;36(12):3231-3242.
251. Lee T, Robertson I, Birnbaum H. TEM in situ deformation study of the interaction of lattice dislocations with grain boundaries in metals. Philosophical Magazine A. 1990;62(1):131-153.
252. Winther G, Huang X, Hansen N. Crystallographic and macroscopic orientation of planar dislocation boundaries—correlation with grain orientation. Acta materialia. 2000;48(9):2187-2198.
253. Sills RB, Aghaei A, Cai W. Advanced time integration algorithms for dislocation dynamics simulations of work hardening. Modelling and Simulation in Materials Science and Engineering. 2016;24(4):045019.
254. Hughes D, Hansen N, Bammann D. Geometrically necessary boundaries, incidental dislocation boundaries and geometrically necessary dislocations. Scripta Materialia. 2003;48(2):147-153.
255. Mecking H, Estrin Y. The effect of vacancy generation on plastic deformation. Scripta Metallurgica. 1980;14(7):815-819.
256. Borchers C, Kirchheim R. Cold-drawn pearlitic steel wires. Progress in Materials Science. 2016;82:405-444.
257. Dlubek G, Brümmer O, Hensel E. Positron annihilation investigation for an estimation of the dislocation density and vacancy concentration of plastically deformed polycrystalline Ni of different purity. physica status solidi (a). 1976;34(2):737-746.
258. Zehetbauer M, Mikulowski B. Deformation induced vacancies and work hardening of metals. Archives of metallurgy. 2001;46(1):65-80.
259. Hirsch PB. Extended jogs in dislocations in face-centred cubic metals. Philosophical Magazine. 1962;7(73):67-93.
260. Kovacs I, Sayed H. Point defects in metals. Journal of Materials Science. 1976;11(3):529-559.
261. Mughrabi H. Dislocation wall and cell structures and long-range internal stresses in deformed metal crystals. Acta metallurgica. 1983;31(9):1367-1379.
262. Abbaschian R, Reed-Hill RE. Physical metallurgy principles. Cengage Learning; 2008.
263. Lubarda V, Schneider M, Kalantar D, et al. Void growth by dislocation emission. Acta Materialia. 2004;52(6):1397-1408.
264. Grady D. The spall strength of condensed matter. Journal of the Mechanics and Physics of Solids. 1988;36(3):353-384.
265. Harkness S, Tesk J, Li C-Y. An analysis of fast neutron effects on void formation and creep in metals. Nuclear Applications and Technology. 1970;9(1):24-30.
266. Suh NP. An overview of the delamination theory of wear. Wear. 1977;44(1):1-16.
267. Thomason P. Ductile fracture of metals. Pergamon Press plc, Ductile Fracture of Metals(UK),

1990. 1990:219.
268. Needleman A, Tvergaard V, Hutchinson J. Void growth in plastic solids. Topics in fracture and fatigue: Springer; 1992. p. 145-178.
269. Besson J. Continuum models of ductile fracture: a review. International Journal of Damage Mechanics. 2010;19(1):3-52.
270. Huang Y. Accurate dilatation rates for spherical voids in triaxial stress fields. Journal of Applied Mechanics. 1991;58(4):1084-1086.
271. Bringa EM, Traiviratana S, Meyers MA. Void initiation in fcc metals: effect of loading orientation and nanocrystalline effects. Acta Materialia. 2010;58(13):4458-4477.
272. Mi C, Buttry DA, Sharma P, et al. Atomistic insights into dislocation-based mechanisms of void growth and coalescence. Journal of the Mechanics and Physics of Solids. 2011;59(9):1858-1871.
273. Essmann U, Mughrabi H. Annihilation of dislocations during tensile and cyclic deformation and limits of dislocation densities. Philosophical Magazine A. 1979;40(6):731-756.
274. Mishin Y, Farkas D, Mehl M, et al. Interatomic potentials for monoatomic metals from experimental data and ab initio calculations. Physical Review B. 1999;59(5):3393.
275. Plimpton S. Fast parallel algorithms for short-range molecular dynamics. Journal of computational physics. 1995;117(1):1-19.
276. Eshelby JD. The determination of the elastic field of an ellipsoidal inclusion, and related problems. Proceedings of the Royal Society of London Series A Mathematical and Physical Sciences. 1957;241(1226):376-396.
277. Anderson PM, Hirth JP, Lothe J. Theory of dislocations. Cambridge University Press; 2017.
278. Bulatov VV, Wolfer WG, Kumar M. Shear impossibility: Comments on "Void growth by dislocation emission" and "Void growth in metals: Atomistic calculations". Scripta Materialia. 2010;63(1):144-147.
279. Merriman C, Field D, Trivedi P. Orientation dependence of dislocation structure evolution during cold rolling of aluminum. Materials Science and Engineering: A. 2008;494(1-2):28-35.
280. Jiang J, Ding Y, Zuo F, et al. Mechanical properties and microstructures of ultrafine-grained pure aluminum by asymmetric rolling. Scripta Materialia. 2009;60(10):905-908.
281. Rao S, Dimiduk D, Parthasarathy T, et al. Atomistic simulations of surface cross-slip nucleation in face-centered cubic nickel and copper. Acta Materialia. 2013;61(7):2500-2508.
282. Benzerga AA. Micromechanics of coalescence in ductile fracture. Journal of the Mechanics and Physics of Solids. 2002;50(6):1331-1362.
283. French I, Weinrich P. The shear mode of ductile fracture in commercial copper. Scripta Metallurgica. 1977;11(11):965-968.
284. El-Naaman SA, Nielsen KL. Observations on mode I ductile tearing in sheet metals. European Journal of Mechanics-A/Solids. 2013;42:54-62.
285. Pardoen T, Hachez F, Marchioni B, et al. Mode I fracture of sheet metal. Journal of the Mechanics and Physics of Solids. 2004;52(2):423-452.
286. Maire E, Zhou S, Adrien J, et al. Damage quantification in aluminium alloys using in situ tensile tests in X-ray tomography. Engineering Fracture Mechanics. 2011;78(15):2679-2690.
287. Landron C, Maire E, Bouaziz O, et al. Validation of void growth models using X-ray microtomography characterization of damage in dual phase steels. Acta Materialia. 2011;59(20):7564-7573.
288. Lecarme L, Maire E, Kc AK, et al. Heterogenous void growth revealed by in situ 3-D X-ray microtomography using automatic cavity tracking. Acta Materialia. 2014;63:130-139.
289. Buljac A, Helfen L, Hild F, et al. Effect of void arrangement on ductile damage mechanisms in nodular graphite cast iron: In situ 3D measurements. Engineering Fracture Mechanics.

2018;192:242-261.
290. Babout L, Maire E, Buffiere J-Y, et al. Characterization by X-ray computed tomography of decohesion, porosity growth and coalescence in model metal matrix composites. Acta Materialia. 2001;49(11):2055-2063.
291. Hosokawa A, Wilkinson DS, Kang J, et al. Effect of triaxiality on void growth and coalescence in model materials investigated by X-ray tomography. Acta Materialia. 2012;60(6-7):2829-2839.
292. Dang N, Liu L, Adrien J, et al. Crack nucleation and growth in α/β titanium alloy with lamellar microstructure under uniaxial tension: 3D X-ray tomography analysis. Materials Science and Engineering: A. 2019;747:154-160.
293. Gürsoy D, De Carlo F, Xiao X, et al. TomoPy: a framework for the analysis of synchrotron tomographic data. Journal of synchrotron radiation. 2014;21(5):1188-1193.
294. Maire E, Carmona V, Courbon J, et al. Fast X-ray tomography and acoustic emission study of damage in metals during continuous tensile tests. Acta Materialia. 2007;55(20):6806-6815.
295. Rice JR. Localization of plastic deformation. Brown Univ., Providence, RI (USA). Div. of Engineering; 1976.
296. Benzerga AA, Thomas N, Herrington JS. Plastic flow anisotropy drives shear fracture. Scientific reports. 2019;9(1):1425.
297. Patterson BM, Escobedo-Diaz JP, Dennis-Koller D, et al. Dimensional quantification of embedded voids or objects in three dimensions using X-ray tomography. Microscopy and Microanalysis. 2012;18(2):390-398.
298. Pardoen T, Delannay F. Assessment of void growth models from porosity measurements in cold-drawn copper bars. Metallurgical and Materials Transactions A. 1998;29(7):1895-1909.
299. Cottrell AH. Dislocations and plastic flow in crystals. 1953.
300. Cottrell AH. Dislocation and Mechanical Properties of Crystals. In: Fisher J, Johnston W, Thomson R, et al., editors.: Wiley, New York; 1957. p. 509.
301. Thompson AW, Weihrauch PF. Ductile fracture: nucleation at inclusions. Scripta Metallurgica. 1976;10(2):205-210.
302. Toda H, Oogo H, Horikawa K, et al. The true origin of ductile fracture in aluminum alloys. Metallurgical and Materials Transactions A. 2014;45(2):765-776.
303. Liu Q, Hansen N. Geometrically necessary boundaries and incidental dislocation boundaries formed during cold deformation. Scripta metallurgica et materialia. 1995;32(8).
304. Arsenlis A, Parks D. Crystallographic aspects of geometrically-necessary and statistically-stored dislocation density. Acta materialia. 1999;47(5):1597-1611.
305. Montheillet F, Le Coze J. Influence of purity on the dynamic recrystallization of metals and alloys. physica status solidi (a). 2002;189(1):51-58.
306. Skrotzki W, Scheerbaum N, Oertel C-G, et al. Recrystallization of high-purity aluminium during equal channel angular pressing. Acta Materialia. 2007;55(7):2211-2218.
307. Ponge D, Bredehöft M, Gottstein G. Dynamic recrystallization in high purity aluminum. Scripta materialia. 1997;37(11).
308. Choi YS, Kim KI, Oh KH, et al. Dynamic recrystallization in high-purity aluminum single crystal under frictionless deformation mode at room temperature. Journal of Materials Research. 2013;28(20):2829-2834.
309. Yamagata H. Dynamic recrystallization and dynamic recovery in pure aluminum at 583K. Acta metallurgica et materialia. 1995;43(2):723-729.
310. International A. Standard Test Method for Analysis of Aluminum and Aluminum Alloys by Inductively Coupled Plasma Atomic Emission Spectrometry (Performance Based Method). Standard Designation E3061 - 17, ASTM International, West Conshohocken, PA. 2017.
311. International A. Standard Test Methods for Determining Average Grain Size, Standard

Designation E 112–13. ASTM International.
312. ASTM WCU. Standard, A. S. T. M. "E8. Standard test method for tension testing of metallic materials." 2004.
313. Brandt R, Neuer G. Electrical resistivity and thermal conductivity of pure aluminum and aluminum alloys up to and above the melting temperature. International Journal of Thermophysics. 2007;28(5):1429-1446.
314. Carroll J, Clark B, Buchheit T, et al. An experimental statistical analysis of stress projection factors in BCC tantalum. Materials Science and Engineering: A. 2013;581:108-118.
315. Brewer LN, Field DP, Merriman CC. Mapping and assessing plastic deformation using EBSD. Electron backscatter diffraction in materials science: Springer; 2009. p. 251-262.
316. Nye J. Some geometrical relations in dislocated crystals. Acta metallurgica. 1953;1(2):153-162.
317. Pantleon W. Resolving the geometrically necessary dislocation content by conventional electron backscattering diffraction. Scripta Materialia. 2008;58(11):994-997.
318. Humphreys F. Characterisation of fine-scale microstructures by electron backscatter diffraction (EBSD). Scripta materialia. 2004;51(8):771-776.
319. Alvi MH, Cheong SW, Weiland H, et al., editors. Recrystallization and texture development in hot rolled 1050 aluminum. Materials Science Forum; 2004: Trans Tech Publ.
320. Cheong SW, Weiland H, editors. Understanding a microstructure using GOS (grain orientation spread) and its application to recrystallization study of hot deformed Al-Cu-Mg alloys. Materials Science Forum; 2007: Trans Tech Publ.
321. Mandal S, Mishra S, Kumar A, et al. Evolution and characterization of dynamically recrystallized microstructure in a titanium-modified austenitic stainless steel using ultrasonic and EBSD techniques. Philosophical Magazine. 2008;88(6):883-897.
322. Mirzadeh H, Cabrera J, Najafizadeh A, et al. EBSD study of a hot deformed austenitic stainless steel. Materials Science and Engineering: A. 2012;538:236-245.
323. Wright SI, Nowell MM, Field DP. A review of strain analysis using electron backscatter diffraction. Microscopy and microanalysis. 2011;17(3):316-329.
324. Wong S, Hodgson PD, Thomson P. Room temperature deformation and recrystallisation behaviour of lead and lead–tin alloys in torsion and plane strain compression. Materials science and technology. 1999;15(6):689-696.
325. Haessner F, Schmidt J. Recovery and recrystallization of different grades of high purity aluminium determined with a low temperature calorimeter. Scripta metallurgica. 1988;22(12):1917-1922.
326. Huang K, Logé R. A review of dynamic recrystallization phenomena in metallic materials. Materials & Design. 2016;111:548-574.
327. Sergueeva A, Zhou J, Meacham B, et al. Gage length and sample size effect on measured properties during tensile testing. Materials Science and Engineering: A. 2009;526(1-2):79-83.
328. Matic P, Kirby III GC, Jolles MI. The relation of tensile specimen size and geometry effects to unique constitutive parameters for ductile materials. Proceedings of the Royal Society of London A Mathematical and Physical Sciences. 1988;417(1853):309-333.
329. Hirth JP, Nix WD. Analysis of cavity nucleation in solids subjected to external and internal stresses. Acta metallurgica. 1985;33(3):359-368.
330. Shimomura Y, Moritaki Y. Formation of Voids in Pure Aluminum Quenched in Hydrogen Gas. Japanese Journal of Applied Physics. 1981;20(10):1787.

# DISTRIBUTION

**Email—Internal**

| Name | Org. | Sandia Email Address |
|---|---|---|
| Brad Boyce | 1881 | blboyce@sandia.gov |
| Doug Medlin | 8341 | dlmedli@sandia.gov |
| Jay Carroll | 1851 | jcarrol@sandia.gov |
| Helena Jin | 8261 | hjin@sandia.gov |
| Sharlotte Kramer | 1528 | slkrame@sandia.gov |
| Julian Sabisch | 8341 | jsabisc@sandia.gov |
| Philip Noell | 1851 | pnoell@sandia.gov |
| Cole Yarrington | 1851 | cdyarri@sandia.gov |
| Ryan Wixom | 1881 | rrwixom@sandia.gov |
| Joseph Michael | 1800 | jrmicha@sandia.gov |
| Wahid Hermina | 1850 | wlhermi@sandia.gov |
| Nydia Brazeau | 8261 | nebraze@sandia.gov |
| Darcie Farrow | 1528 | dfarrow@sandia.gov |
| Alan Jankowski | 8341 | afjanko@sandia.gov |
| LDRD Office | 1971 | Ldrd@sandia.gov |
| Technical Library | 01177 | libref@sandia.gov |

This page left blank


Sandia National Laboratories is a multimission laboratory managed and operated by National Technology & Engineering Solutions of Sandia LLC, a wholly owned subsidiary of Honeywell International Inc. for the U.S. Department of Energy's National Nuclear Security Administration under contract DE-NA0003525.